Thermal Analysis of the Detector in the Radiation Budget Instrument (RBI)

Jonathan Francis Pfab

Thesis submitted to the faculty of the Virginia Polytechnic Institute and State University in partial fulfillment of the requirements for the degree of

Master of Science
In
Mechanical Engineering

Brian Vick, Chair
J. Robert Mahan
Vinh Nguyen

December 19, 2017
Blacksburg, Virginia

Keywords: Radiometry, Parameter Estimation, Thermal Analysis, Radiation Budget Instrument, Gold-black Detector, Remote Sensing

Thermal Analysis of the Detector in the Radiation Budget Instrument (RBI)

Jonathan Pfab

ABSTRACT

Earth radiation budget instruments are devices designed to study global climate change. These instruments use telescopes embarked on low-earth-orbit satellites to measure Earth emitted and reflected solar radiation. Radiation is sensed as temperature changes caused by radiation absorbed during scans of the earth on a delicate gold-black coated detector. This work is part of a larger effort to develop an end-to-end dynamic electro-thermal model, based on first-principles, for the next generation of earth radiation budget instruments, the Radiation Budget Instrument (RBI). A primary objective of this effort is to develop a numerical model of the detector to be used on RBI. Specifically, the sensor model converts radiation arriving at the detector, collimated and focused through telescopes, into sensible heat; thereby producing a voltage. A mathematical model characterizing this sensor is developed. Using a MATLAB algorithm, an implicit finite-volume scheme is implemented to determine the model solution. Model parameters are tuned to replicate experimental data using a robust parameter estimation scheme. With these model parameters defined, the electro-thermal sensor model can be used, in conjunction with the remaining components of the end-to-end model, to provide insight for future interpretation of data produced by the RBI.

Thermal Analysis of the Detector in the Radiation Budget Instrument (RBI)

Jonathan Pfab

GENERAL AUDIENCE ABSTRACT

Earth radiation budget instruments are devices designed to study global climate change. These instruments use telescopes embarked on low-earth-orbit satellites to measure radiation exiting the atmosphere of the Earth. As the atmospheric science community works to design and develop the next generation of these instruments, a need for a model capable of simulating operating performance has arisen. This work is part of a larger effort to develop a complete model for the next generation of Earth radiation budget instruments, the Radiation Budget Instrument (RBI). A primary objective of this effort is to develop a model of a detector to be used on the RBI. The modelling techniques used to characterize the detector are presented in this work. Once the model has been developed, optimal model parameters are determined to tune the model. With these model parameters defined, the detector model can be used, in conjunction with the remaining pieces of the overall end-to-end model, to provide insight for future interpretation of data produced by the RBI.

Acknowledgments

I would like to thank my advisor, Dr. Brian Vick, for giving me the opportunity to complete my Master's Degree in Mechanical Engineering at Virginia Tech. Under Dr. Vick's guidance, I have grown as both a researcher and as an individual. Dr. Vick dedicated countless hours to helping me succeed, making this work possible.

I would also like to thank Dr. J. Robert Mahan and Dr. Vinh Nguyen for their willingness to serve on my committee. Thank you for welcoming me into the Thermal Radiation Group. Without this team, I surely could not have completed this work.

I owe a debt of gratitude to Dr. Kory J. Priestley and Anum Barki Ashraf of the NASA Langley Research Center. They provided the opportunity and encouragement and without which this work would have come to fruition.

I am especially grateful to my family for supporting me through all of my time at Virginia Tech. I would like to thank my parents, Michael and Rachel, for everything. They taught me to keep an open mind and work hard; the rest will fall into place. I wouldn't have gotten to this point if they hadn't pushed me from the start. I love you.

Lastly, I would like to thank all of my friends at Virginia Tech. They made my stay at Virginia Tech a pleasant one and I would not have stayed so long without them. A special thanks to Noah Allen for his coding expertise, a real MATLAB wizard.

Table of Contents

List of Figures

List of Tables

Nomenclature

Symbols:

A Area (m^2)

A_{cont} Surface area along the boundary of sensor (m^2)

A_s Surface area (m^2)

c Specific heat (J/kgK)

h_{cont} Contact heat transfer coefficient (W/m^2K)

h_{rad} Radiation heat transfer coefficient (W/m^2K)

H Unit step function $(-)$

i Control volume index in x-direction $(-)$

ii Total number of control volumes in x-direction $(-)$

I Irradiation source distribution across the detector (W/m^2)

I_c Magnitude of irradiation source (W/m^2)

j Control volume index in y-direction $(-)$

jj Total number of control volumes in y-direction $(-)$

k_{ther} Thermal conductivity (W/mK)

L Length (m)

L_x Length of detector (m)

L_y Width of detector (m)

L_z Thickness of detector (m)

N Total number of thermocouples $(-)$

N_{Bound} Number of boundary control volumes $(-)$

N_{Loc} Number of measurement locations $(-)$

M Number of measurements $(-)$

p Parameter index $(-)$

q Heat transfer rate (W)

q'' Heat flux (W/m^2)

RMS Root-mean-square voltage (V)

S	Objective function (V^2)
t	Time (s)
t_{start}	Experimental heat source start time (s)
T	Temperature distribution of the detector (K)
T_{sur}	Temperature of surrounding enclosure (K)
V	Output voltage (V)
$\mathcal{V}$	Volume (m^3)
x	Primary direction (m)
$x_{1,2}$	Starting and ending positions of the heat source in the x-direction (m)
X_p	Sensitivity coefficient to parameter p (V)
y	Secondary direction (m)
$y_{1,2}$	Starting and ending positions of the heat source in the y-direction (m)

Greek:

α	Thermal diffusivity (m^2/s)
α_s	Seebeck coefficient for a single thermocouple (V/K)
$\bar{\beta}$	Matrix of parameters to be estimated
Δt	Time step (s)
ΔT	Temperature rise (K)
ΔV	Voltage change (V)
Δx	Control volume length in x-direction (m)
Δy	Control volume length in y-direction (m)
ϵ	Emissivity coefficient $(-)$
ϵ_{Tol}	Tolerance $(-)$
$\bar{\eta}$	Outward normal $(-)$
θ	Dimensionless temperature distribution $(-)$
ρ	Density (kg/m^3)
σ	Stefan-Boltzmann constant (W/m^2K^4)
τ	Time constant (s)

Φ Process $(-)$

Subscripts:

ave	Average
$cont$	Contact
DC	DC offset
eq	Equivalent
GA	Gold absorber
GB	Gold-black
GS	Gold shunt
i	Control volume i
j	Control volume j
n	Mesh refinement level
nom	Nominal
on	Heat source starting time
off	Heat source ending time
rad	Radiation
Rel	Relative
$ther$	Thermal

Superscripts:

p	Time index
$+$	Denotes dimensionless

1 <u>Introduction</u>

1.1 Motivation

Throughout the long history of the human race, the Earth has always been home. Barring drastic advancements in space travel, the Earth will be the home for generations to come for the foreseeable future. The way we treat our home now shapes the livelihood of our posterity.

Acceleration of industrialization over the last century has led to increased concern of the health of the Earth's climate. Over the years, lawmakers have posed questions about the impact of "global warming, polar ice and sea level changes, deforestation…and changes in cloud radiative effects resulting from greenhouse warming…" [1] However, atmospheric scientists cannot provide lawmakers with answers due to "a lack of knowledge of the interdependent processes that affect regional and global climate." [1] Before we can begin to understand how our actions affect the climate, we must first understand the climate itself.

In order to better understand the climate, the atmospheric science community has launched a series of programs to monitor the Earth radiation budget. The Earth radiation budget is defined as "the difference between the absorbed solar radiation and the radiation emitted from the Earth and its atmosphere which is lost to space." [2] A primary mission of Earth science is to monitor the planetary thermal radiation budget with sufficient accuracy and over a sufficiently long time-interval to identify and track global climate change, with emphasis on clarifying the role of clouds [3]. For the past twenty years *Clouds and the Earth's Radiant Energy System* (CERES) employed a suite of three broadband scanners embarked on a series of near-Earth-orbit satellites to capture this information [1]. This instrument produces global maps revealing the distribution of heat energy radiated from the Earth in three wavelength intervals and at monthly intervals [4].

To assure continuity of observation, a CERES follow-on, the *Radiation Budget Instrument* (RBI), is currently nearing completion of its first instrument [5]. The RBI footprint on the Earth is similar in size and shape to the CERES footprint, and its mission is essentially the same as that of CERES; however, the user community is pressing for a half-order-of-magnitude improvement in accuracy with RBI. This requirement has motivated the engineering community

to not only employ more advanced technology, but also to conceive modeling tools capable of simulating instrument performance to that level of accuracy [3].

1.2 Objectives

The objective of this thesis is to formulate an accurate model of the sensor in the Radiation Budget Instrument used to track global climate change. The goals of this effort are to:

1. Formulate a first-principle mathematical model of the sensor in the Radiation Budget Instrument.
2. Develop a finite volume solution of the mathematical model.
3. Implement the finite volume solution in a MATLAB algorithm.
4. Validate the model against experimental data.
5. Present the atmospheric science community with a tool capable of providing insight for future interpretation of data produced by the Radiation Budget Instrument.

1.3 Literature Review

The literature review for this thesis is divided into two major sections – the Thermal Radiation Group (TRG) at Virginia Tech and parameter estimation. The former has been chosen because the work performed by the TRG serves as the groundwork upon which this thesis is built, and the latter has been chosen for its important role in validating the model against experimental data.

1.3.1 Thermal Radiation Group

Under the direction of J. Robert Mahan, the Thermal Radiation Group at Virginia Tech has collaborated for many years with the Langley Research Center, a field center of the National Aeronautics and Space Administration (NASA), to study the Earth radiation budget. The work of the TRG began in 1975 with an analysis by Fanney [6] of the detectors proposed for use in the Long-Term, Zonal Earth Energy Budget Experiment (LZEEBE) instrument. Since then, dozens of graduate students have worked on high-resolution thermal and optical models of various iterations of radiation budget instruments. In 2002, Ira Sorensen's PhD dissertation included a detailed history of the work done by the TRG from its inception until the turn of the century [7]. For brevity, this thesis will focus only on the new work that has been done since Sorensen's dissertation was

written. For those readers interested in the work done before the turn of the century, the author directs them to read Sorensen's dissertation.

The updated history of the TRG begins with the work done in Sorensen's dissertation. Sorensen developed a tool to aid in development of radiometric instruments based on the Monte Carlo ray-trace (MCRT) method. Additionally, Sorensen developed a generic finite difference model of a thermistor bolometer detector used for radiometric instruments. By combining these two ideas, Sorensen created a complete and robust optical and dynamic electro-thermal model of the CERES instrument. Using a search method based on genetic algorithms, he then developed a design tool capable of determining optimal system parameters given varying instrument configurations [7].

The MCRT method is the standard for modelling radiation heat transfer in radiation budget instruments; therefore a continued effort to further our knowledge and understanding of this technique has been performed. In 2002, Sánchez characterized results from the MCRT method based on standard statistical analysis. Using standard statistical principles, she developed a model to predict the uncertainty of distribution factors and heat fluxes at various confidence intervals. Sánchez also presents a model for predicting confidence intervals associated with distribution factors and heat fluxes based on this uncertainty. By applying this work to CERES, the TRG gained a better understanding of the accuracy of the results produced from a model utilizing the MCRT method [8].

After Sánchez, Mahan left Virginia Tech to accept an administrative position at Georgia Tech. The TRG resumed operation with his return in 2014. At this time, development of the successor to CERES was underway. During this development, the idea of using gold-black as an absorber medium for the detector had become the front runner for the design. However, a lack of understanding of the optical and thermal characteristics of gold-black presented an interesting dilemma for the scientific community. In 2015, Quinlan sought to further the communities' understanding of the topic by developing a model for the absorption of thermal radiation by gold-black. Quinlan showed that gold-black can be simulated using random fractal geometry and a set of descriptive parameters. Incorporating this random fractal geometry simulation with circuit theory, Quinlan developed a model for calculating absorptivity. Lastly, Quinlan theorized that

using a formal parameter estimation technique the model could be refined to match gold-black data found in literature [9].

To this point, the radiation budget instruments have been designed to minimize the effect of diffraction and polarization on measurements. In 2016, Mahan hypothesized that performance of these instruments could be enhanced by including quantitative measures of these effects during operation. A MCRT model that includes these effects was developed and investigated. Ultimately, it was found that the incorporation of these effects had negligible impact on the performance of the instrument for the CERES configuration [10]. In 2017, Mahan pursued this effort by applying the analysis to a theoretical instrument model more sensitive to these effects. Mahan presents a series of instrument design configurations and demonstrates how diffraction and polarization can affect the results. If the instrument is not designed to minimize these effects, the resulting measurements can be compromised [11].

As a continuation of the effort to broaden the understanding of physical optics phenomena in the MCRT realm, Stancil investigated the effect of coherence on the performance of instruments. To do this, Stancil developed a simulation of a Michelson interferometer using the MCRT method. A Michelson interferometer is known to be an effective tool for "quantifying the degree of temporal coherence of a quasi-monochromatic light beam [12]." By comparing experimental data from a real and a simulated interferometer, Stancil demonstrated that the MCRT method is capable of simulating an actual Michelson interferometer. This model could therefore be used for further understanding of the effect of coherence on the performance of instruments [12].

The TRG simultaneously pursued an effort based on modelling and investigating the performance of the RBI instrument [13]. One such effort was an investigation of the performance and effectiveness of the filters used to block long-wavelength radiation in the instrument short-wavelength. Mahan and Vick validated the hypothesis that in order to meet stringent design requirements two sequential and coaxial filters, rather than one, would be required in the instrument. This effort supported a necessary design change to the instrument [14]. Pfab developed an electro-thermal model of a typical detector in a radiation budget instrument. Subject to knowledge of the relevant parameters, this tool can be used to model a specific instrument [3].

1.3.2   Parameter Estimation

With any modelling technique, the usefulness of the model is limited to the accuracy with which it can replicate data produced by the real system. In general, a model has a set of parameters that are selected to replicate real data under identical conditions. Often, these parameters such as thermos-physical properties can be well-defined. If the model is accurate, the results it produces will replicate those of the actual system. However, it is not uncommon for one or more of the parameters to be ill-defined or unknown. In these instances, the science of parameter estimation is the standard for determining values of unknown parameters. The basic idea is to use the actual behavior of the system to determine the model parameters required in order for the model to reproduce that behavior. Beck [15] and Özisik [16] present techniques that can be used to determine these system parameters. While the examples presented in the cited works focus on thermal systems, the techniques presented are generic and can be applied to any field. One common technique uses the least-squares algorithm to determine optimal parameter estimates.

This parameter estimation technique has been the motivation behind many investigations. Some relevant examples are presented here.

McMasters showed that the parameters capable of being determined are dependent on the data being used. Using data from one experiment, McMasters showed that one could not distinguish between two interdependent parameters and could only estimate values for the combination of the two. However, with the introduction of a second experiment, the two data sets can be used simultaneously to determine the two interdependent parameter values separately [17].

Vick used parameter estimation to determine optimal parameters for a model describing blood perfusion. Blood perfusion is the local blood flow through a capillary network. Vick presented a mathematical model for blood perfusion based on unknown coefficients. Using a non-invasive heat flux and temperature sensor, Vick's team obtained experimental measurements of local blood perfusion. Armed with these measurements and a least-squares algorithm, they were able to determine the model coefficients. Once those were obtained, Vick demonstrated excellent agreement between the model and actual data found in literature [18].

Vick and Schneck used the parameter estimation technique to quantify the real contact area between two surfaces. The real surface area in contact between two surfaces is often hard to

quantify due to factors such as surface topography. This area becomes important when trying to quantify the heat generated by friction when one surface is sliding across the other. They present a model based on unknown parameters. The parameters for this model were determined and a tool for predicting heat loss by friction was developed using parameter estimation [19].

The most relevant parameter estimation effort is that carried out by Sorensen, discussed previously. Rather than a least-squares algorithm, Sorensen used genetic algorithms to determine optimal parameters for the CERES detector model. In contrast to Sorensen's effort, the work presented in this thesis uses a least-squares algorithm to determine optimal parameters for the RBI detector model.

In all of the efforts that the author found, the parameters to be estimated were either system properties (thicknesses, thermo-physical properties, etc.) or experimental properties (magnitude of heat source, heat source duration, etc.). The literature is reticent on works where a mixture of both system and experimental properties must be determined. When performing parameter estimation in Chapter 6, the parameter estimation effort reported here involves this dilemma. Three of the four parameters are system parameters and are used to replicate the real instrument. The fourth, however, is an experimental parameter that arises from a lack of information about the test conditions. This parameter is specific to the test conditions at hand and has to be determined simultaneously with the system parameters. However, the experimental parameter is never used outside of this investigation and is not useful for future work. Conversely, the system parameters are integral to replicating future data. This is apparently a unique feature of the effort reported here.

1.4 Organization

This thesis is divided into seven chapters. The first chapter presents an overview of the motivations and the goals of this effort. The second chapter presents information regarding the Radiation Budget Instrument. This information provides the necessary background needed to develop a useful model. The third chapter develops the mathematical model used to characterize the sensor in the Radiation Budget Instrument. Chapter 4 presents the finite volume solution developed to solve the mathematical model. After developing the model and the solution method, Chapter 5 presents a series of case studies aimed at establishing the relationship between input parameters and the output solution. In Chapter 6, the model parameters are tuned, using a rigorous

parameter estimation scheme, to permit replication of the experimental results using the developed model. Finally, Chapter 7 concludes this effort and presents recommendations for future efforts.

2   Physical System

2.1   RBI Package

The Joint Polar Satellite System (JPSS) is a series of polar orbiting satellites conceived to gather global measurements of atmospheric, terrestrial and oceanic conditions. To meet these goals, the JPSS satellites are equipped with four state-of-the-art instruments. These instruments are:

- Advanced Technology Microwave Sounder (ATMS) – Collects atmospheric temperature and moisture information
- Cross-track Infrared Sounder (CrIS) – Collects atmospheric temperature and moisture information
- Ozone Mapping and Profiler Suite (OMPS) – Documents the health and concentration of the Earth's ozone layer
- Visible Infrared Imaging Radiometer Suite (VIIRS) – Provides high resolution images of the Earth's surface

A fifth instrument for measuring earth's reflected sunlight and emitted thermal radiation is included on these satellites. JPSS-1 is equipped with the Clouds and the Earth's Radiant Energy System, or CERES, instrument [1]. Beginning with JPSS-2, shown in Figure 2.1, CERES will be replaced with the next-generation instrument, the Radiation Budget Instrument, or RBI [20]. This instrument is currently under development, and is scheduled for launch on JPSS-2 in November 2021, thereby providing continued monitoring of the earth's radiation budget into the foreseeable future [21].
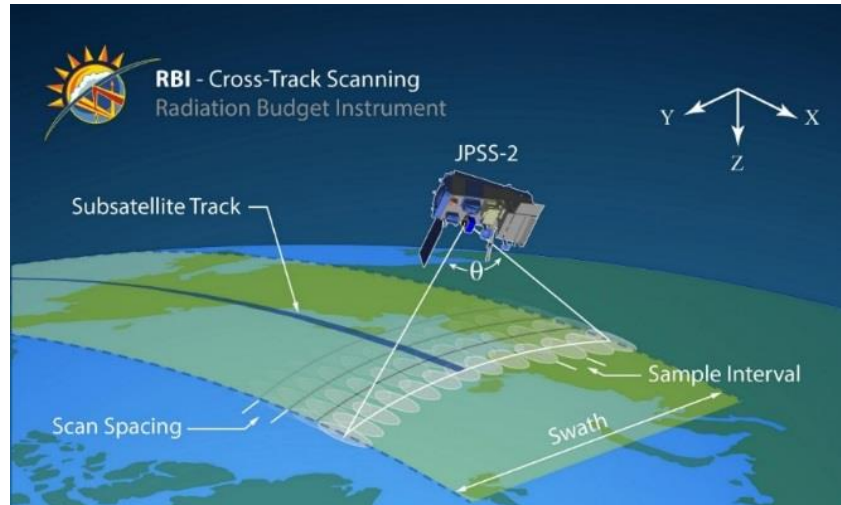
Figure 2.1. Rendering of RBI mounted on JPSS-2 performing a typical earth scan [21].

An exploded view of the RBI instrument, shown in Figure 2.2, consists of an electronics package, an optical module, three calibration targets, and a scanning module [22]. At a high level, the scanning module orients the optical module to observe an earth scene. The information is obtained by the optical module and sent to the electronics package for interpretation. Periodically, the optical module is oriented to observe the on-board calibration targets for radiometric correction.
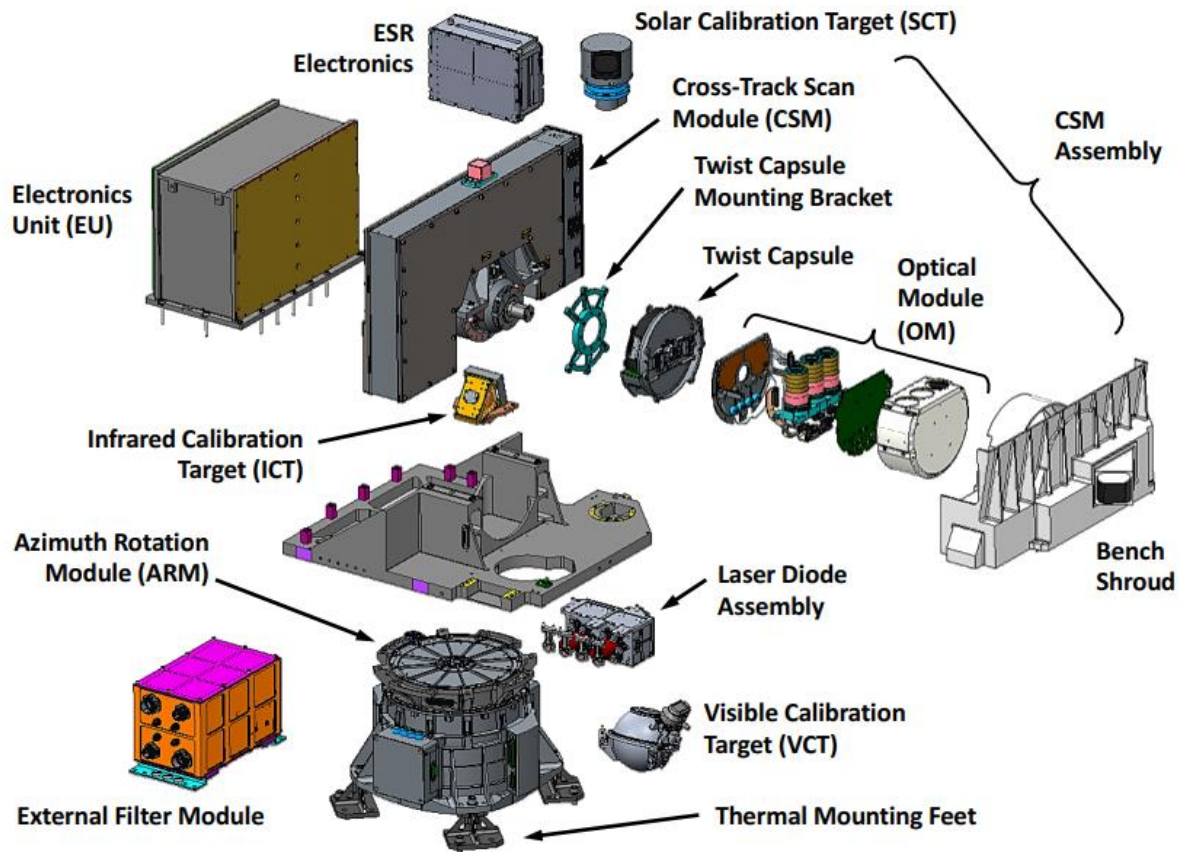
Figure 2.2. Exploded CAD render of entire RBI instrument and assembly view of individual components [22].

The optical module, shown in Figure 2.3 houses three almost identical telescopes, each sensitive to a different spectral band. Each of these three telescopes, referred to as channels, measures one of the following: reflected solar energy (shortwave radiation), earth emitted radiation (longwave radiation), and the total radiation leaving the earth (shortwave and longwave radiation) [23]. The longwave and shortwave channels permit differentiation between two types of radiation leaving the earth. The sum of the shortwave and longwave channels should provide the same information as the total channel. Therefore, this latter is used to verify that the other two independent channels are not registering radiation outside their respective spectral bands [24].
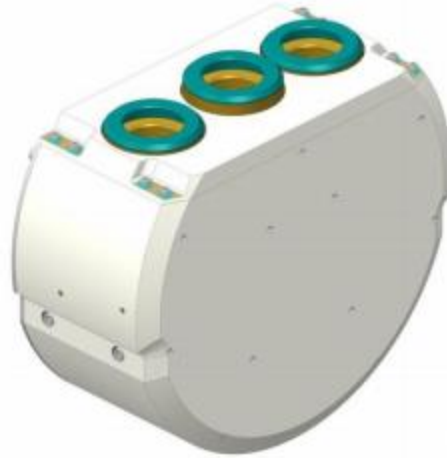
Figure 2.3. CAD rendering of the optical module and the three individual measurement channels [23].

Thermal radiation enters through the aperture of the three single channels. A cut-away view of the shortwave channel appears in Figure 2.4. As the light propagates farther into the telescope, a series of baffles collimates the radiation such that rays not parallel or nearly parallel to the optical axis have a reduced chance of reaching the focal plane. The rays that survive the baffle system are reflected by two co-axial mirrors, pass through a filter (with the exception of the total channel) and ultimately arrive at the focal plane. The filter is selected to block the unwanted spectral content for a given channel. For example, in the longwave channel the filter is selected so that it blocks any shortwave radiation from arriving at the focal plane [23].
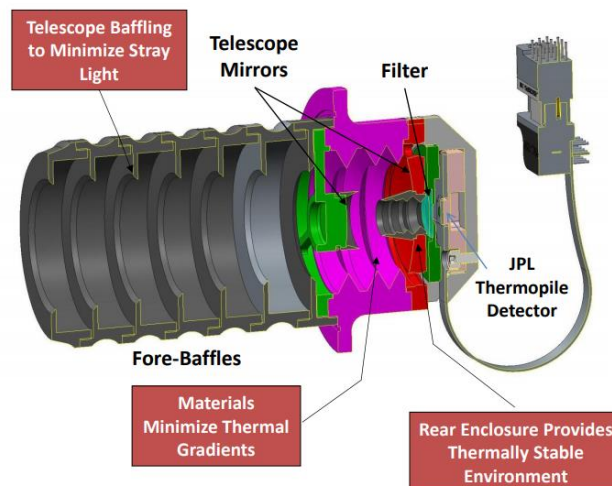
Figure 2.4. CAD rendering of shortwave channel design [23].

In addition to partially collimating the radiation that arrives at the entrance aperture, the telescope has been designed to ensure that the signal output from the detector is due solely to the

11

radiation arriving from the Earth scene. To accomplish this goal, the telescope surfaces, including the focal plane itself, must be maintained at a constant known temperature. Radiation that does not penetrate to the focal plane must either be absorbed by the telescope structure itself or be reflected back out the telescope aperture. If absorbed by the telescope, the temperature of the telescope itself will rise. This disruption of equilibrium would in turn lead to a radiation exchange between the detector and the telescope. The materials of the telescope itself have been selected to minimize any thermal gradients near the focal plane. Additionally, the end cap of the telescope has been designed to include heaters that help assure a thermally stable environment [23].

2.2   Detector Model Information

Ultimately, the goal of the instrument is to convert thermal radiation into digital counts. The radiation that survives the complex telescope system is absorbed by a detector utilizing a thermopile array to create an output voltage. Figure 2.5 shows the complete focal-plane assembly located within each telescope channel [25]. The heart of the entire instrument is the thermopile detector itself. A labeled photograph of the RBI detector appears in Figure 2.6. The detector consists of two hexagonal sensors mounted on a circuit board. In order to obtain nearly perfect absorptivity, the sensors and surrounding circuit board are coated with a thin layer of gold-black [25].

Figure 2.5. Complete focal plane module assembly [25] © 2016 IEEE.
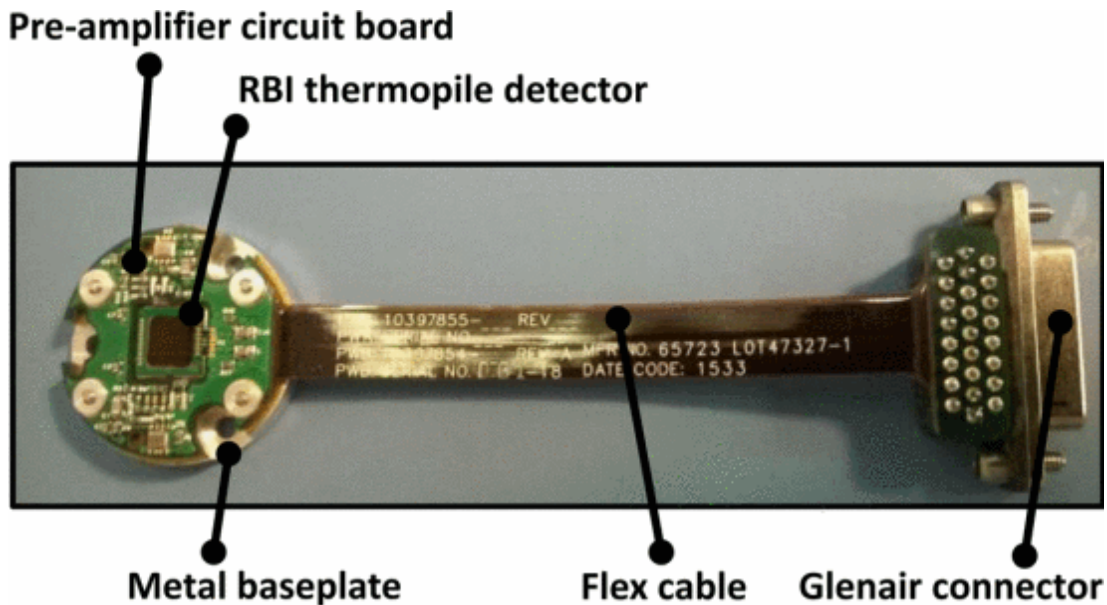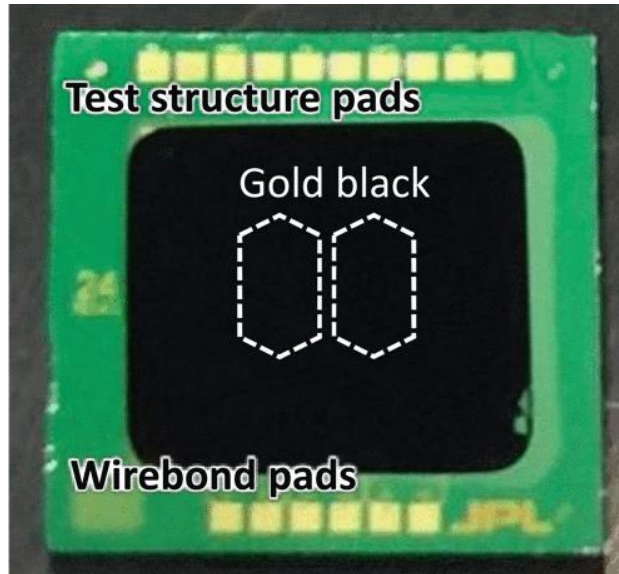
Figure 2.6. RBI detector consisting of two sensors mounted on a circuit board and coated with in gold-black [25] © 2016 IEEE.

Redundancy is achieved by using two sensors in each channel. Once the satellite has been inserted in orbit, it will be impossible to service the instrument. During normal instrument operation, the voltage signal will only be recovered from one of the two sensors. If the primary sensor fails, the output would then be provided by the remaining sensor.

Each hexagonal sensor is surrounded by a series of bismuth-antimony-tellurium thermopiles [25]. This thermopile "fence" acts as the thermal connection between the hexagonal detectors and the substrate, as illustrated in Figure 2.7. The area beneath a hexagonal detector has been etched away to reduce its thermal mass. The following analogy to a typical trampoline is often invoked: The fabric (detector) is supported by a series of springs (thermopile fence) that connects it to the metal base (substrate). The thermopile fence provides the mechanism for converting the absorbed thermal radiation into a voltage single through the thermoelectric effect [25].

13
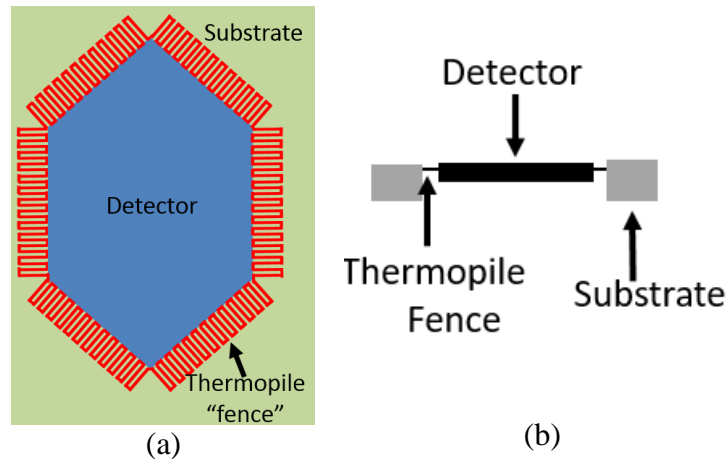
Figure 2.7. Schematic diagram showing the sensor mounted in the substrate thermally connected by the thermopile fence, (a) plan view and (b) cross-sectional view.

The composition of the detector itself has been designed to meet a response time requirement of about 9 ms [25]. A brief description of the construction process is presented here. Refer to Figure 2.8 for a cross-sectional view of the finished detector.

- A gold impregnated silicon-nitride layer (shown in yellow) is bonded to the silicon-nitride printed circuit board (PCB) (shown in purple).
- The thermopile fence (shown in red) is placed on the PCB.
- Electrical insulation (shown in blue) is laid down on top of the thermopile fence contacts to electrically isolate it from the gold-black layer.
- A thin gold shunt (shown in gold) is laid down to assure strong thermal contact between the gold-black and the thermopile fence.
- A layer of gold-black (shown in black) is deposited onto the gold shunt.
- PCB is etched away below the detector between the thermopile fence contacts.
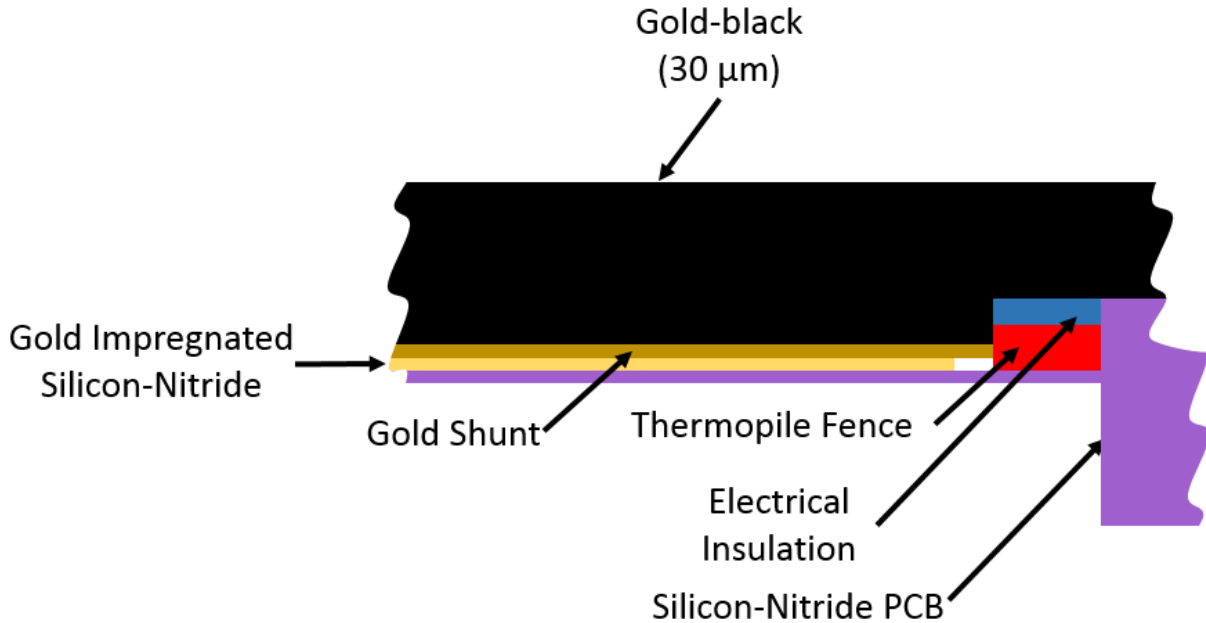
Figure 2.8. Cross-sectional view of the detector showing its composition.

The gold shunt was not included in the original detector design. However, the response time of the device was found to be too slow. Radiation absorbed by the gold-black took too long to conduct to the thermopile fence due to the low conductivity of gold-black. To accelerate the response time, a thin layer of gold, referred to as the gold shunt, was introduced to the design. Having a very high thermal conductivity, this gold layer increases the overall effective thermal conductivity of the detector. In this configuration, the radiation is absorbed by the gold-black layer and conducts down to the gold shunt. The energy is quickly and evenly dispersed in the lateral direction (towards the thermopile fence) due to the high thermal conductivity of gold. The heating of the thermopile fence produces a voltage response.

2.3 Thermal Processes

Five main thermal processes affect the output voltage from a single detector. These five processes are: incident irradiation, contact conductance, radiation exchange with the surroundings, conduction within the device, and thermal storage within the device. A brief description of each of these processes follows.

1. Incident radiation. As mentioned in Section 2.2, radiation is partially collimated through a baffle system and then focused onto the focal plane by a two-mirror reflecting telescope. Of the radiation that floods the focal plane, the portions that illuminate the

15

detector are almost perfectly absorbed. The absorbed radiation causes the temperature of the detector to rise from its equilibrium values creating an output voltage as already described. Measuring the magnitude of the incident irradiation is the only function of the detector.

2. Contact conductance. This contact conductance is the effect the thermopile fence introduces by being attached to the detector. The thermopile fence serves as a thermal bridge the between detector and the surrounding substrate. As the temperature of the detector begins to rise, heat is drawn out of the detector through the thermopile fence and into the substrate. As noted in Section 2.1, the telescope has heaters intended to keep the substrate at a constant temperature. In addition to acting as a cooling mechanism, the flow of energy across the thermopile fence also directly converts the thermal energy into a voltage output through the thermoelectric, or Seebeck, effect.

3. Radiation exchange with the optically visible surroundings within the telescope. The detector can see the various telescope components, such as the filters and the telescope walls. Additionally, the detector can see the underlying substrate because much of the PCB directly below the detector has been etched away. As a result, as the temperature of the detector rises, the net radiation exchange above and below the detector acts to cool the detector. As noted in Section 2.1, the telescope has heaters to maintain the key components of the telescope at a constant temperature. The radiation exchange effect is small compared to the effect of the thermopile fence, because temperature rises in the detector are on the order of 100 mK.

4. Conduction. Conduction is an important mechanism for transporting energy throughout the detector. If irradiation is absorbed in the center of the detector, it must either conduct to the edges to be removed by the thermopile fence, or be transferred to the surroundings through radiation exchange. Therefore, if conduction was absent within the device, energy absorbed by the detector in regions not immediately adjacent to the thermopile fence would not contribute to creation of a voltage.

5. Thermal storage. Because the detector has a thermal mass, its ability to store thermal energy ultimately affects the response time of the output signal.

3 **Thermal Model**

3.1 **Model Assumptions**

The Thermal Radiation Group (TRG) was tasked with modelling the gold-black sensor. In order to model this sensor, some logical assumptions had to be embraced to simplify the model. These simplifications are presented here.

In order to model the detector, a simplified construction of the detector was developed as shown in Figure 3.1. In this configuration, it is assumed that the detector is comprised only of 3 distinct layers – gold-black, the gold shunt and the gold-impregnated silicon-nitride. Since the detector itself is very thin (~30 μm) compared to its length and width (~2 by 1 mm), it is assumed that thermal gradients through the thickness of the detector (z-direction) are negligible compared to lateral gradients across the detector (x- and y-direction). In agreement with the assumption that the detector is lumped in the z-direction, the effective thermal properties are a combination of the three individual layers.
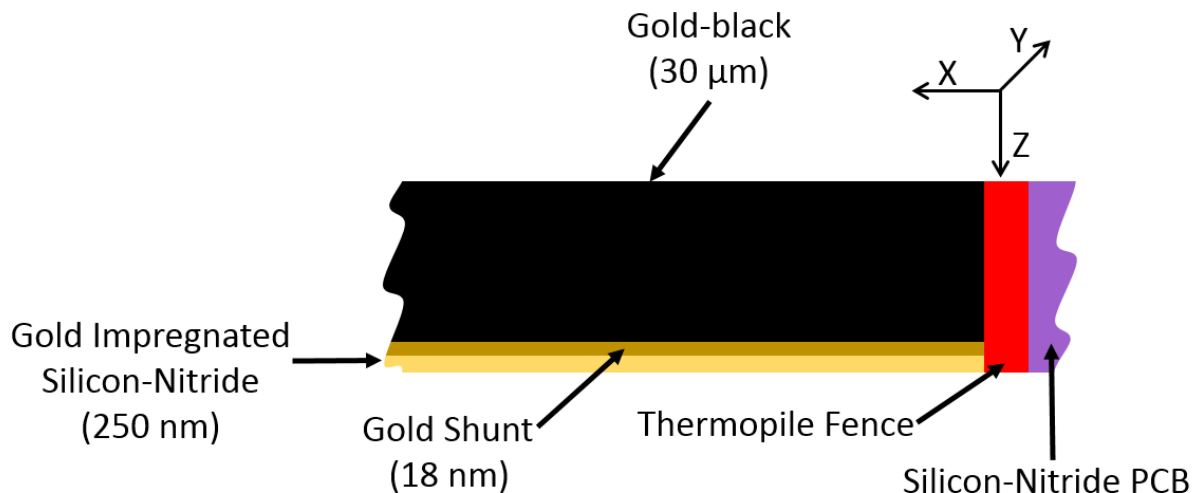
Figure 3.1. Cross-sectional view of the simplified detector model showing the composition used for modeling.

In addition to lumping the model in the z-direction, an assumption that the thermopile fence spans the whole thickness of the detector was made. The magnitude of the effect the thermopile fence has on the detector is related to the contact boundary area. In reality, the thermopile fence only contacts a small section of the detector, as seen in the configuration depicted in Figure 2.8. It

17

would be impossible to determine the precise thicknesses of each of the thermopile junctions that make up the entire fence and thereby accurately compute a total contact area. To overcome this, it was decided to assume the fence spanned the whole thickness of the detector and to determine an equivalent boundary effect based on this area. This can be represented mathematically as

$$(h_{cont}A_{cont})_{Physical} = (h_{cont}A_{cont})_{Equivalent}. \qquad \textbf{(3.1)}$$

This is a similar issue to that of traditional heat exchangers where the overall heat transfer coefficient is quoted based on a representative rather than an actual area [26].

The final assumption made is that the heaters in the telescope perfectly maintain the equilibrium temperature of the telescope surfaces. The heaters are designed to energize when the temperature of the telescope falls below a certain temperature. The heaters remain energized until the telescope reaches a temperature above equilibrium temperature. However, because the temperature drift from equilibrium is small, the assumption that the telescope surfaces are maintained at a constant temperature is justified. Future iterations of this model could incorporate a drifting surrounding temperature.

3.2 Mathematical Model

A mathematical model for the detector was developed using the simplified detector configuration. The model incorporates:

- Two-dimensional heat conduction over the hexagonal detector surface. An accurate model does not need to be three-dimensional because lumping the temperature in the thin z-dimension has been deemed appropriate.
- A volumetric heat source to model the absorbed radiation in the detector that arrives at the focal plane from an earth scene, consistent with lumped heat capacity through its thickness.
- Boundary conditions due to the connection between the detector and the substrate across the thermopile fence.
- Radiation exchange with all telescope surfaces that are visible to the detector.
- The hexagonal detector initially at thermal equilibrium with the entire telescope.

The interaction between the system and its thermal processes is depicted in Figure 3.2.
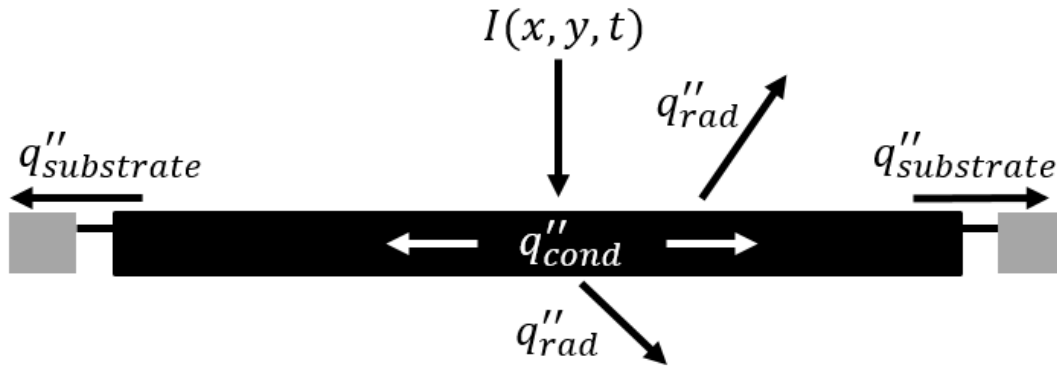
Figure 3.2. Heat flow diagram of the detector [3].

The instrument operates in the vacuum of space so the assumed model does not include effects due to convection. To develop the mathematical model, the conservation of energy principle is applied an infinitesimally small control volume, shown in Figure 3.3.
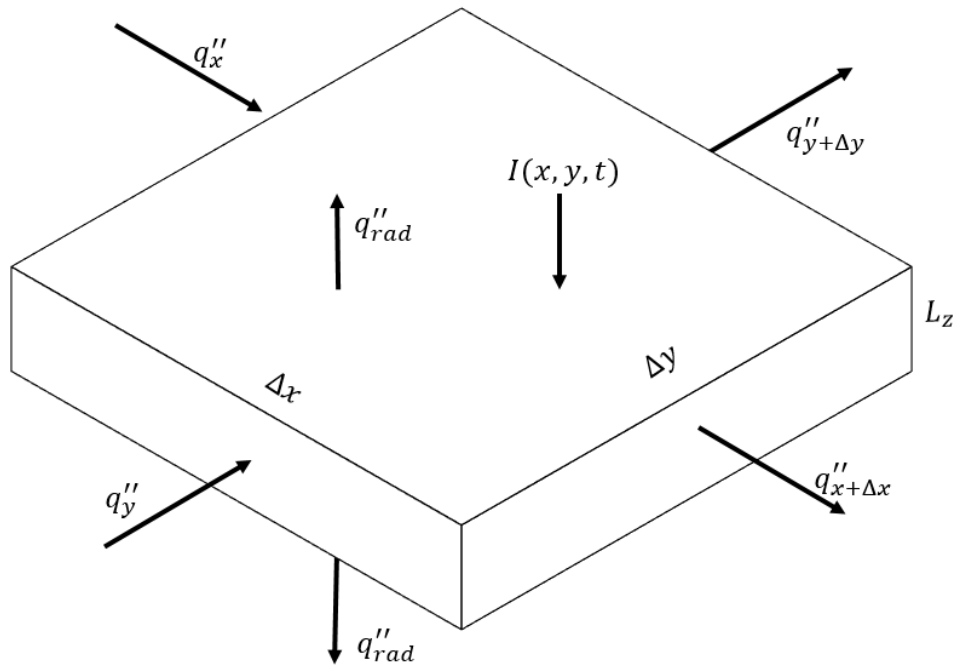
Figure 3.3. Heat fluxes on an infinitesimally small control volume.

Conservation of energy applied to the differential control volume in Figure 3.3 requires that

$$\rho c L_z \Delta x \Delta y \frac{\partial T}{\partial t} = q_x'' \Delta y L_z - q_{x+\Delta x}'' \Delta y L_z + q_y'' \Delta x L_z - q_{y+\Delta y}'' \Delta x L_z - 2 q_{rad}'' \Delta x \Delta y \qquad \textbf{(3.2)}$$

$$+ I(x, y, t) \Delta x \Delta y,$$

where

$$q''_{rad} = \epsilon\sigma(T^4 - T^4_{sur}) \tag{3.3}$$

and

$$q''_{x+\Delta x} \cong q''_x + \frac{\partial q''_x}{\partial x}\Delta x, \ q''_{y+\Delta y} \cong q''_y + \frac{\partial q''_y}{\partial y}\Delta y. \tag{3.4}$$

These heat fluxes are related to temperature using Fourier's rate law by

$$q''_x = -k_{ther}\frac{\partial T}{\partial x} \text{ and } q''_y = -k_{ther}\frac{\partial T}{\partial y}. \tag{3.5}$$

Dividing by the constant $\Delta x\Delta y$ and substituting the above relationships produces

$$\rho c L_z \frac{\partial T}{\partial t} = k_{ther}L_z\left(\frac{\partial^2 T}{\partial x^2} + \frac{\partial^2 T}{\partial y^2}\right) - 2\epsilon\sigma(T^4 - T^4_{sur}) + I(x,y,t), \tag{3.6}$$

where T is the absolute temperature (K), k_{ther} is the thermal conductivity (W/mK) and $I(x,y,t)$ is the absorbed surface radiation flux in (W/m^2).

The boundary condition is

$$-k_{ther}\frac{\partial T}{\partial \bar{\eta}} = h_{cont}(T - T_{sur}) \ , \tag{3.7}$$

$$\bar{\eta} \text{ on boundaries}$$

where $\bar{\eta}$ is the outward normal direction along the boundary of the sensor. This boundary condition is due to thermal contact with the substrate across the thermopile fence.

The initial condition for this system is

$$T(x,y,t) = T_{sur} \ , \ \ t = 0. \tag{3.8}$$

3.3 Radiant Heat Source

As seen in Equation 3.2, irradiation is modelled as an arbitrary heat source whose magnitude can vary in both space and time. Typically, irradiation will be determined independently using the Monte Carlo ray-trace (MCRT) method and then input directly into the detector model [27].

Because the radiation heat source is the most important input when modeling the detector, a brief overview of the MCRT method is presented here.

The MCRT method is a way of tracing a "bundle," or ray, of energy through an enclosure. Using this method, an enclosure, such as a telescope, is divided into a series of mathematical surfaces. A bundle of energy enters the enclosure through a port, such as a telescope aperture, following a given trajectory. The bundle continues propagating in the original direction until it is incident to with one of the mathematical surfaces, representing incidence to a real surface. Each surface has an absorptivity, based on its surface properties, that determines the efficiency with which the ray will interact with that surface. A random number is generated and is compared to the absorptivity to determine the outcome. If the absorptivity is larger than the random number, the ray is absorbed in that surface. Otherwise, the ray is said to be reflected along some new trajectory. The ray can undergo multiple reflections, but will eventually either be absorbed by a surface or exit the enclosure through an opening (e.g., exiting through the aperture). After a significant number of rays have been traced, one can accurately predict propagation of incident radiation through the telescope. The TRG has developed an extremely detailed model of the RBI telescope for this application. The power and position of rays arriving at the detector can be found using this model for a given Earth scene [27].

Because radiation travels at the speed of light, time is not involved in the MCRT method; everything occurs instantaneously. Each time the MCRT method is invoked the distribution of radiation is determined for a given Earth scene. In order to develop a transient heat source, one must string together results from the MCRT method for a sequence of Earth scenes.

3.4 Voltage Output

Ultimately, this model will convert incident irradiation into a voltage time series. To do this, the edge of the hexagonal detector is surrounded by a thermopile fence consisting of 898 *N*- and *P*-doped semiconductor junction pairs wired in series with a known Seebeck coefficient. The detector response is the output voltage from this thermopile fence. The thermocouples are distributed evenly around the hexagonal detector and the total output voltage is the sum of the individual junction pair voltages. The output voltage is

$$V = \alpha_s \sum_{n=1}^{N} \Delta T_n, \tag{3.9}$$

where α_s is the Seebeck coefficient (μV/K), and N is the number of thermocouple junction pairs. The voltage is expressed in terms of an average boundary temperature rise in the form

$$V = N\alpha_s \Delta T_{ave} \tag{3.10}$$

where

$$\Delta T_{ave} = \frac{\sum_{n=1}^{N} \Delta T_n A_{s,n}}{\sum_{n=1}^{N} A_{s,n}}. \tag{3.11}$$

4   Finite Volume Solution

4.1   Methodology Overview

While the detector model has been developed to convert incident radiation into a voltage signal, the detector model is only one piece of a larger puzzle. NASA assembled a multi-disciplinary team to develop an end-to-end radiometric system model of the RBI instrument [28]. This end-to-end model converts photons entering the telescope into digital counts, shown in Figure 4.1. As mentioned in Section 3.3, the TRG developed a detailed MCRT model of the RBI that converts the photons entering the telescope aperture into a power distribution on the detector. Next, this proposed detector model converts the incident power into a transient voltage. Downstream, an electronics device interprets this voltage signal to product digital counts.

Photons $\longrightarrow$ [Optical Module] — Power Distribution on Detector → [Focal-Plane Module] — Detector Output → [Electronics] → Digital Counts
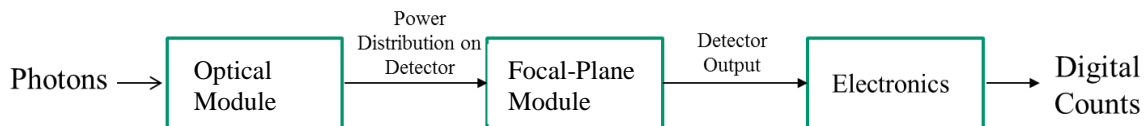
Figure 4.1. Information flow in the end-to-end radiometric model [28].

A finite volume (FV) solution has been used to determine the solution to the proposed detector mathematical model. The FV method is the standard for solving problems without analytical solutions, and many commercial codes are readily available to aid in solving these difficult problems. A few examples of these codes are COMSOL, FLUENT, and Thermal Desktop. Rather than use a commercial software, NASA has requested that each piece of the end-to-end model be developed in MATLAB. Using a common modelling software allows for seamless integration between the individual pieces. MATLAB is a very common platform for developing a FV code and open source scripts are available on the internet for use. However, the goal of the end-to-end model is to "develop a tool to enhance the interpretation of instrument performance" [28].   To support this goal, a program where every line of source code is clear and can be easily understood and modified by third-party users is needed. With this in mind, the TRG had to develop and test a FV code from the ground up. This way, if the physical instrument is found to be producing seemingly erroneous data, the user can easily modify the source code to try and replicate the phenomenon and use the model to aid in interpretation.

An internal team goal is to not only create a program that would be capable of solving the proposed mathematical model, but also sufficiently flexible to be adapted to some different application in the future. To meet this goal, the team has developed a "Library of Elementary Processes". The idea behind this library is to create a repository of functions where each function performs a single physical process. One can combine these single processes in a systematic manner to build a complex model. A simple example of the usefulness of this idea is presented. A client wants to model a situation for which he believes only radiation exchange is important. Assuming he has some knowledge of how to run the code, he would go to the library and call the function ΦRadiation that performs radiation. After examining the output, he may decide that he would like to investigate implementing a heat source into his model. Rather than starting from scratch, he can go to the library and add the function that treats volumetric sources, ΦSource, and quickly obtain his results.

In addition to allowing for rapid implementation of additional processes into a model, this method is beneficial because it can be used for any physical process. At its inception, the functions within the library are focused on thermal modelling. However, a process that models some chemical interaction or bacteria dynamic could be included. Initially, it would take some critical thinking to derive the details of the function, but once it has been developed, the process can be included in the library. Now, if a new situation arises that needs to utilize that process, it is readily available with no new development. Consider this simple example. Suppose the temperature of a device changes according to some mathematical operation at every step. A function called ΦMultplier might be developed. Figure 4.2 shows the implementation of this process in pseudocode. More complex processes are treated in the same manner as in this trivial example. This leads to tremendous modeling flexibility.

Library of Elementary Process: φMultiplier

Input Variables:

        Temperature_Old – Temperature of the Sample at the current, known time

        Multiplication_Coefficient – Parameter identifying the ratio between the new temperature and old temperature

Output Variables:

        Temperature_New – Temperature of the Sample at the future, to be determined time

Temperature Manipulation:

<p style="color:red; text-align:center;">Temperature_New = Multiplication_Coefficient · Temperature_Old</p>

Figure 4.2. Pseudocode representation of a simple function that could be added to the Library of Elementary Processes to treat temperature changes that are based on some multiplicative factor of its previously known value.

Ultimately, the algorithm has been developed to determine the solution of the proposed RBI detector model. For the purposes of this thesis, any discussion of the FV solution focuses on the processes in the Library of Elementary Processes that treat the thermal processes included in the mathematical model.

4.2 Mesh Development

As with any FV scheme, the modelled system must be discretized into a mesh, before the differential equations can be solved. As mentioned, an internal team goal is to develop a program capable of modelling the RBI detector while still allowing for flexibility in modelling a related future device. To meet this goal, the team started with a standard two-dimensional rectangular mesh, as illustrated in Figure 4.3. The rectangular mesh, with physical dimensions L_x-by-L_y, is divided into "ii" control volumes in the x-dimension and "jj" control volumes in the y-dimension, creating an ii-by-jj mesh. Following conventional nomenclature, the symbol "i" is the index used to designate control volumes in the x-direction where $i = 1, 2, …, ii − 1, \ ii$. Similarly, the symbol "j" is the index used to designate control volumes in the y-direction where $j = 1, 2, …, jj − 1, \ jj$.
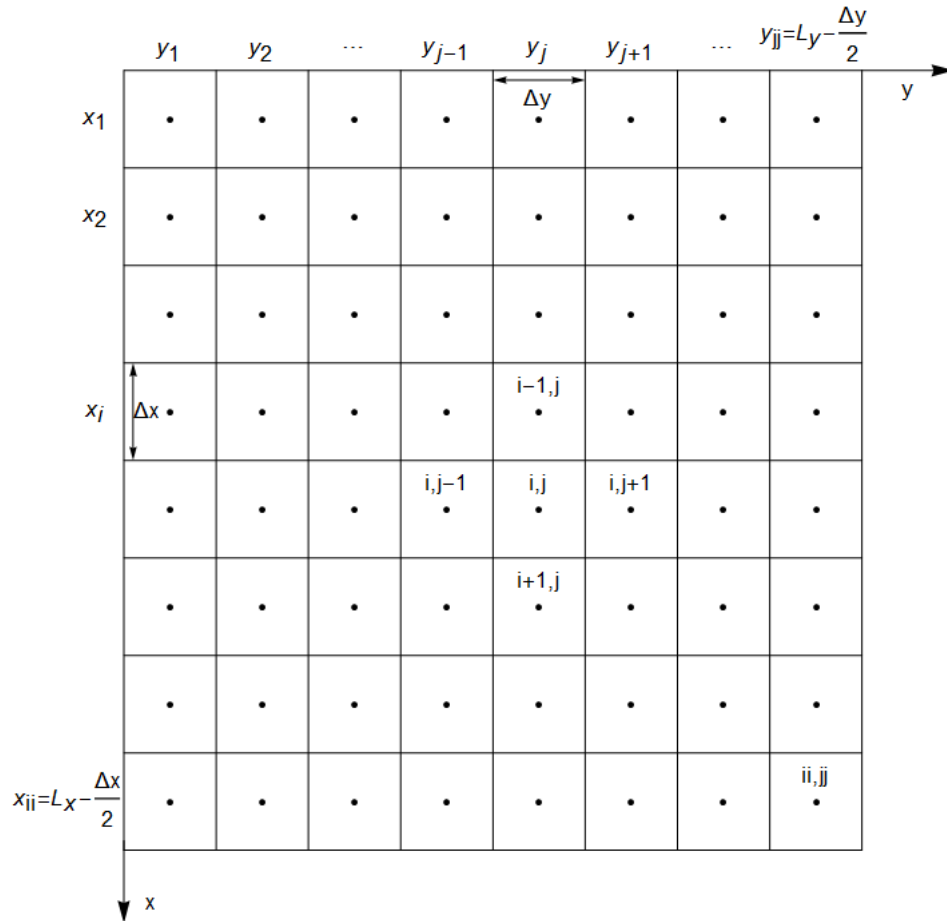
Figure 4.3. Schematic of a generic node-centered finite volume mesh.

This meshing technique works beautifully for modelling a rectangular surface. However, this rectangular mesh can still be used to model non-rectangular objects. This is done by controlling the properties of the control volumes to create a pixelated version of the non-rectangular object. As the mesh becomes more and more refined, the image begins to take shape. The process for creating a 1-mm octagon out of a rectangular mesh is presented.

- Start with a 1×1-mm rectangular mesh and determine how many control volumes to use. In this example we will use a 20×20 mesh, see Figure 4.4(a).

- Determine which cells need to be "removed" to create a non-rectangular object. A cell that is "removed" is effectively set to be insulated and no processes can occur in this cell. In the developed algorithm, those cells that are to be removed are referred to as "gaps." In Figure 4.4(b), these "gaps" have been identified by the red shading. For many shapes, a pattern-based algorithm can be developed to quickly identify the

gaps. For irregular shapes, care must be taken to identify the gaps and can become tedious.

- Remove the gaps to reveal a pixelated version of the octagon, see Figure 4.4(c).
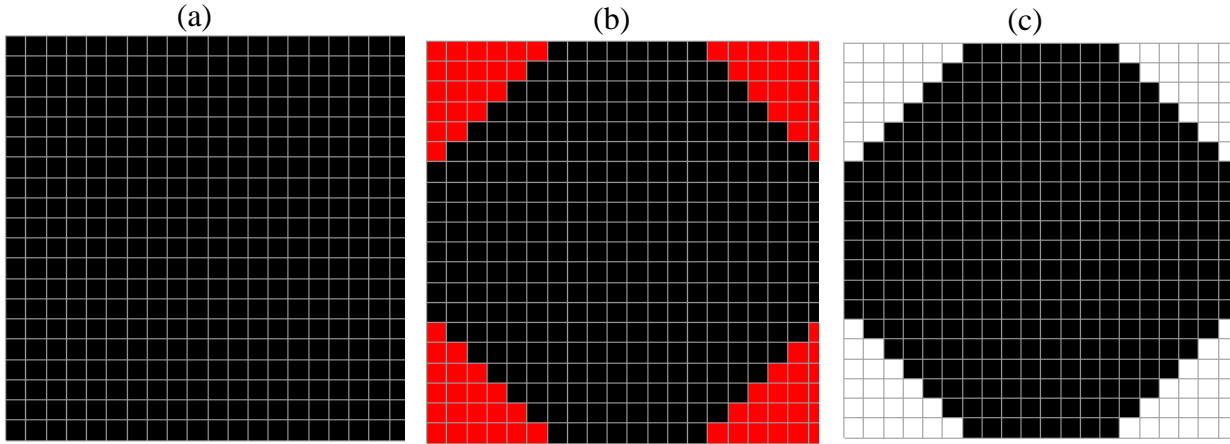
Figure 4.4. Example of creating a non-rectangular object in the rectangular mesh, (a) rectangular mesh from which an octagon will be created, (b) flagging the control volumes (red) that need to be removed to create the octagon, (c) final mesh used to model an octagon.

In the presented example, the image in Figure 4.4(c) begins to resemble an octagon, albeit a very jagged octagon. To improve the resolution of the image, a more refined mesh would be needed. As the mesh becomes more refined, the object becomes more defined. This presents an interesting dilemma for the user to consider. As the mesh becomes more refined, the computational time required to solve the solution increases. The user must find a compromise between resolution of the mesh and CPU time.

Now that the idea behind the mesh generation has been discussed, the focus turns to modelling the RBI detector. Constructing the detector from the rectangular mesh was relatively simple owing to its regular hexagonal shape. The detector itself was designed to have a 2:1 aspect ratio; that is, the tip-to-tip length is twice the side-to-side width. To reflect this, it was decided to use an ii-by-jj mesh specifically selected where $ii = 2 \cdot jj$. This discretization creates equal spacing between the center positions of control volumes in both the x and y dimensions, i.e $\Delta x = \Delta y$. It is important to note that this is not a requirement, just a logical simplification. Figure 4.5(a) shows an example of the selected rectangular mesh. The red outline represents the actual position of the detector. Figure 4.5(b) shows the detector after the gaps have been removed. Notice how the pixelated detector "steps" up the red line. Along the slanted segments, the mesh overshoots the

27

true detector area by including one control volume and then undershoots the true detector area by neglecting the next control volume. By refining the mesh, as seen in Figure 4.5(c), this overshooting effect becomes less noticeable due to smaller stepping increments.
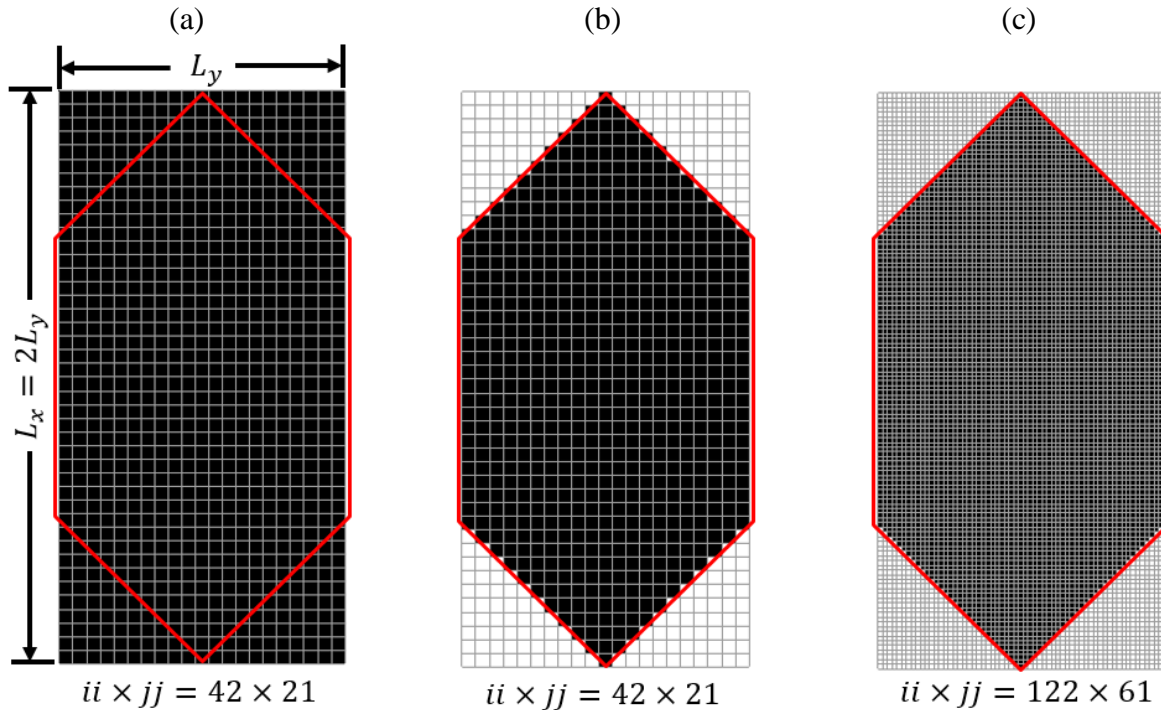
Figure 4.5. Mesh creation of the RBI detector, (a) depiction of detector dimensions and mesh dimensions required, (b) pixelated hexagonal detector using a 42-by-21 mesh, (c) pixelated hexagonal detector using a 122-by-61 mesh where the sloped edges match the true detector profile closely.

4.3 Library of Elementary Processes

In all of the cells that form the hexagonal detector, designated as black or red in Figure 4.6, the following processes from the Library of Elementary Processes are used:

- ΦConductionRectangular2D – Performs rectangular conduction with the four surrounding control volumes
- ΦSource – Applies a spatially and temporally varying volumetric heat source to a control volume
- ΦRadiation – Performs radiation exchange between a control volume and a constant-temperature surrounding

In boundary cells, designated exclusively by red in Figure 4.6, one additional process was added. This process, ΦBoundaryCondition, performs the interaction between the substrate and detector across the thermopile fence.

To incorporate initial conditions, each control volume, black or red in Figure 4.6, was initially set to the equilibrium temperature of T_{sur}. With the inclusion of these thermal processes, the model is ready to be solved.
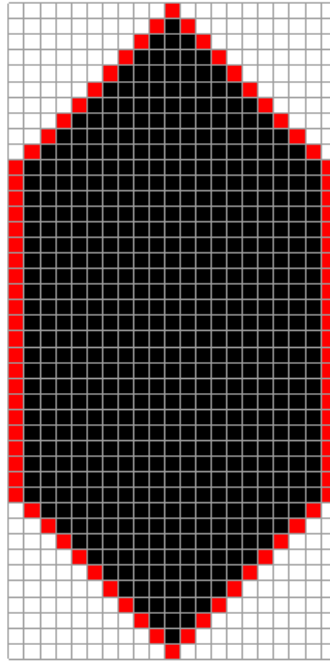
Figure 4.6. Distribution of boundary effects where red and black control volumes contain conduction, volumetric source, radiation exchange with red cells including boundary effect due to thermopile fence.

A description of the thermal processes, included in the Library of Elementary Processes, is presented in this section. Each of the processes has been using an implicit FV scheme in which it is as if no other process affected the control volume. That is, the change in temperature of the $(i,j)^{th}$ control volume over time, $\frac{dT_{i,j}}{dt}$, is due solely to the effect of the thermal process, Φ_1, represented as

$$\frac{dT_{i,j}}{dt} = \Phi_1.$$

(4.1)

Once the FV solution to this simple problem is found, it is stored in the library. To combine individual processes from the Library of Elementary Processes for use in a certain model, two logical options are available. If using a sufficiently small time step, we can implement a sequential, splitting method. For a given time step, the new temperatures are computed based on the previous time step values, $\vec{\mathbf{T}}^P$, assuming that only Φ_1 occurs. This result is stored as a sort of intermediate temperature for that time step. Φ_2 acts on these intermediate temperatures and overwrites the intermediate values. Once the final process, Φ_n, has occurred; the temperature returned is the final temperature for that time step, T^{P+1}. This splitting method is represented as

$$\vec{\mathbf{T}}^{P+1} = \Phi_1\left[\Phi_2\left[\dots\left[\Phi_n\left[\vec{\mathbf{T}}^P\right]\right]\right]\right].$$ (4.2)

This can introduce problems if the time step is too large. Additionally, the order in which the processes occur can influence the final results [29]. To avoid this issue, the second method, where solutions for each individual process are combined into one compound process, was implemented.

The solutions for each of the individual processes are presented in the following sections. For ΦConductionRectangular2D, the solution is developed from conservation of energy. To avoid repetition, only the final solution for the remaining processes is presented here.

4.3.1 ΦConductionRectangular2D

To develop the ΦConductionRectangular2D process, an energy balance on the control volume, shown in Figure 4.7, where only conduction is included requires

$$\rho c \mathrm{L}_z \Delta x \Delta y \frac{\partial T}{\partial t} = q_x - q_{x+\Delta x} + q_y - q_{y+\Delta y}.$$ (4.3)

Using a first-order Taylor series expansion on the $q_{x+\Delta x}$ and $q_{y+\Delta y}$ terms, the equation is rewritten as

$$\rho c \mathrm{L}_z \Delta x \Delta y \frac{\partial T}{\partial t} = q_x - \left(q_x + \frac{\partial q_x}{\partial x}\Delta x\right) + q_y - \left(q_y + \frac{\partial q_y}{\partial y}\Delta y\right).$$ (4.4)

where

$$q_x = q_x'' \mathrm{A} = \mathrm{q}_x'' \Delta y L_z \text{ and } q_y = q_y'' \mathrm{A} = \mathrm{q}_y'' \Delta x L_z.$$ (4.5)

These heat fluxes are related to temperature using Fourier's rate law by

$$q''_x = -k_{ther} \frac{\partial T}{\partial x} \text{ and } q''_y = -k_{ther} \frac{\partial T}{\partial y}. \tag{4.6}$$

Substituting these relationships into Equation 4.3, the two-dimensional heat diffusion equation becomes

$$\rho c \frac{\partial T}{\partial t} = k_{ther} \left(\frac{\partial^2 T}{\partial x^2} + \frac{\partial^2 T}{\partial y^2} \right). \tag{4.7}$$

Discretizing the equation using a second-order center-difference scheme in space and first-order backward difference in time, the solution for a typical interior node is obtained as

$$T_{i,j}^{P+1} - \alpha \Delta t \left(\frac{T_{i-1,j}^{P+1} - 2T_{i,j}^{P+1} + T_{i+1,j}^{P+1}}{\Delta x^2} + \frac{T_{i,j-1}^{P+1} - 2T_{i,j}^{P+1} + T_{i,j+1}^{P+1}}{\Delta y^2} \right) = T_{i,j}^P. \tag{4.8}$$

The discretization technique is the standard in finite volume solutions and a detailed explanation can be found Patankar's "Numerical Heat Transfer and Fluid Flow" [30]. This equation gives an implicit scheme to compute the temperatures simultaneously at time level p+1. A major advantage is its unconditional stability. This equation applies to every control volume and is linked to its immediate neighbors. If one of the surrounding control volumes is considered to be a gap, as discussed previously, no contribution is provided by that control volume and interface is treated as insulated. Therefore, the term contributed from that neighboring control volume drops out and the previous equation is simplified. The entire system of equations can be solved simultaneously to produce the new temperature values using only the temperature values from the previously known time step [31]. In matrix form Equation (4.8) can be written,

$$[\vec{T}^{P+1}] = [\Phi Cond2DCoef]^{-1}[\vec{T}^P]. \tag{4.9}$$
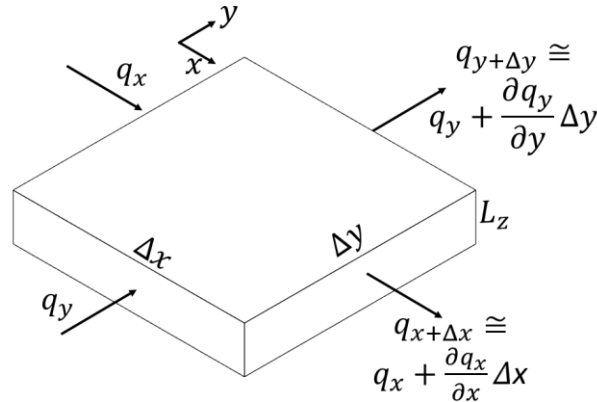
4.3.2 ΦSource

Conservation of energy on the control volume, shown in Figure 4.8, subjected only to a heat flux of magnitude I_c produces

$$\rho c \mathrm{L_z} \Delta x \Delta y \frac{\partial T}{\partial t} = I_c(t) \Delta x \Delta y. \tag{4.10}$$

Discretizing using an implicit scheme, the solution may be written

$$T_{i,j}^{P+1} = T_{i,j}^{P} + I_c(t) \frac{\Delta t}{\rho c L_z} = T_{i,j}^{P} + I_c(t) \cdot \Phi SourceCoef. \tag{4.11}$$
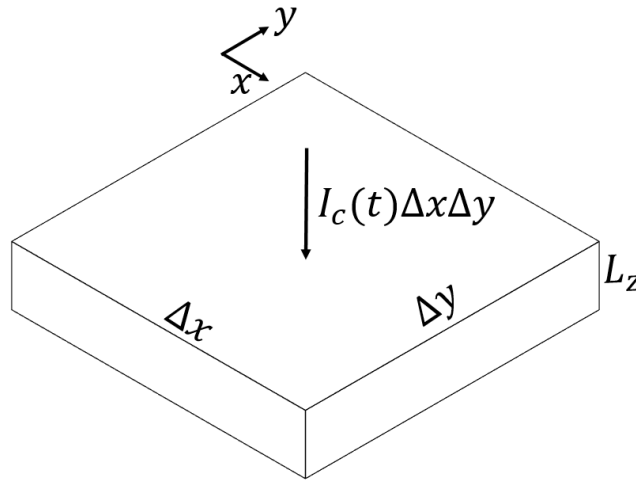
Figure 4.8. Control volume on which only a heat source affects the solution.

4.3.3 ΦRadiation

Conservation of energy on a control volume, shown in Figure 4.9, with only radiation exchange to surroundings at a constant temperature produces

$$\rho c \mathrm{L_z} \Delta x \Delta y \frac{\partial T}{\partial t} = -2 q_{rad}'' \Delta x \Delta y = -2 \Delta x \Delta y \epsilon \sigma (T^4 - T_{sur}^4). \tag{4.12}$$

Because a linear solver is used to compute the solution, the radiation term is linearized using a radiation heat transfer coefficient as

$$q''_{rad} = h_{rad}(T)(T - T_{sur}),$$ (4.13)

where

$$h_{rad}(T) = \epsilon\sigma(T^2 + T_{sur}^2)(T + T_{sur}).$$ (4.14)

Using this relationship and discretizing using an implicit scheme, the final solution is given as

$$T_{i,j}^{P+1} = \frac{T_{i,j}^P + \dfrac{2\Delta t}{\rho c L_z}h_{rad}(T_{i,j}^P)T_{sur}}{1 + \dfrac{2\Delta t}{\rho c L_z}h_{rad}(T_{i,j}^P)} = \frac{T_{i,j}^P + \Phi RadCoef(T_{i,j}^P) \cdot T_{sur}}{1 + \Phi RadCoef(T_{i,j}^P)}.$$ (4.15)
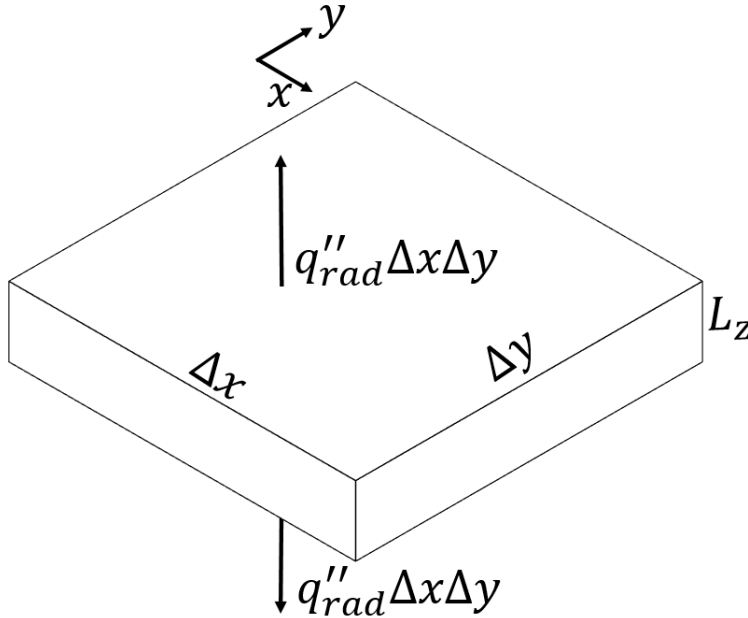
Figure 4.9. Control volume on which only a radiation exchange affects the solution.

The radiation heat transfer coefficient is computed in an explicit manner. That is, the coefficient is evaluated at the previous time step. It is important to note that this linearization method is allowed because of relatively small temperature differences between the detector and the surroundings. However, problems can arise when large temperature differences exist between the detector and the substrate. This is because the radiation solution becomes unstable and introduces numerical anomalies.

For instance, consider a system initially at equilibrium at a low temperature. This results in a low value of h_{rad}. Then a heat source causes the temperature of the detector to rise, at which point, the radiation heat transfer coefficient is re-evaluated. If the detector temperature has risen significantly above that of the surroundings the radiation coefficient, will be evaluated to a high

value. At the next time step, the radiation term will dominate and return the temperature of the detector to the equilibrium position, restarting this cycle. However, this instability can be eliminated by using a smaller time step. For the RBI application, this is not an issue. Caution should be used if modelling a system under conditions that could create an unstable radiation coefficient.

4.3.4 ΦBoundaryCondition

For boundary nodes, conservation of energy applied to a control volume where the only effect is a heat loss due to the thermopile fence, shown in Figure 4.9, produces

$$\rho c L_z \Delta x \Delta y \frac{\partial T}{\partial t} = -h_{cont} A_{cont}(T - T_{sur}). \tag{4.16}$$

Here, A_{cont} is the area with which the thermopile fence is in contact with. As mentioned in Section 3.1, it is assumed that the thermopile fence spans the entire side face. Discretizing in an implicit manner, the solution is given as

$$T_{i,j}^{P+1} = \frac{T_{i,j}^{P} + \frac{A_{cont}\Delta t}{\rho c L_z \Delta x \Delta y} h_{cont} T_{sur}}{1 + \frac{A_{cont}\Delta t}{\rho c L_z \Delta x \Delta y} h_{cont}} = \frac{T_{i,j}^{P} + \Phi BCCoef \cdot T_{sur}}{1 + \Phi BCCoef}. \tag{4.17}$$

$$h_{cont} A_{cont}(T - T_{sur})$$
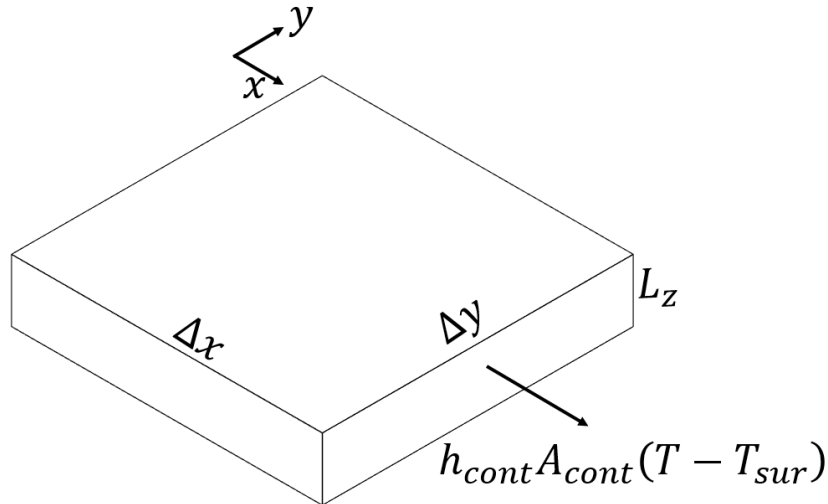
Figure 4.10. Control volume on which only thermal contact along the boundary affects the solution.

4.3.5 Compound Process Solution

To avoid any time step restrictions inherent to the splitting method, the individual processes were added together to create one compound process. The linearity of the problem makes this compound process easy to formulate. This process is given as

$$[\Phi Cond2DCoef + \Phi RadCoef(T^P) + \Phi BCCoef][\vec{T}^{P+1}]$$
$$= [\vec{T}^P + \Phi RadCoef(T^P)T_{sur} + \Phi BCCoefT_{sur} + I_c(t)\Phi SourceCoef]. \tag{4.18}$$

This compound process can be solved at every time step to produce the transient solution using a linear solver such as "mldivide" in MATLAB. In Equation 4.9, the variables $\Phi Cond2DCoef$, $\Phi SourceCoef$, and $\Phi BCCoef$ are constants. To reduce overall computational time, these constants are computed once and them used throughout the code.

4.4 Voltage

Ultimately, the voltage is the most critical quantity that the detector model must compute. The voltage is computed as the average boundary temperature rise multiplied by the total number of thermocouples and the effective Seebeck coefficient. Therefore, the voltage is a post-processed quantity that requires the transient temperature solution. At a given time step, the temperatures at the boundary control volumes, identified by red squares in Figure 4.11, are computed. The boundary area weighted average temperature is computed. These temperatures are weighted by their respective boundary area due to the construction of the thermopile fence. All of the thermopile junctions are evenly spaced around the perimeter of the detector. Over the same size segment of the detector, a sloped section contains $\sqrt{2}$ more thermocouples than a vertical section. As a result, in the meshed environment, the temperatures in control volumes along the sloped sections are weighted $\sqrt{2}$ times the vertical segments. The tips are weighted $2\sqrt{2}$ times a vertical segment to compensate for the fact that the tips come to a point and have two sloped areas to which thermopiles are attached.
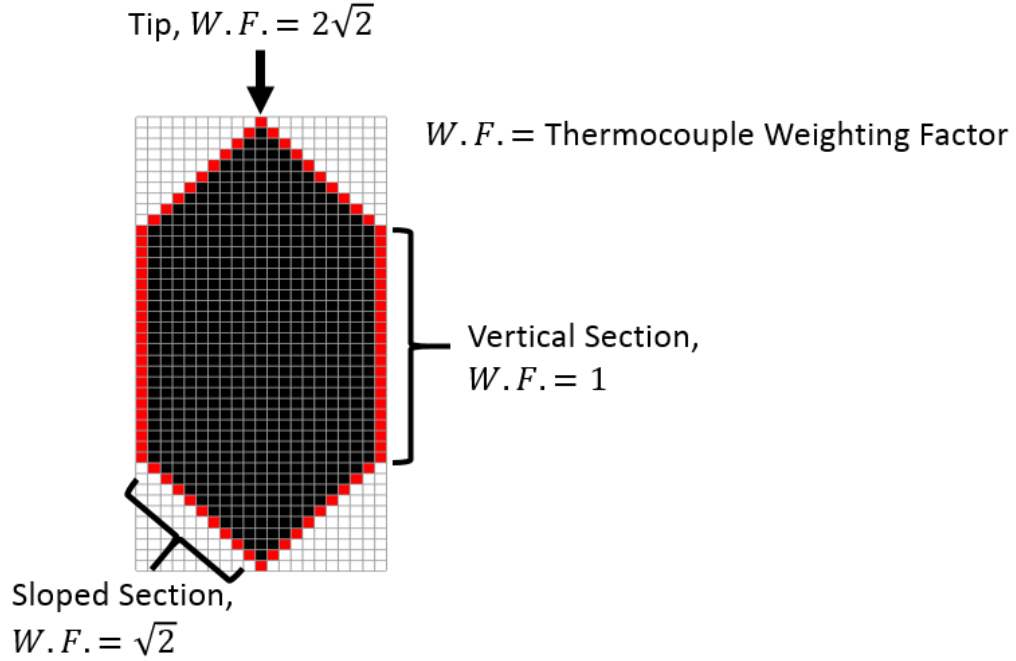
Figure 4.11. Meshed detector with control volumes used to compute voltage flagged in red.

Using this idea, the voltage computed in the discretized detector model is represented as

$$V(t) = \alpha_s N \frac{\sum_{n=1}^{N_{Bound}} (T_n(t) - T_{surr}) A_{s,n}}{\sum_{n=1}^{N_{Bound}} A_{s,n}}, \qquad (4.19)$$

where N_{Bound} is the number of boundary control volumes, A_n is the contact area (weighted as described above) for a given boundary node, and N is the total number of thermocouples.

4.5 Code Logic Block Diagram

While the MATLAB code is included in Appendix A, a flow chart diagram is presented to help the reader understand the code.
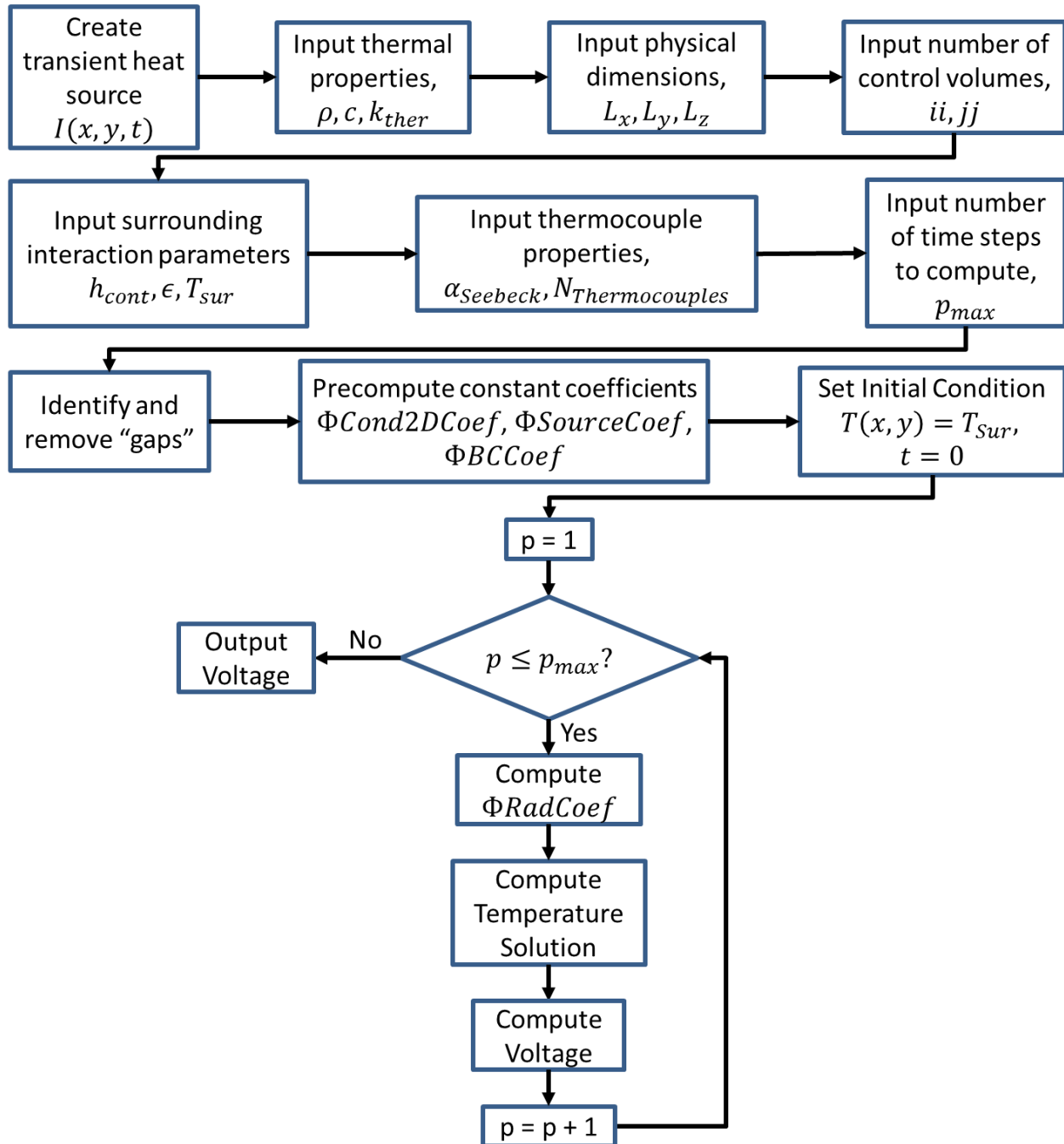
Figure 4.12. Logic block diagram of developed MATLAB algorithm to compute RBI voltage.

5   <u>Numerical Solution Studies</u>

To better understand the relationship between input parameters and voltage response, case studies were performed on the developed model. The case studies performed are mesh dependence, effect of h_{cont}, effect of incident source location, and the effect of scanning. For these case studies, the detector was assumed to be made of pure gold with a thin layer of gold-black deposited on the upper surface. While this is not representative of the RBI detector, it is acceptable for testing the developed model to determine how the parameters effect the solution.

5.1   Case Study Simplifications

For these case studies, some model simplifications were made to allow for easier interpretation of results. A logical simplification was to use a well-defined heat source, rather than true data from the MCRT method. Using the MCRT method, the magnitude of the heat source would vary depending on the earth scene that is being observed at each time step. Instead, the incident radiation is modelled as

$$I(x, y, t) = I_c \cdot [H(x - x_1(t)) - H(x - x_2(t))]$$
$$\cdot [H(y - y_1(t)) - H(y - y_2(t))] \cdot [H(t - t_{on}) - H(t - t_{off})],$$

(5.1)

where H is the unit step function. With this function, we can systematically control the individual components of the heat source. For instance, by adjusting x_1 and x_2, we can move the heat source location without changing anything else. Then, when comparing results, we know that any differences between results are due purely to the location change of the heat source. In a practical sense, this type of heat source of constant magnitude would correspond to looking at a very uniform body, such as the desert or an ocean.

Additionally, in order to possibly simplify the thermal model for these case studies, the relative influence of the radiation term, from Equation 3.6, is explored. If we assume that the system is at steady-state ($\frac{\partial T}{\partial t} = 0$) and the lumped capacity assumption is valid ($\nabla^2 T = 0$), an energy balance on the entire sensor produces

$$A_s I(x, y, t) = 2 A_s \epsilon \sigma (T^4 - T_{sur}^4) + A_{cont} h_{cont} (T - T_{sur}).$$

(5.2)

The heat input due the radiation is dissipated by the combined effects of radiation to the enclosure and contact with the substrate acting in parallel. Expressing the radiation term using the radiation heat transfer coefficient defined by

$$h_{rad}(T) = \epsilon\sigma(T^2 + T_{sur}^2)(T + T_{sur}),$$ (5.3)

Equation 5.2 can be solved for the approximate steady temperature rise as

$$T - T_{sur} = \frac{A_s I(x, y, t)}{2A_s h_{rad}(T) + A_{cont}h_{cont}}.$$ (5.4)

For typical parameter values in an earth radiation budget instrument with $T \sim T_{sur} \sim 300K$, we can estimate the order-of-magnitude of the terms as

$$2A_s h_{rad}(T) \sim 10^{-5} \left(\frac{W}{K}\right),$$

$$A_{cont}h_{cont} \sim 10^{-3} \left(\frac{W}{K}\right).$$ (5.5)

Since the contact conductance contribution is about two orders of magnitude greater than the radiation contribution for this application, the radiation term can be neglected, in which case, the energy equation, Equation 3.6, reduces to

$$\rho c \frac{\partial T}{\partial t} = k_{ther} \left(\frac{\partial^2 T}{\partial x^2} + \frac{\partial^2 T}{\partial y^2}\right) + \frac{1}{L_z} I(x, y, t).$$ (5.6)

5.2 Dimensionless Form

In addition to simplifying the model to make results easier to interpret, the case studies were done in dimensionless form. This was done so that when the actual RBI parameters have been determined, the results could be rescaled. The system is put expressed dimensionless form using the parameters I_c, k, α, and L_x as reference quantities. The following dimensionless variables are formed using these reference quantities:

$$\theta = \frac{T - T_{sur}}{I_c L_x / k_{ther}}, x^+ = \frac{x}{L_x}, y^+ = \frac{y}{L_x}, t^+ = \frac{t\alpha}{L_x^2}.$$ (5.7)

In dimensionless form, the energy equation, Equation 5.6, then becomes

$$\frac{\partial \theta}{\partial t^+} = \nabla^2 \theta + \frac{1}{L_z^+} I^+(x^+, y^+, t^+). \tag{5.8}$$

The dimensionless form of the boundary condition, Equation 3.5, is

$$-\frac{\partial \theta}{\partial \bar{\eta}^+} = h_{cont}^+ \theta, \quad \bar{\eta}^+ \ on \ boundaries. \tag{5.9}$$

The dimensionless form of the initial condition, Equation 3.6, is

$$\theta(x^+, y^+, t^+) = 0, \qquad t^+ = 0. \tag{5.10}$$

The dimensionless voltage is

$$V^+(t^+) = \frac{V}{N\alpha_s I_c \, L_x/k_{ther}}. \tag{5.11}$$

The dimensionless parameters for this system are

$$I^+ = \frac{I}{I_c} \tag{5.12}$$

$$h_{cont}^+ = h_{cont} \frac{L_x}{k_{ther}} \tag{5.13}$$

$$L_y^+ = \frac{L_y}{L_x}, \quad L_z^+ = \frac{L_z}{L_x} \tag{5.14}$$

$$x_1^+ = \frac{x_1}{L_x}, \quad x_2^+ = \frac{x_2}{L_x}, \quad y_1^+ = \frac{y_1}{L_x}, \quad y_2^+ = \frac{y_2}{L_x}. \tag{5.15}$$

5.3 Mesh-Dependence

The first case study performed was a mesh-dependence study. In order to report meaningful results, one must make sure that the results are independent of the selected mesh. That is, using a more refined mesh should not change significantly the solution. Because non-rectangular objects are formed as pixelated versions of the object, this mesh-dependence study becomes paramount. As the mesh becomes more refined, the pixelated object begins to resemble the true shape. Additionally, the boundary surface area and total volume begin to converge to values corresponding to the real object. The goal is to determine the coarsest mesh that can be used to produce converged results.

To perform the mesh-dependence study, solutions using four different mesh sizes under identical conditions were computed. The four mesh sizes will be referred to as coarse (6×3),

medium (18×9), fine (54×27), and ultra-fine (162×81). Table 5.1 shows a comparison between the surface area and volume of the pixelated detector at different mesh sizes, as well as the real detector. Because the voltage output and boundary loss effect are directly dependent on the boundary surface area, numerical differences between results at different mesh sizes are purely mesh dependent and not physical. Ideally, a super fine mesh would be selected and used for all cases. But this is a game of diminishing returns. Once the mesh has converged, any finer mesh just adds additional computational time for insignificant increases in accuracy.

Table 5.1. Comparison of dimensional properties of a pixelated detector, at different mesh levels, with the physical detector.

	Coarse (6x3)	Medium (18x9)	Fine (54x27)	Ultra-Fine (162x81)	Physical
L_x^+	1	1	1	1	1
L_y^+	0.5	0.5	0.5	0.5	0.5
L_z^+	0.1	0.1	0.1	0.1	0.1
$\Delta x = \Delta y$	0.3333	0.1111	0.0370	0.0123	N/A
Number of gaps	4	40	364	3280	N/A
Boundary Area	0.2552	0.2460	0.2430	0.2419	0.2414
Total Volume	0.03889	0.03765	0.03752	0.03750	0.03750

In each case the same heat source is incident on identical areas of the detector. The parameters used for this case study can be found in Table 5.2. For each case, the solution was computed until the steady state had been reached using a very fine time step (1000 Hz sampling rate). This was done to ensure that the time step does not introduce any numerical inaccuracies. Figure 5.1 shows the dimensionless voltage for each of the four cases. The difference is noticeable between the dimensionless voltages compute using the coarse (Δx) and the medium ($\frac{\Delta x}{3}$) meshes. However, this difference is less significant between the remaining meshes.

Table 5.2. Parameters used for mesh-dependence study.

Parameter	Value
L_y^+	0.5
L_z^+	0.1
x_1^+	0.333
x_2^+	0.494
y_1^+	0.166
y_2^+	0.5
t_{on}^+	0.327
t_{off}^+	∞
h_{cont}^+	1
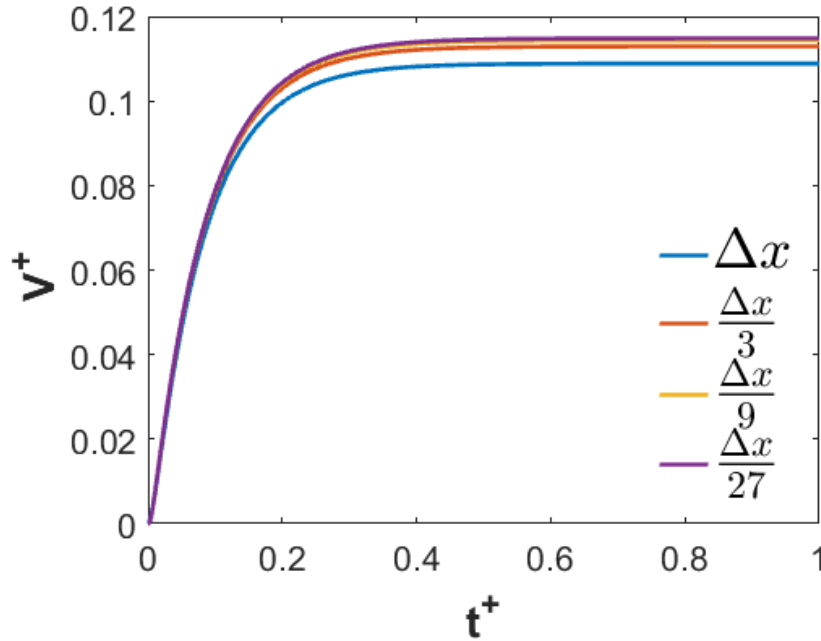
Figure 5.1. Dimensionless voltage produced at four increasingly refined mesh levels.

An acceptance criteria was needed to determine the coarsest allowable mesh. We decided to consider that the mesh was converged when the relative change between the dimensionless voltage produced with a given mesh, V_n^+, and that produced with the more refined mesh, V_{n+1}^+, was within a specified tolerance, ε_{Tol}. This criterion can be expressed as

$$\Delta V^+_{Rel} = \frac{V^+_{n+1} - V^+_n}{V^+_n} \le \varepsilon_{Tol}. \tag{5.16}$$

This relative change was computed for each of the mesh refinement levels, and the results are shown in Figure 5.2. The three curves represent the relative change when going from a coarse mesh to a medium mesh (blue), from a medium mesh to a fine mesh (orange) and from a fine mesh to an ultra-fine mesh (yellow). Based on a tolerance of $\varepsilon_{Tol} = 0.02$, the coarse mesh is not sufficient to produce mesh-independent results since the relative change between the coarse and medium meshes exceeds the acceptable tolerance. However, when the mesh is refined from a medium mesh to a fine mesh, the relative change is less than the acceptance criteria. We conclude that the medium mesh is the coarsest mesh that can be used to produce mesh-independent results.
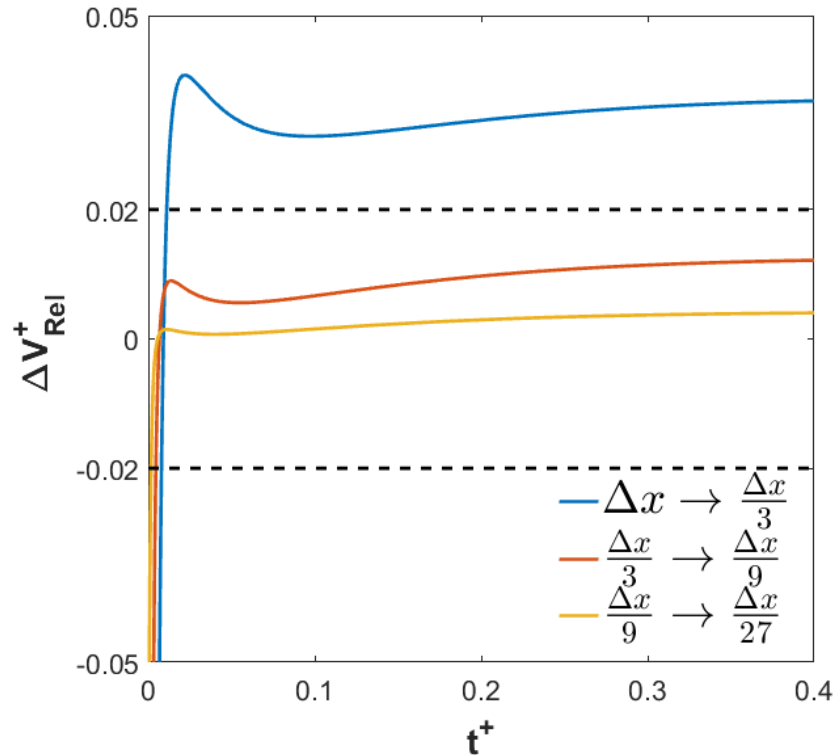
Figure 5.2. Relative change in dimensionless voltage when going from a coarse to medium mesh (blue), medium to fine mesh (orange), and fine to ultra-fine mesh (yellow).

It is worth noting that when going from a fine mesh to the ultra-fine mesh, almost no relative change occurs in dimensionless voltage. One could argue that a fine or ultra-fine mesh would make more sense. However, as mentioned previously, this is a problem with diminishing returns. On the computer that was used for all test cases, the medium mesh solution took 0.67 s to compute. Compared to the time required to compute the medium grid solution, the fine and ultra-fine mesh solutions took approximately 47 and 3800 times longer to run, respectively. There is no need to wait longer with marginal increases in accuracy. While an 18-by-9 mesh is the coarsest allowable, for the remaining case studies a 42-by-21 mesh was used to incorporate a factor of safety.

5.4   Effect of h_{cont}

Sections 5.4 – 5.6 are reprinted with slight editing with permission from "Thermal Analysis of the Sensor in a Radiation Budget Instrument" by Pfab et al. from the proceedings of the 2017 Summer Heat Transfer Conference. Copyright © 2017 by ASME.

The accuracy of any model is directly related to how well the input parameters for the model are defined. For this model, the parameters that must be defined are the physical properties of detector, the incident radiation, and the magnitude of the heat transfer coefficient, h_{cont}^+, due to the thermal contact with the substrate across the thermopile fence surrounding the detector. As the properties of gold have been well documented in the literature, the confidence is high that these parameters are well defined. Using methods such as the MCRT method to model the radiation source [27], the magnitude of the incident irradiation arriving at the detector can be very accurately known.

With regards to the h_{cont}^+ parameter, it is difficult to accurately predict what the magnitude of the h_{cont}^+ should be. A separate analysis of the thermopile would need to be performed in order to obtain an accurate magnitude of this coefficient. The magnitude of h_{cont}^+ is important because it protects the sensor from burning up while allowing its temperature to rise sufficiently providing a significant output voltage. If the magnitude is too low, there would not be an effective heat loss mechanism and the temperature of the detector would continue to grow, potentially causing damage to the detector. Conversely, if the magnitude is too high, any incident radiation is immediately transferred out of the system and no temperature rise is apparent. This is problematic since a time variant voltage response is recorded based on the temperature difference between the

sensor and the substrate. If no temperature rise is apparent, ultimately, no voltage response is output.

A case study was performed to determine a value of h_{cont}^+ that would provide realistic results. Since an exact value is not known, mathematically convenient values of h_{cont}^+ were used. Four solutions were computed using h_{cont}^+ values of 0.1, 1, 10 and 100, corresponding to effectively zero, small, medium and large h_{cont}^+. The dimensionless parameters used for all the test cases can be found in Table 5.3. For this test case, the radiation source was assumed uniform over the entire hexagonal sensor grid.

Figure 5.3Figure 5.4 shows the temperature distribution across the sensor after a long period of time. The temperature rise for the small, medium and large h_{cont}^+ values (1, 10, 100) have reached steady state, but the effectively zero value (0.1) has not. As the h_{cont}^+ value gets increasingly larger, the difference between the maximum temperature rise (located at the center) and the temperature rise along the boundary becomes more apparent. The gradient in the temperature rise distribution is indicative of this effect.

Table 5.3. Dimensionless parameters used to compute model solution.

Parameter	Value
L_y^+	0.5
L_z^+	0.1
x_1^+	0
x_2^+	1
y_1^+	0
y_2^+	0.5
t_{on}^+	0
t_{off}^+	∞
h_{cont}^+	0.1, 1, 10, 100

Figure 5.4 shows the transient output voltage for each of the four test cases. When h_{cont}^+ is effectively zero, the voltage continues to rise with a constant slope but is clipped in Figure 5.4 to show a comparison of the 3 remaining values. For large h_{cont}^+ values, the voltage output is almost negligible and the sensor reaches steady state almost instantly. Conversely, a small h_{cont}^+ value has

a relatively slow rise time and a large voltage output. For a radiation budget instrument, an output voltage sufficiently significant to overcome the signal-to-noise ratio and a time constant sufficiently low to reach steady state during the scanning sequence is important. Based on these design necessities, a medium h_{cont}^{+} value of 10 is chosen for the remaining analysis. As expected, Figure 5.3 and Figure 5.4 show h_{cont}^{+} to be critical to the accuracy of the model. Further investigation is needed.
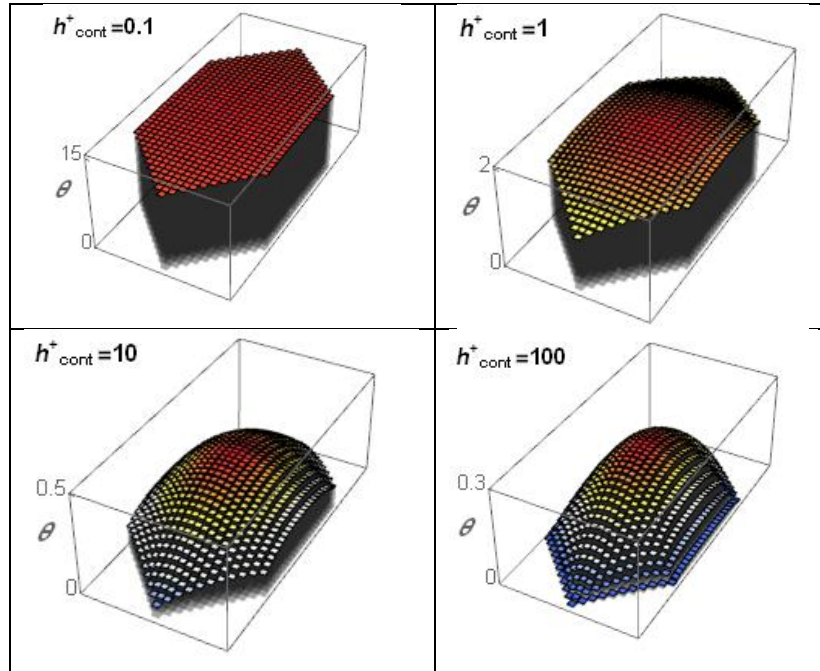
Figure 5.3. Temperature rise distribution for various values of h$^+$$_{cont}$ at steady state.

Figure 5.4. Dimensionless voltage for various values of h$^+$$_{cont}$.
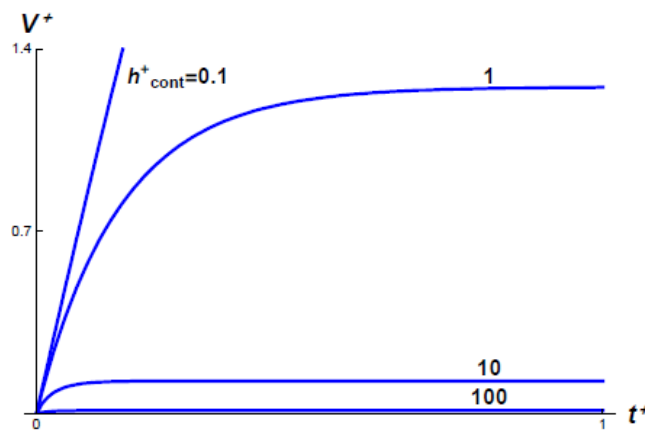
5.5 Effect of Source Location

To test the limitations of the model, an extreme illumination case was developed where all of the radiation is focused into a small area. For this case study, the total radiation source is concentrated into one finite volume control volume. In the previous example, $I(x,y,t)$ was incident on all of the 662 cells comprising the hexagonal grid. To keep the total energy the same for all cases, all the incident radiation was placed into one cell. Three locations; the cell at the center of the detector, a cell along the side of the detector, and a cell at the tip of the detector are chosen since these locations cover the total spectrum of possibilities. The center cell has four conduction paths and no boundary effects covering any interior point location. The side has one boundary effect area and three conduction paths. The tip has two boundary effect areas and one conduction path. Note that a true detector comes to a triangle but mesh consists of square cells: thus only the left and right sides of the tip cell are chosen as boundary areas and the top of the tip cell is effectively insulated. Figure 5.5 illustrates these conduction paths and boundary effect locations for the three unique locations.
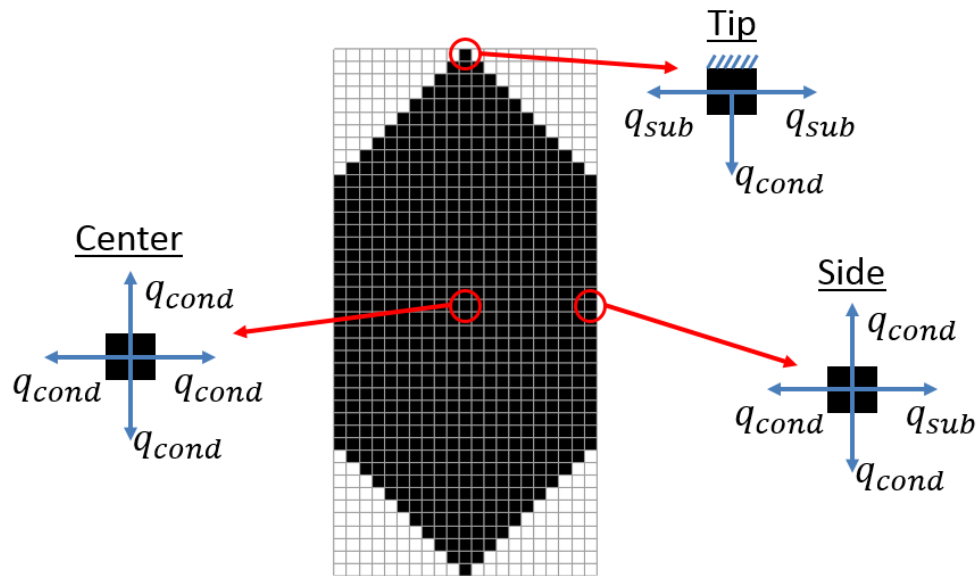
Figure 5.5. Schematic of conduction paths and boundary effect locations for three unique control volume locations: tip, side, and center.

The parameters used in Table 5.3 are the same parameters used for this case study. However, as mentioned previously, $h_{cont}^+ = 10$ was selected for the remaining cases. Figure 5.6 shows the locations of the radiation on the hexagonal detector as well as the steady-state temperature for each source location. The range of the temperature rise is clipped on the tip plot

to maintain the same graph scale. Figure 5.7 shows the voltage response for the three source locations. Early on, the three curves are very different but converge to the same value of 0.12. When the source is located at the center, time, corresponding to the delayed rise time, is needed for the heat to dissipate through the sensor. Conversely, at the tip and side an instantaneous voltage output occurs as these cells are directly in contact with a thermopile junction. Because all steady-state voltages converge to the same value, the position of the source does not affect the final result; however, if one is intererested in the early voltage transients, the location of the incident irradiation is important when interpreting the voltage data.
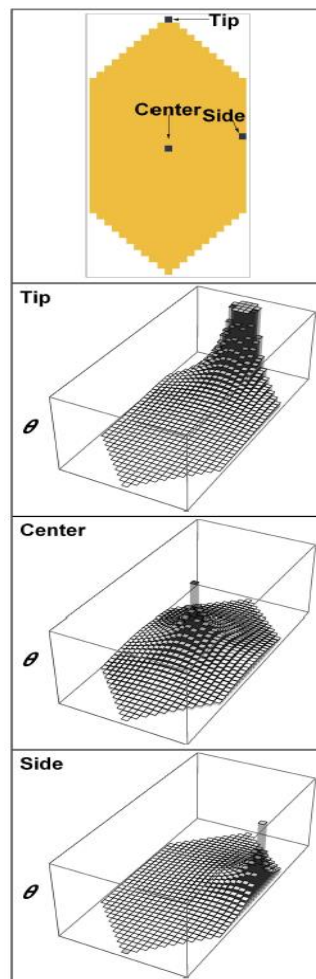
Figure 5.6. Steady-state temperature rise distribution for heat source locations at tip, center and side.
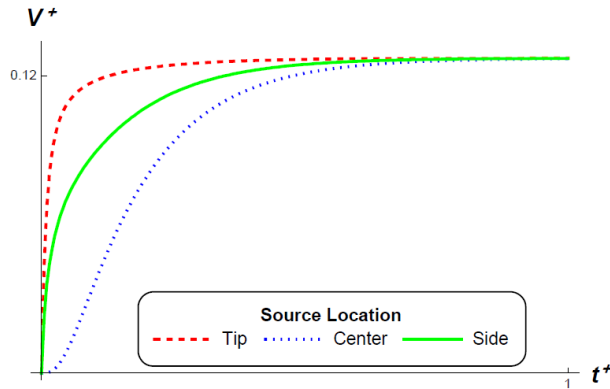
Figure 5.7. Dimensionless voltage for heat sources concentrated at the tip, center and side of a hexagonal detector.

5.6   Effect of Scanning

In general, a radiation budget instrument operates in a scanning sequence. During this sequence, the detector starts with its field-of-view occupied by empty space and then sweeps across the earth until it is once again regarding only space. It then reverses direction and sweeps back across the earth. This comprises one scanning sequence. A typical scanning sequence is shown in Figure 5.8. Shown is the telescope angle with respect to the earth limit angle, so that between ±1 the sensor is regarding the earth and registering a voltage. While the detector is scanning side to side, the satellite continues to travel through space. As a result, the position of the source moves both across the sensor and along the sensor.
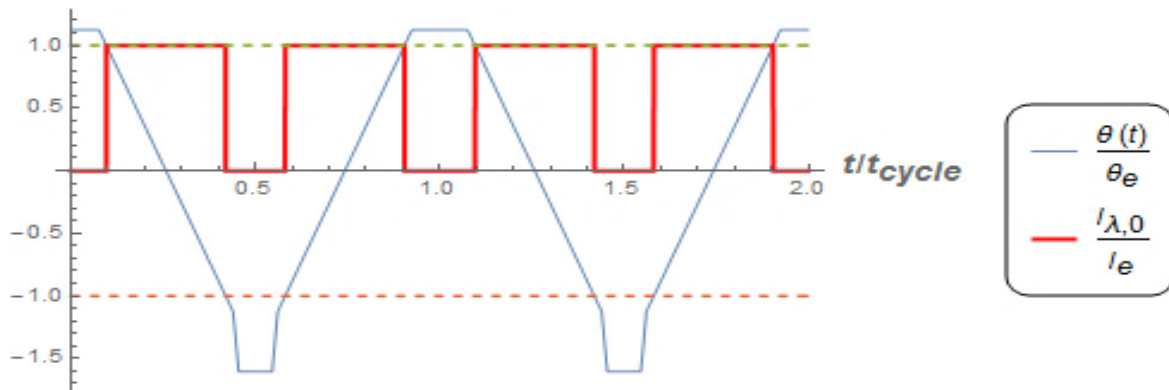
Figure 5.8. Incident radiation over two cycles of a standard earth scan sequence as a function of telescope cross-track scan angle.

5.6.1   Extreme Illumination Scan

To simulate this scanning phenomenon, the extreme illumination case is revisited. Using the parameters in Table 5.3, the extreme case with a moving heat source, rather than a stationary

heat source, is investigated. Figure 5.9 shows the heat source path for 2.5 cycles, designated by the black line in the top frame. Additionally, Figure 5.9 illustrates the instantaneous temperature rise at three indicated time instances. As before, the temperature rise at the source location is clipped to render the surrounding effects are visible.
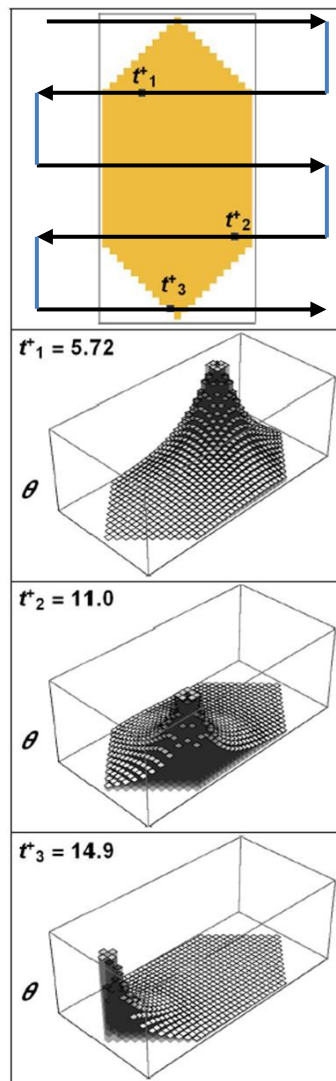
Figure 5.9. Extreme illumination scanning sequence and instantaneous temperature rise distributions at specific times during the sequence.

Figure 5.10 shows the nondimensional voltage during the scanning sequence. The first and last voltage spikes are smaller in width because the source does not sweep across the full width of the sensor. The three middle spikes pass across the full width of the sensor and produce similar curves.
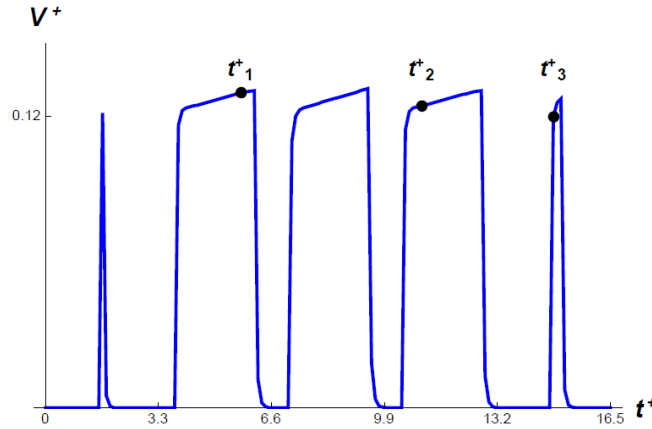
Figure 5.10. Dimensionless voltage for extreme illumination scanning sequence.

5.6.2 Typical Earth Scan

While the concentrated source case demonstrates the robustness of the mesh and method, a more practical case study is presented. For real applications, the sensors are small, resulting in very uniform temperature rise distributions across the sensor. Table 5.4 shows realistic parameters for a gold sensor used in a radiation budget instrument. Results using the typical parameters in Table 5.4 and the dimensionless parameters discussed in Table 5.3 are compared in the following study.

Table 5.4. Values representative of a typical RBI sensor.

Parameter	Value
$\rho, \dfrac{kg}{m^3}$	19,300
$c, \dfrac{J}{kg \cdot K}$	129
L_y, mm	1
$h_{cont}, \dfrac{W}{m^2}$	10^5
$\alpha, \dfrac{m^2}{s}$	1.27×10^{-4}
L_x, mm	2
L_z, mm	0.03
$I_c, \dfrac{W}{m^2}$	30

To model a typical earth scan sequence, a "coastline scan" was chosen. During this scenario, the magnitude of the radiation is very uniform across the illuminated portion of the sensor. The left panels in Figure 5.11 show the illuminated portions (in black) of the sensor at different instances during the first half-cycle. In this case, the heat source is moving from left to right. The second half-cycle corresponds to the source moving from right to left across the sensor. The sensor becomes illuminated in vertical columns of the mesh as the source moves across the width of the sensor. The sensor is fully illuminated as the source moves across the sensor until it begins to lose sight of the coastline and the line source begins leaving the sensor in vertical columns of the mesh.

Figure 5.11 additionally shows the temperature rise distribution at different instances during the first half of a typical earth scan cycle for both dimensionless and typical parameters. The temperature rise for typical parameters is much more uniform than that for dimensionless parameters. For the dimensionless parameters, in the first and last row, the heat source location is very noticeable as indicated by the gradients at those locations. However, for the typical parameters the temperature rise is much more uniform, and thus the location of the heat source is not as evident.

52
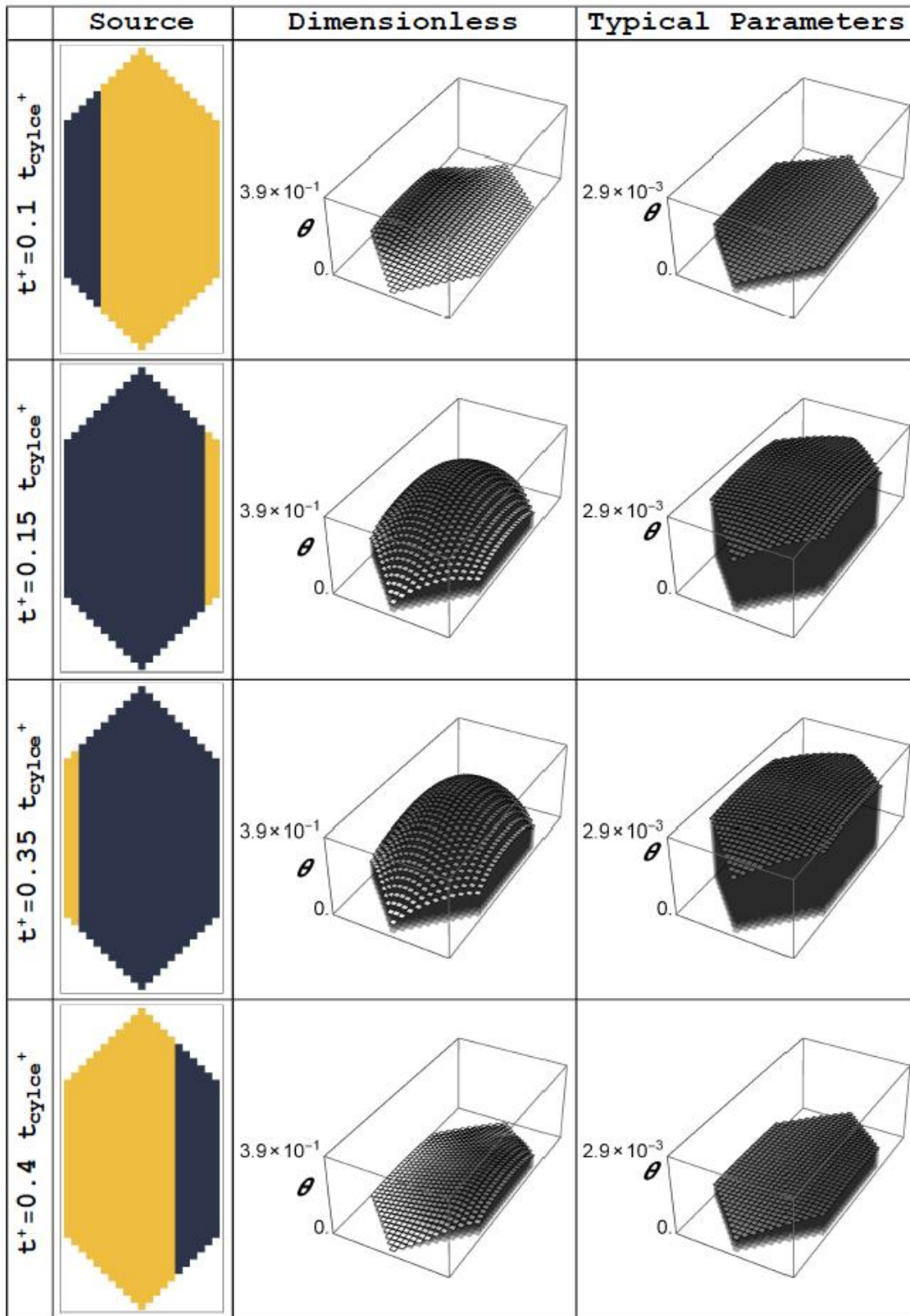
Figure 5.11. Temperature rise distribution at various times during the first half of a typical earth scan sequence.

Figure 5.12 shows the transient voltage for both the dimensionless and typical parameter cases. When normalized with the respective maximum voltage rise, the two curves fall on top of each other and appear as one line.
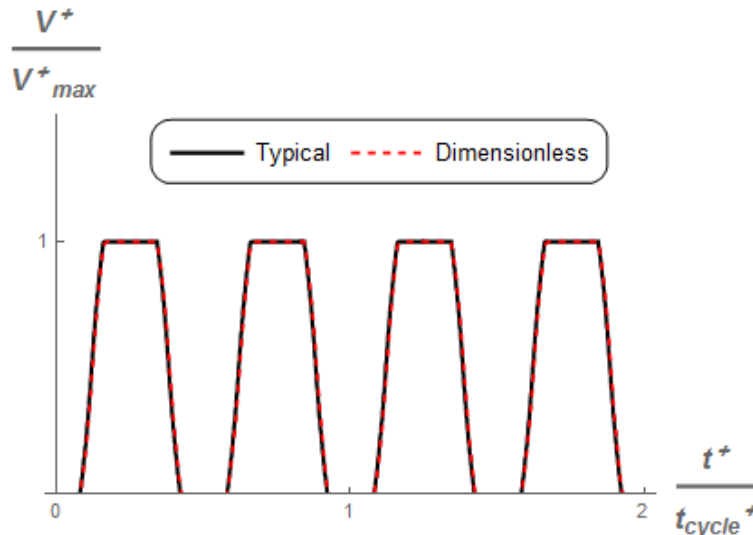
Figure 5.12. Voltage output for a typical earth scan sequence using typical and dimensionless parameters.

6 <u>Parameter Estimation</u>

The usefulness of the mathematical model is directly dependent on how well the theoretical model fits the experimental data. In general, for a given experimental test condition, the detector will produce a voltage time series. Therefore, applying these same test conditions to the MATLAB model should produce a time series that is as close as possible to the experimentally determined result. JPL conducted an experiment where a laser of known power was incident on the detector at specific (x, y) locations and the resulting voltage time series was recorded [32].

6.1 Experimental Data

A brief description of the experimental testing is presented here. A laser focused to a 75 µm full width at half maximum (FWHM) spot is incident on the detector mounted in a vacuum chamber. For a given (x, y) location, the data acquisition system is turned on to record the output voltage produced by the detector sampled at 50 kHz. At an arbitrary time, the laser is turned on to illuminate that (x, y) location and remains on for 0.5 s. The data acquisition continues to record the data long after the laser is turned off. In post-processing, a technician clips the voltage time series data to a 0.615-s segment that completely captures the rise and fall of the voltage signal corresponding to the time when the laser was pulsed over that location. The laser is moved to the next (x, y) location and the experiment is repeated. For each hexagonal detector, this experiment is conducted over a 2×3-mm mesh where the laser position is stepped in 37.5-µm increments. As a result, for a single detector, JPL provided 4374 voltage-versus-time data sets. A typical voltage response for a laser position near the center of the hexagonal sensor can be found in Figure 6.1.
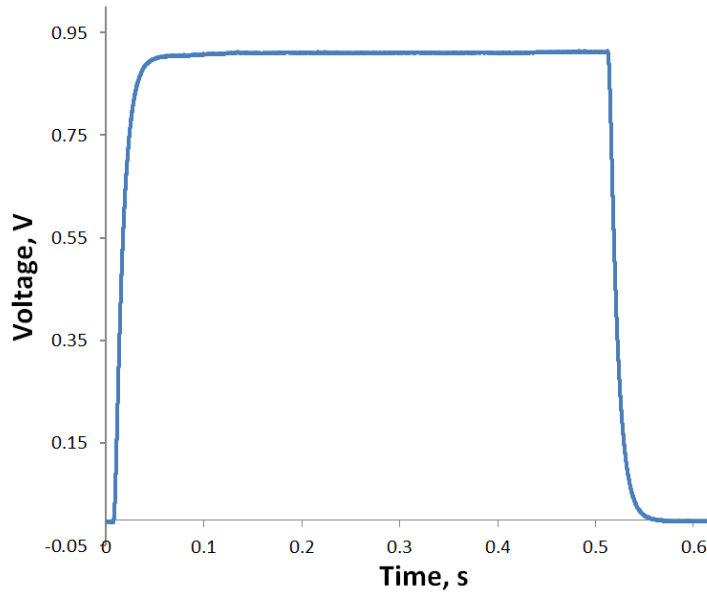
Figure 6.1. Voltage response for a laser position near the center of the hexagonal detector.

To replicate this experiment in MATLAB, the laser was modelled as a variation of the "extreme illumination" type heat source discussed in Section 5.5 of this thesis. As discussed in Section 5.5, the position of the source location does make a noticeable difference on the transient portion of the output voltage. While the details of the heat source were well documented in the provided technical report, a reference coordinate system was not provided. A reasonable coordinate system was developed in order to locate the 4374 positions within the 2×3 mm testing area. The 2×3-mm map was positioned so that the detector was perfectly centered in this mesh. Defining the lower left corner of the map to be the origin (0,0), the center of the detector was placed at (1, 1.5) mm. Figure 6.2 shows this in detail.
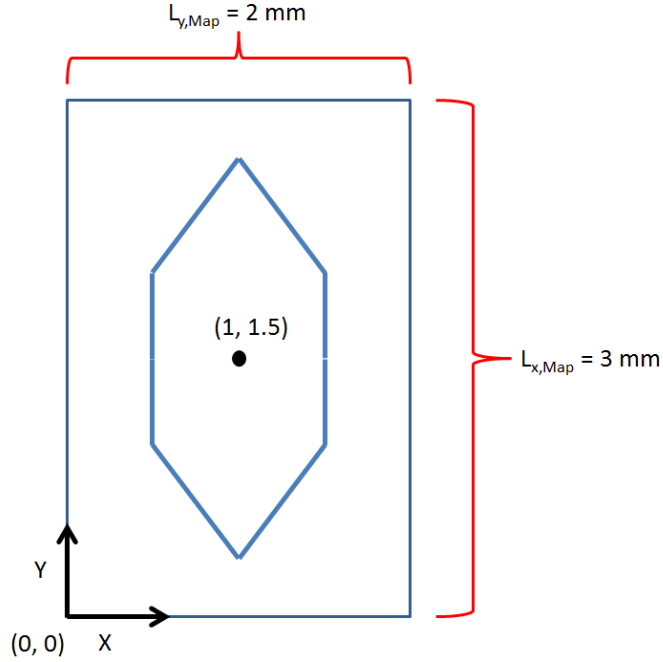
Figure 6.2. Proposed JPL map where scanning map is centered over the detector

The next step was to divide the 2-by-3-mm mesh into control volumes. Due to the nature of the finite volume method, the most concentrated heat source allowable would be one where all of the energy is absorbed in a single cell. Therefore, the surface area of a single cell should be equivalent to the size of the area illuminated by a 75-µm FWHM spot ($\sim4.42 \cdot 10^{-9}$ m^2). With a 30-by-15 (ii×jj) mesh for the detector the mesh spacing was determined as

$$\Delta x_{Det} = \frac{L_{x,Det}}{ii_{Det}} = 75.63 \ \mu m \tag{6.1}$$

$$\Delta y_{Det} = \frac{L_{y,Det}}{jj_{Det}} = 75.63 \ \mu m \tag{6.2}$$

By choosing this mesh, the surface area of each cell is $\sim5.72 \cdot 10^{-9}$ m^2. Using the 30-by-15 grid configuration is the closest mesh for representing the illuminated surface area as a single cell (i.e. extreme illumination). An alternative would have been to use a finer mesh and allow the heat source to illuminate multiple cells. However, using a finer grid would have increased the computational time required to evaluate the solution while not providing a significant return on accuracy, as discussed in Section 5.3. While the area illuminated is slightly different, the total power input to the system remains the same (1.52 mW). Using this spacing, the number of control volumes needed to recreate the entire JPL scan map is determined as

$$\text{ii}_{\text{Map}} = \frac{L_{y,Map}}{\Delta x_{Det}} = 39.67 \tag{6.3}$$

$$\text{jj}_{\text{Map}} = \frac{L_{x,Map}}{\Delta y_{Det}} = 26.44 \tag{6.4}$$

Normally, the grid would be truncated to a 39-by-26 size. However, for this particular case, it is convenient to round up rather than down creating a 40-by-27 grid. This is because, in the proposed mesh, the sensor is physically occupying the inner 30-by-15 cells. Having 40 cells in the x-direction places a symmetric five cells above the detector and five cells below, which is preferable to having an asymmetric distribution. Similarly, having 27 cells in the y-direction allows the ability to place a symmetric six cells to the left of the sensor area and six cells to the right. Figure 6.3 shows the described grid in detail.
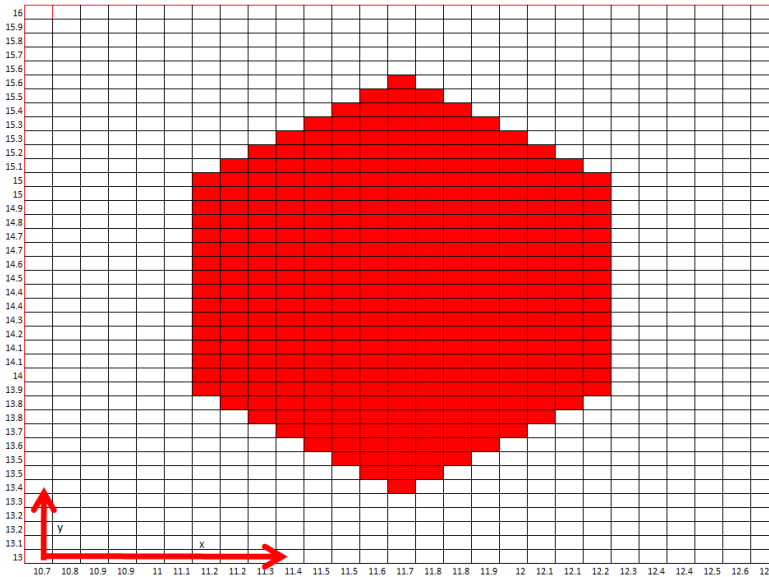
Figure 6.3. Mesh with (x, y) positions at each mesh line with respect to the testing origin.

Upon receiving the complete data set from JPL, it became clear that the origin shown in Figure 6.2 is not the same as the origin used for testing, shown in Figure 6.3. Each of the 4374 tested locations was referenced from a position located outside the domain of the detector. To convert the position of the local origin into the global coordinate system, the data files were searched to determine the minimum and maximum (x, y) positions tested. The minimum and maximum coordinates tested were (10.7, 13.0) and (12.7, 16.0). Placing the origin at the minimum coordinate (10.7, 13.0), the mesh now corresponds to the data provided. For convenience a mesh grid is shown in Figure 6.3 that shows the x-coordinate of the vertical lines along the bottom

58

(corresponding to the starting location of each finite volume) and the y-coordinates of the horizontal lines along the left (corresponding to the bottom of the finite volumes) with respect to the global coordinate system.

It is worth noting that because the laser is modelled as an extreme illumination type heat source, each location in Figure 6.3 will produce a unique voltage-versus-time response. However, only 1080 cells are contained in the finite volume mesh. Because the distance between the centers of two adjacent cells is 75.6 µm and JPL stepped the laser in 37.5 µm increments, about four voltage-versus-time responses fall within the domain of each cell. Of these four, the response whose laser coordinate is closest to the center of the cell is selected as the single unique voltage for this cell.

In order to compare the experimental results to the theoretical results, the power incident to the detector must be the same. When the laser is nearing edges of the detector, it is possible that not all of power incident on the detector is actually absorbed in the detector itself, but rather some is absorbed in the surrounding substrate upon which detector is mounted on. For instance, assume the laser is positioned such that it straddles the left edge of the detector. Due to the way the laser is modeled, the model would assume that all the power is absorbed in the left most cell of the detector. However, realistically, approximately 50 percent of the power would actually get absorbed by the detector and the remaining 50 percent would be absorbed by the substrate surrounding the detector. It would be tedious to accurately quantify the amount of power actually absorbed by the detector for these boundary locations. To avoid this, only the voltages produced at cells that are well within the interior of the detector are used for comparison. In Figure 6.4, the cells containing a number have been identified as interior to the detector. For ease of discussion, each cell has been given a location index labelled (1 − 130). While more locations could be included, 130 is sufficient to provide a statistically significant conclusion. Note: Figure 6.4 only shows the inner 30-by-15 cells from Figure 6.3 that comprise the detector.
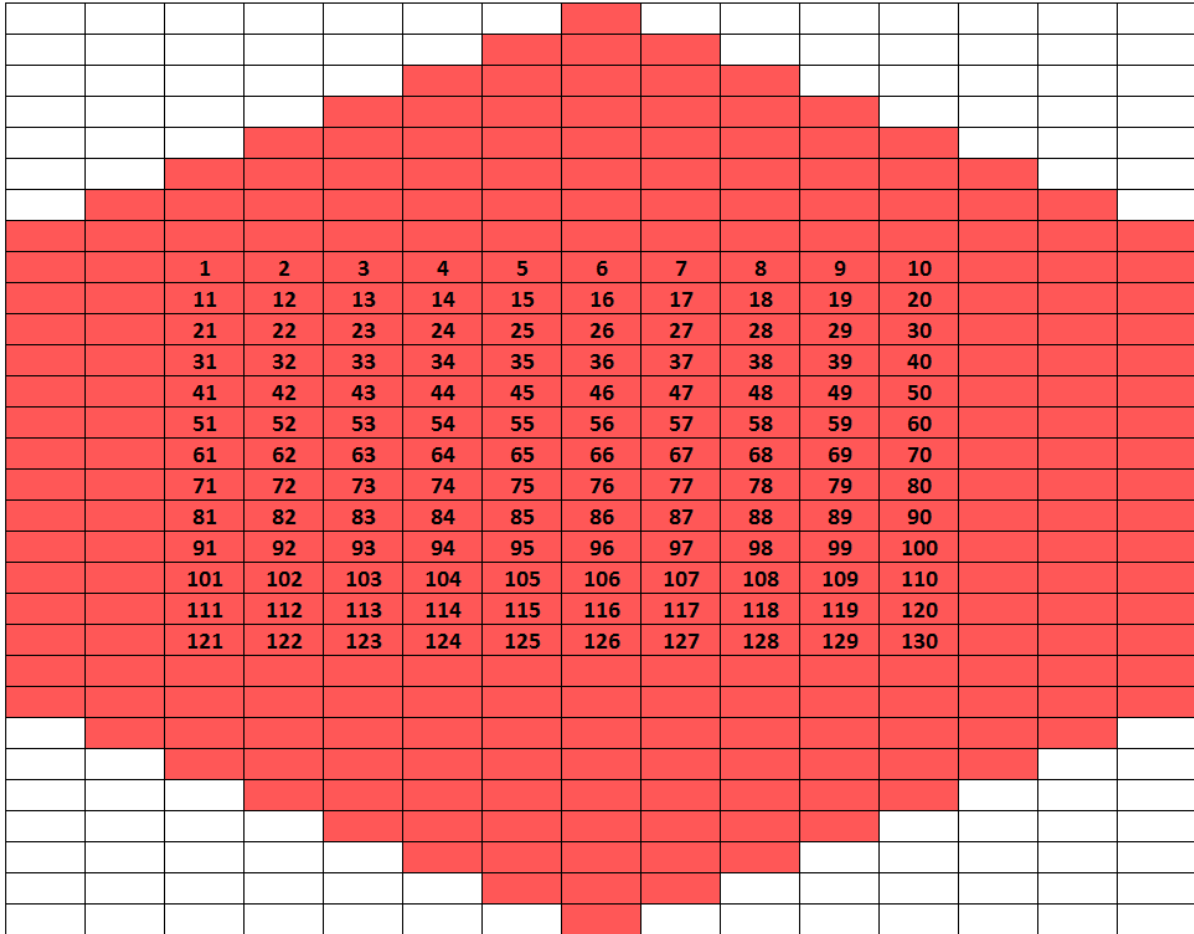
Figure 6.4. Indices of cells designated as interior to the detector for use in model comparison.

A time constant map was provided along with the complete voltage time series at all the locations [33]. The map, seen in Figure 6.5, was created by determining the time constant for standard first-order response at each location. The center of the detector has the largest time constant (8.6 ms), while moving outward towards the edges of the detector produces a gradually smaller time constant. This is to be expected since a voltage rise occurs when the temperature at the edge of the detector is greater than the surroundings. When the detector is heated at the center, the conduction path to the boundary is longer than if it is heated near the edge.

60
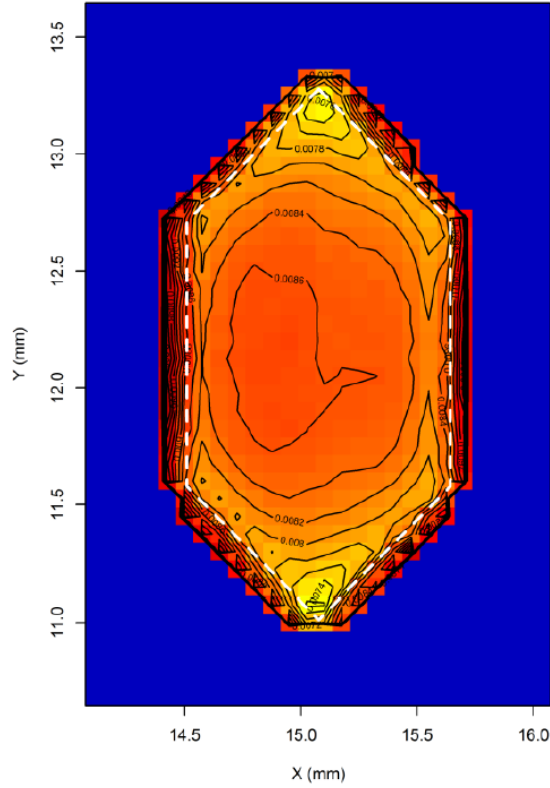
Figure 6.5. Time constant map created using JPL voltage time series [33].

In order to begin replicating the JPL data, the model inputs need to be finalized. To produce a voltage time series, the model needs the following inputs: thermal properties (ρc, k_{ther}, ϵ), heat source information ($I(x, y, t)$), boundary loss (h_{cont}, T_{sur}), and thermopile properties ($N_{thermocouples}, \alpha_{Seebeck}$). Of these inputs, only the values of ρc, k_{ther}, and h_{cont} had not been provided. As a result, a logical method of determining these parameters was investigated.

6.2   Equivalent Property Analysis

As discussed in Section 3.1, the detector is made up of three layers of different materials. Because the model includes only two-dimensional conduction, it is logical to hypothesize that the overall thermal properties of the detector can be determined using an appropriate equivalent properties analysis. Heat capacity, defined as the product ρc, is a volumetric quantity. An equivalent value is thus a volume-weighted average given as

$$\left(\rho c_{eq}\right)\mathcal{V}_{Total} = \rho c_{GB}\mathcal{V}_{GB} + \rho c_{GS}\mathcal{V}_{GS} + \rho c_{GA}\mathcal{V}_{GA}, \tag{6.5}$$

where,

61

$$\mathcal{V}_{GB} = L_x L_y L_{GB,}$$

$$\mathcal{V}_{GS} = L_x L_y L_{GS},$$

and

$$\mathcal{V}_{GA} = L_x L_y L_{GA.}$$

Therefore,

$$\rho c_{eq} = \frac{\rho c_{GB} L_{GB} + \rho c_{GS} L_{GS} + \rho c_{GA} L_{GA}}{L_{GB} + L_{GS} + L_{GA}}.$$

Thermal conductivity combines with area to produce thermal conductance. An equivalent area-weighted conductivity is

$$\frac{k_{ther,eq} A_{Total}}{L} = \frac{k_{ther,GB} A_{GB}}{L} + \frac{k_{ther,GS} A_{GS}}{L} + \frac{k_{ther,GA} A_{GA}}{L}, \qquad \textbf{(6.6)}$$

where

$$A_{GB} = L \cdot L_{GB},$$

$$A_{GS} = L \cdot L_{GS,}$$

$$A_{GA} = L \cdot L_{GA,}$$

and

$$A_{Total} = L(L_{GB} + L_{GS} + L_{GA}).$$

Therefore,

$$k_{ther,eq} = \frac{k_{ther,GB} L_{GB} + k_{ther,GS} L_{GS} + k_{ther,GA} L_{GA}}{L_{GB} + L_{GS} + L_{GA}}.$$

Developed above, the equivalent thermal properties of the lumped system were determined using the equations and the thermal properties of each individual layer. These equivalent properties can be found in Table 6.1.

Table 6.1. Equivalent thermal properties analysis

Layers From Figure 3.1	$\rho, \frac{kg}{m^3}$	$c, \frac{J}{kg \cdot K}$	$k_{ther}, \frac{W}{m \cdot K}$	L, μm
Gold-Black (Estimated)	96.5	124.5	$3 \cdot 10^{-3}$	30
Gold-Absorber (Gold Impregnated Silicon-Nitride)	19300	129	170	0.25
Gold-Shunt	19300	129	100	0.018
Equivalent	266.5	127.3	1.467	30.268

While the thermal properties can be estimated using the equivalent property analysis discussed above, the contact conductance, h_{cont}, need to be determined in a different manor. The magnitude of the heat loss due to the thermopiles is known to be a critical value to the accuracy of the model. However, while this quantity is recognized to be important, a good estimate of its value was difficult to obtain. Using the time constant map supplied by JPL [33], allowed a simplified parameter estimation of this value. The methodology behind this parameter estimate is presented here. To simplify the model, a lumped-capacity version of the full model for the hexagonal sensor is used, yielding

$$\rho c \mathcal{V} \frac{dT}{dt} = h_{cont} A_{cont} (T - T_{sur}) + I_c A_{rad}, \tag{6.7}$$

where ρ and c are the equivalent properties listed in Table 6.1, $\mathcal{V}$ is the total volume of the sensor, h_{cont} is the heat transfer coefficient representing the loss due to the thermopiles, A_{cont} is the surface area along the boundary of the sensor, I_{rad} is the magnitude of the radiation incident on the detector, and A_{rad} is the area upon which the radiation is incident. The initial condition for this system is

$$T = T_{sur}, t = 0. \tag{6.8}$$

Rearranging Equation 6.7 produces an equation in terms of the time constant τ,

$$\frac{dT}{dt} = \frac{1}{\tau}(T - T_{sur}) + \frac{I_c A_{rad}}{\rho c \mathcal{V}}, \qquad\qquad (6.9)$$

where

$$\tau = \frac{\rho c \mathcal{V}}{h_{cont} A_{cont}}. \qquad\qquad (6.10)$$

In Equation 6.10, $\mathcal{V}$, and A_{cont} are known from the dimensions of the gold-black sensor. Similarly, the values of ρ and c had been found using the equivalent properties analysis. In order to get a good approximation of h_{cont}, a value for τ must first be found. It is important to note that the value being estimated is really the product of $h_{cont} A_{cont}$. The model assumes that the A_{cont} is the total boundary of the detector (i.e. Perimeter·L_z). In reality, the thermocouples do not cover the entire boundary area of the detector. Further investigation of the data in Figure 6.5 reveals that the detector has an average time constant of 8.5 ms. Using the values in Table 6.2 along with this average time constant, a value of h_{cont} is estimated to be $1407.2 \frac{W}{m^2 \cdot K}$.

Table 6.2. Properties used to estimate required value of h$_{cont.}$

Parameter	Value
L_x, mm	2.269
L_y, mm	1.1345
L_z, μm	30.268
$\rho, \frac{kg}{m^3}$	266.5
$c, \frac{J}{kg \cdot K}$	127.3
$\mathcal{V}, m^3$	$5.84 \cdot 10^{-11}$
A_{cont}, m^2	$1.66 \cdot 10^{-7}$

When discretized, the surface area along the outside of the sensor is slightly larger ($1.68 \cdot 10^{-7}$ m^2) than the true value ($1.66 \cdot 10^{-7}$ m^2). This difference must be taken into consideration. In order to maintain the same magnitude for $h_{cont} A_{cont}$, the final value of h_{cont} was adjusted to be $1391.3 \frac{W}{m^2 \cdot K}$.

$$\left(1407.2\,\frac{W}{m^2 K}\right)\left(\frac{1.66 \times 10^{-7}\, m^2}{1.68 \times 10^{-7}\, m^2}\right) = 1391.3\,\frac{W}{m^2 K} \qquad \textbf{(6.11)}$$

After the input parameters have been determined, it is then possible to use the model to attempt to reproduce the data provided by JPL. For an initial comparison, it was decided to compare the experimental voltage produced at a location near the center of the detector to the voltage predicted using the model at the same location. Location index 68, which can be located by referring to Figure 6.4, was chosen for this comparison. Figure 6.6 is a comparison between the predicted voltage time response using the equivalent properties analysis and experimental data from JPL when the heat source illuminates this spot. The voltage produced by the model using these input parameters exceeds the measured voltage by a factor of 1.5. We concluded that a more accurate parameter estimation scheme is needed to determine the appropriate parameters that capable of replicating the experimental data.
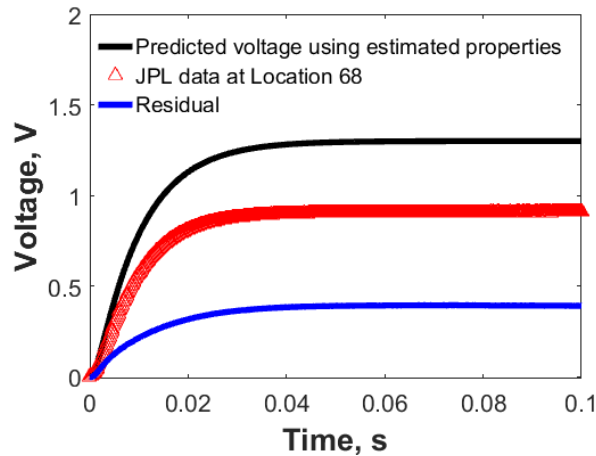
Figure 6.6. Comparison of voltage response using estimated parameters analysis and JPL data.

6.3 Sensitivity Analysis

It has been shown that the equivalent property analysis method is not an adequate method for determining the parameters. A sensitivity study was performed to determine which parameters are most important to replicating the JPL data. For each parameter, a goal of this study is to determine how the voltage output responds to a small change in the nominal value of that parameter. If a small change in the nominal value of the parameter produces a large change in output voltage, it becomes clear that emphasis should be placed on the value of this parameter.

65

Conversely, if a small change in the nominal parameter value has little or no effect on the output, we give lower priority to obtaining the accuracy of this value.

In order to investigate the influence of model parameters, we introduce the concept of sensitivity, defined

$$X_p(t) = \frac{\partial V}{\frac{\partial p}{p_{nom}}},$$

(6.12)

where p is one of the system parameters and the subscript "nom" refers to the nominal, or best estimate of, a particular parameter. Equation (6.11) is an example of this concept. The idea is to see how the output changes for a fractional change in a model parameter.

Since we have developed a discretized solution using a finite volume method, the derivative in Equation (6.11) must be evaluated numerically using finite differences. That is, the results from two numerical solutions corresponding to two slightly different values of parameter p must be computed and subtracted to approximate the sensitivity as

$$X_p(t) \cong \frac{V(t) - V_{nom}(t)}{(p - p_{nom})/p_{nom}}$$

(6.13)

For this sensitivity study, the nominal values, unless otherwise specified, are those found in Table 6.3. The detector is radiated by a heat source identical to that described in Section 6.1—an extreme illumination source concentrated in the center of the detector, at location index 66. However, in this case, the heat source is turned on immediately and remains on for 0.05 s. In addition to investigating the sensitivity study around the nominal values, the team decided to investigate the difference in the results obtained when if the nominal values of k_{ther} and h_{cont} are significantly different.

Table 6.3. Nominal parameters for sensitivity analysis.

Symbol	Units	Nominal Value
h_{cont}	$\dfrac{W}{m^2 \cdot K}$	1400
I_c	$\dfrac{W}{m^2}$	$2.67 \cdot 10^5$
k_{ther}	$\dfrac{W}{m \cdot K}$	3
L_x	mm	2.269
α_s	$\dfrac{\mu V}{K}$	132
ε	–	0.95
ρc	$\dfrac{J}{m^3 \cdot K}$	16000

The sensitivity analysis results corresponding to the four nominal values of k_{ther} are shown in Figure 6.7. This sequence emphasizes the sensitivity of the results to the thermal conductivity. As shown Figure 6.7(a), for a high value of thermal conductivity corresponding to a pure gold detector, the sensitivity of k_{ther} relative to the other parameters is essentially zero. As we proceed to lower k_{ther} values in Figure 6.7, we see an increasing sensitivity. The sensitivities to k_{ther} are collected in Figure 6.8. The conclusion is that for a pure gold detector using 317 or 318 (or 3000) $\frac{W}{m \cdot K}$ for k_{ther} would make little difference. However, using a value of around 2 or 3 $\frac{W}{m^2 K}$, as determined with the equivalent property analysis, can make a very significant difference. In addition to an increase in sensitivity to k_{ther} at lower values of k_{ther}, an increase in the sensitivity to radiation exchange parameters, T_{sur} and ϵ is also noticeable. Additionally, an overall increase in the time it takes to reach steady state is observed. This is best demonstrated in Figure 6.7(d) where $X_{T_{sur}}$ is the largest at its peak. Radiation parameters become very important because with such low conductivity the heat absorbed in a concentrated area cannot be conducted out efficiently. This causes a large temperature rise in that concentrated area, thereby increasing the radiation exchange.
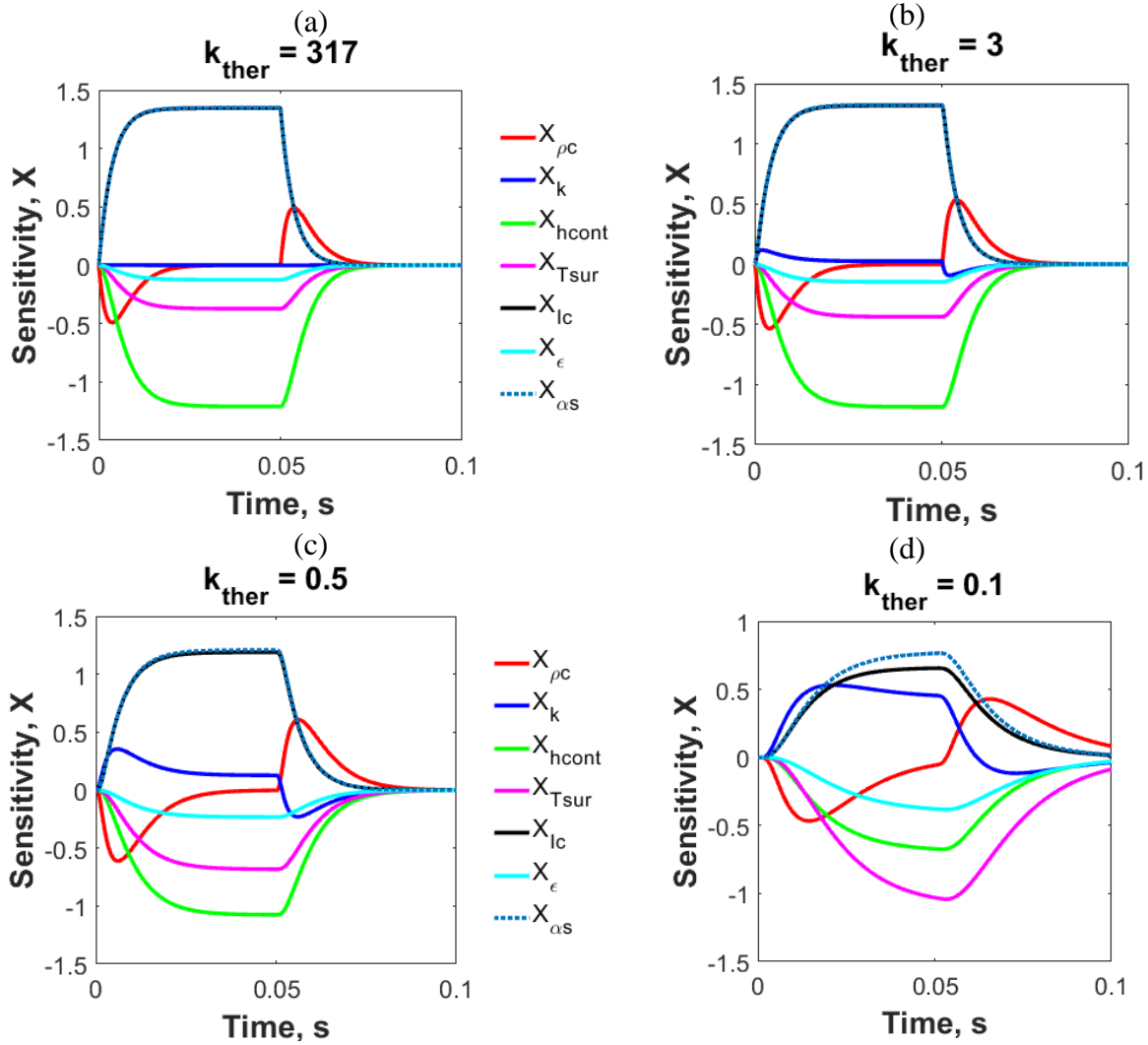
Figure 6.7. Sensitivity to model parameters at decreasing values of k$_{ther}$ where (a) k$_{ther}$ = 317, (b) k$_{ther}$ = 3, (c) k$_{ther}$ = 0.5, (d) k$_{ther}$ = 0.1.
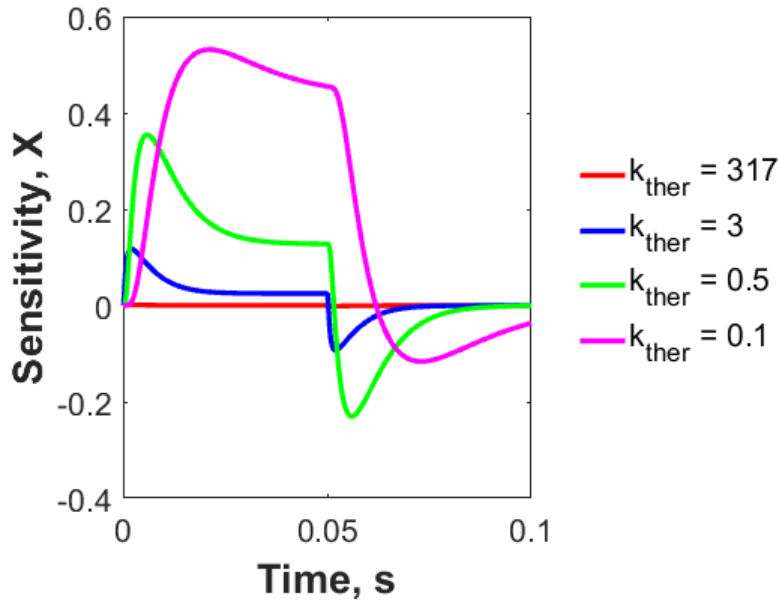
Figure 6.8. Sensitivity to k$_{ther}$ at decreasing nominal values.

The sensitivity to h_{cont} works in a much different way. As discussed in Section 5.4, a large value of h_{cont} keeps the boundary temperature from having any significant rise over the surrounding temperature, producing no voltage. As the magnitude of h_{cont} increases to infinity, the sensitivity to all of the parameters decreases, as seen in Figure 6.9. Similarly, a small value of h_{cont} removes no heat from the system, and radiation exchange is the only cooling mechanism. At these two extremes, little to no sensitivity to h_{cont}, is observed, as seen in Figure 6.9. However, a band of values exists between the two extremes, where h_{cont} is significant. In Figure 6.10, we can see that $h_{cont} = 500$ is approximately the peak nominal value where the sensitivity is highest.
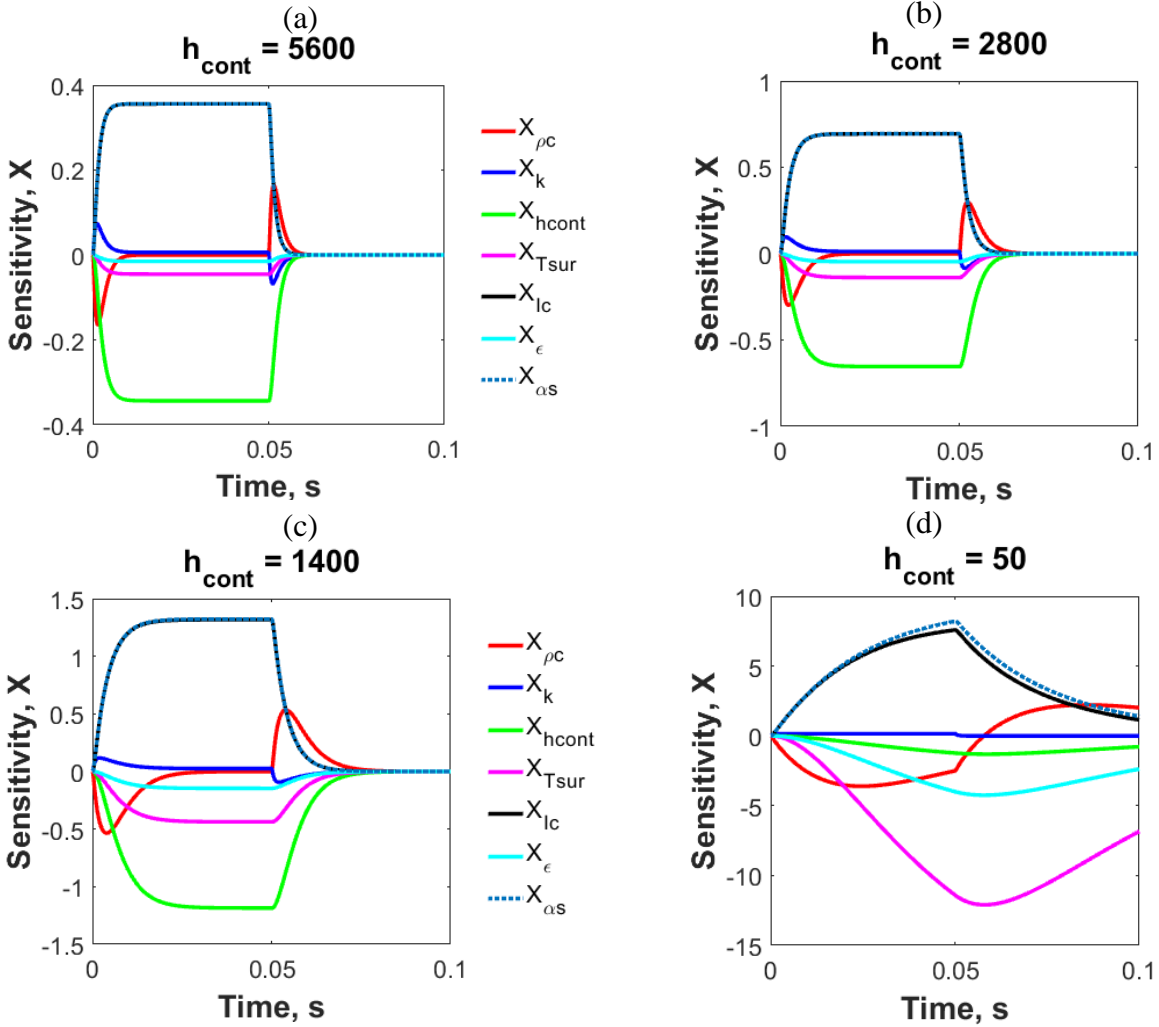
Figure 6.9. Sensitivity to model parameters at decreasing values of h_{cont} where (a) h_{cont} = 5600, (b) h_{cont} = 2800, (c) h_{cont} = 1400, (d) h_{cont} = 50.
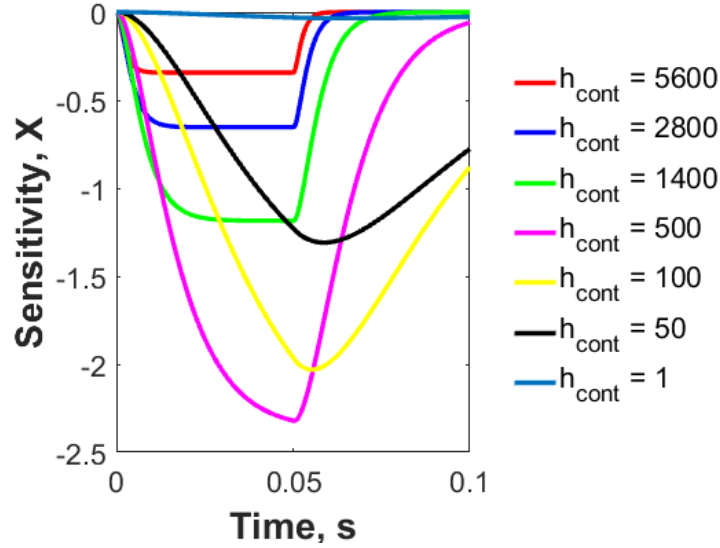
Figure 6.10. Sensitivity to h$_{cont}$ at decreasing nominal values.

Ultimately, the findings from the sensitivity study confirm the expected. Using the nominal values, it is clear that the magnitude of the heat source is the most important parameter to estimate accurately. Using the MCRT method, we are confident in the accuracy of this parameter. The values of h_{cont} and k_{ther} greatly affect the output voltage. In order to replicate data produced by the real detector, the magnitude of these two parameters must be accurately known.

6.4 The Parameter Estimation Method

An overview of a typical parameter estimation procedure is depicted in Figure 6.11 [34]. The objective is to estimate the values of the unknown parameters $\bar{\beta} = [\beta_1, \cdots, \beta_n, \cdots, \beta_N]$ such that a best fit is found between theory, $\hat{V}_m(\beta) = V(x_s, t_m, \beta)$, and experimental data, $\bar{V} = [V_1, V_2 \cdots, V_m, \cdots, V_M]$. The determination of the unknown parameters is based on minimization of the ordinary least square norm given by

$$S(\beta) = \sum_{m=1}^{M} \left(V_m - \hat{V}_m(\beta) \right)^2. \tag{6.14}$$

The quantity S is referred to as the objective function. Here V_m is the experimental voltage data at time step-m and $\hat{V}_m(\boldsymbol{\beta})$ is the predicted voltage at that same time as a function of the model parameters, $\boldsymbol{\beta}$. The desired minimum value of $S(\beta)$ is where $\frac{\partial S}{\partial \beta} = 0$. Note: Voltage data were

71

provided by JPL, so a voltage time series is used for comparison. If JPL had provided a detailed temperature map across the detector, this method could have been extended to treat a temperature comparison.
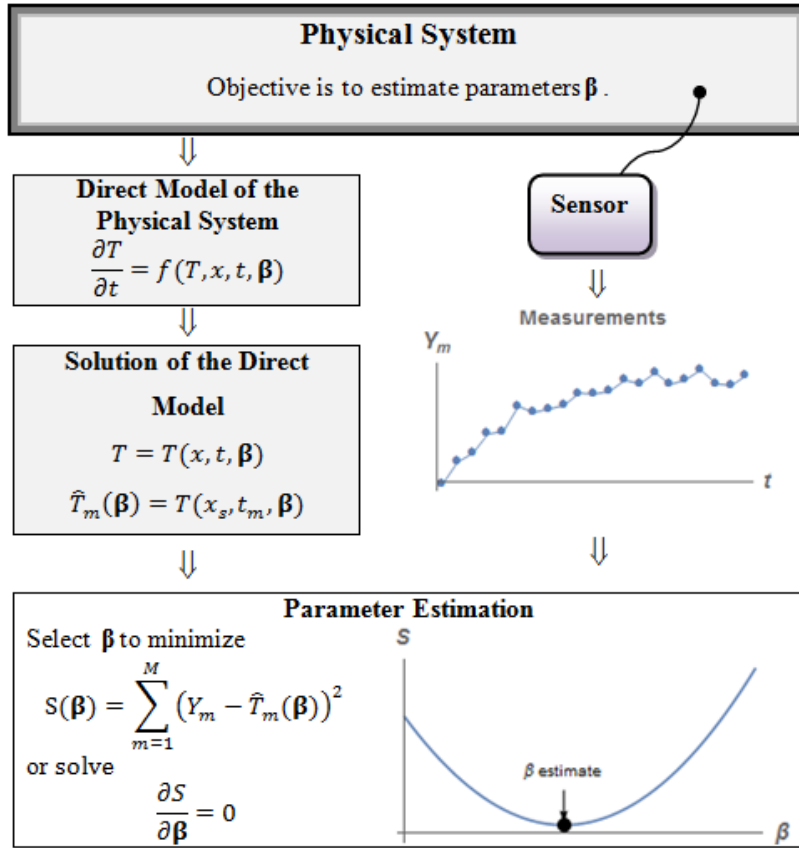
Figure 6.11. Typical parameter estimation schematic diagram.

A parameter estimation scheme was developed to tune the model parameters—ρc, k_{ther}, and h_{cont}—to replicate experimental data from JPL. The typical data shown in Figure 6.1 indicate a delay time between the beginning of the measurements and the activation of the laser. Additionally, a random DC offset, V_{DC}, is introduced into the system from the measurement equipment used at JPL. Neither of these parameters is a model parameter, but rather both are purely experimental. This delay time and DC offset, t_{start} and V_{DC}, must also be estimated in order to determine the model parameters. However, these parameters are purely experimental; the final model does not include these parameters.

As a way to reduce the number of parameters to be estimated in the parameter estimation algorithm, V_{DC} was determined by averaging the first 300 data points at the beginning of the JPL data at a single location. This portion of the data clearly represents a time interval before the heat source was energized, and consists of random background noise, as indicated by its small (and often negative) voltage values. While each data file provided by JPL had a slightly different V_{DC}, it was accounted for by shifting each voltage by its offset before the parameter estimation scheme was performed.

A general overview of the MATLAB parameter estimation algorithm developed in this thesis is presented here. The JPL data were imported and positioned at their respective mesh locations as discussed in Section 6.1. The DC offset was computed and accounted for at every location. Next, each data set was searched to find 99 percent of its respective maximum voltage and the time required to reach this voltage. As seen in Figure 6.1, a recorded voltage of about 80 percent corresponds to steady state. To avoid overly weighting the steady state and missing the early transients, the model voltage and corresponding sum-of-the-squares value were evaluated only at the time corresponding to 99 percent of the maximum. Using the data in Figure 6.1 as an example, 99 percent of the maximum occurs around 0.1 s; therefore, the model only determines the solution for the first 0.1 s. By doing this, the overall CPU time was reduced because the solution does not need to be evaluated as far into the future; however, it means that at each location, a slightly different number of points are used for comparison. This is discussed later. For a given location index, the experimental data were recreated in MATLAB using an initial guess for each of the four parameters, and the corresponding sum-of-the-squares is computed. Using the "fminsearch" function in MATLAB, the parameters are systematically iterated until the four parameters that produce the smallest sum of the squares value is determined.

When a parameter estimation technique is performed against a unique set of experimental data, a single set of parameters is determined. This means that when looking at 130 data sets, 130 different sets of parameters are computed. Ultimately, a single set of parameters that best describes the whole detector is needed for the model. Two slight variations were considered to arrive at this single set.

1. Individual and averaged - Perform the parameter estimation at each of the 130 locations and average all the parameters sets to get one final set.

2. Simultaneous Estimation - Adjust the algorithm so that, using a single set of parameters, the voltage at 130 locations is computed. Then, the sum of the squares is performed at all 130 locations and all of the locations are summed to produce a single objective function. This total sum of the squares is then the value to be minimized.

Although this is a four-dimensional optimization problem, a simplified one-dimensional visualization of typical results is shown in Figure 6.12. Setting $\rho c, h_{cont},$ and t_{start} as constants, the objective function is used to determine the value of k_{ther} that best fits the data by minimizing the objective function. Examination of the figure indicates that the value of k_{ther} to minimize $S(\boldsymbol{\beta})$ is around $2 \frac{W}{m\,K}$. An efficient and accurate nonlinear minimization function available in MATLAB is used to numerically determine the optimal values. Figure 6.12 shows that $S(\boldsymbol{\beta})$ has a well-defined minimum with no local minimums, which should enable accurate numerical solutions. This becomes more complicated when four parameters are to be found to minimize $S(\boldsymbol{\beta})$, but the general methodology remains the same.
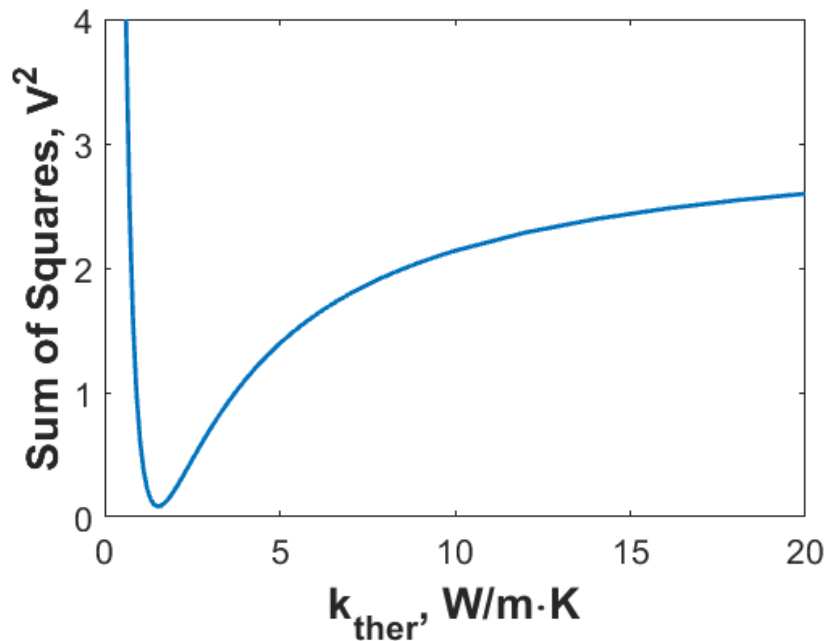
Figure 6.12. Typical landscape of the objective function with respect to k_{ther}.

74

6.5 Parameter Estimation Results

6.5.1 Individual and Averaged Results

Since the individual, average method produced 130 different parameter combinations, a statistical analysis was performed on the results to determine a single set of parameters that best fit the entire detector. Figure 6.13-Figure 6.17 show the cumulative results for $\rho c, k_{ther}, h_{cont},$ t_{start} and the objective function, respectively. Each of these figures contain the following results:

A. Estimates for all the 130 data sets
B. A map of the estimates with the outliers highlighted in yellow
C. A box-and-whisker summary of the distribution of values
D. Probability distribution function (PDF) of the computed results.

While each of the figures show the same information, a detailed discussion of the estimated ρc values, Figure 6.13, is presented. In Figure 6.13(a), the estimates are plotted versus location index. Thankfully, the parameter estimation scheme always estimates ρc to be on the order of $4 \cdot 10^4 \frac{kg}{m^3}$ with a reasonably small variation. Using the box-and-whisker plot in Figure 6.13(c), nine outliers (identified as points outside the "whisker") with three being too small and six being too large. Next, an investigation to ensure that no significant pattern exists to sensor location and outliers was performed. Figure 6.13(b) shows that the outlier locations seem to be randomly dispersed around the tested locations, but are more likely to occur around the perimeter. Regarding the PDF in Figure 6.13(d), the results for all the locations seem to follow a typical Gaussian-like distribution with a standard deviation indicated on the plot.
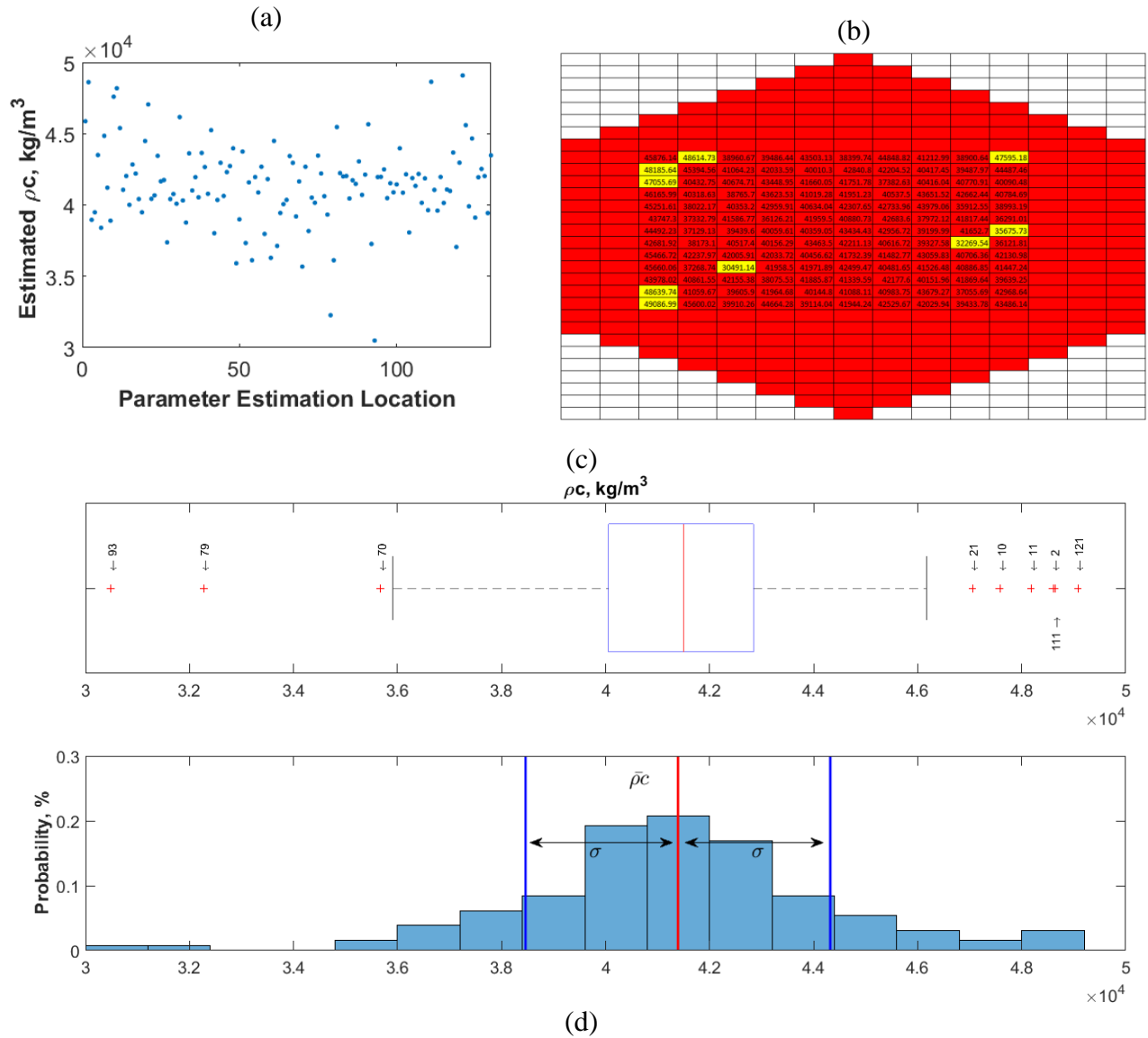
Figure 6.13. Parameter estimation results of ρc for 130 locations, (a) raw estimates at each location index, (b) estimates-versus-detector location with outliers identified (yellow), (c) box-and-whisker plot for identifying outliers, (d) probability distribution function.

Figure 6.14 displays the thermal conductivity estimates. In Figure 6.14(d), the PDF is skewed toward lower values rather than being symmetric as expecting in typical Gaussian distributions. Additionally, Figure 6.14(c) shows nine outliers, all of which are too large.
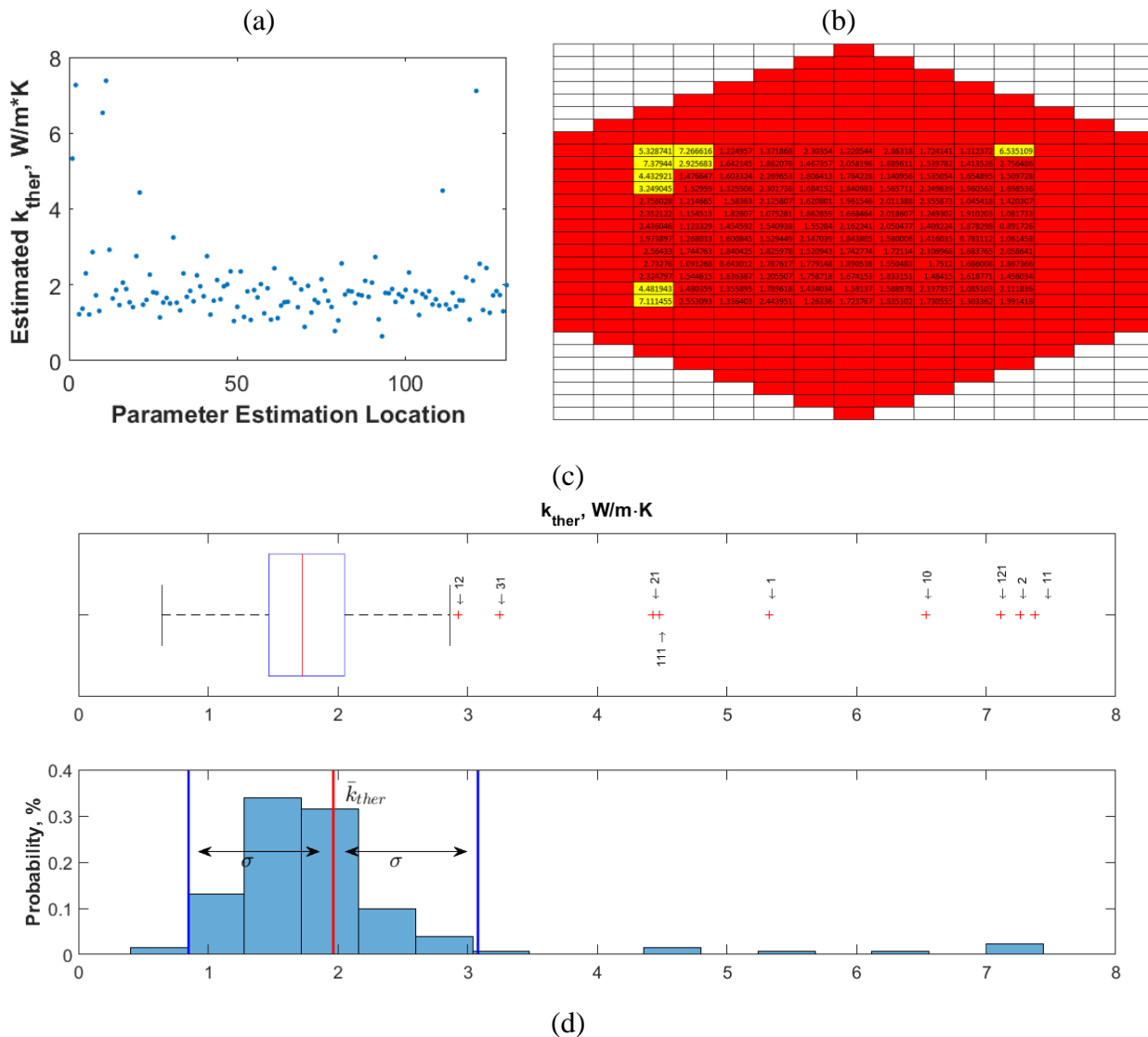
Figure 6.14. Parameter estimation results of k_ther for 130 locations, (a) raw estimates at each location index, (b) estimates-versus-detector location with outliers identified (yellow), (c) box-and-whisker plot for identifying outliers, (d) probability distribution function.

Figure 6.15 shows the summary of contact conductance estimates. In Figure 6.15(d), the results seem to be a rather symmetric, Gaussian–like distribution with a relatively low standard deviation. Figure 6.15(c) shows, there are only four outliers and they are not far beyond the whiskers. This parameter has been previously shown in the sensitivity figures to be an extremely important parameter. Fortunately, the contact conductance estimates were the most repeatable and seemed to always estimate values around $2060 \frac{W}{m^2 \cdot K}$.

(a)

(b)

2111.592	2107.053	2057.558	2062.217	2085.513	2046.177	2085.484	2060.999	2049.157	2094.295
2110.757	2093.292	2065.551	2075.986	2057.687	2071.707	2063.161	2050.044	2048.243	2078.458
2101.106	2063.602	2064.006	2080.831	2064.716	2062.032	2025.686	2046.852	2053.655	2051.903
2093.424	2062.694	2048.538	2075.589	2057.422	2060.734	2047.632	2066.937	2053.042	2053.59
2083.789	2044.944	2057.028	2073.214	2052.224	2059.825	2057.313	2064.792	2013.989	2041.46
2080.562	2038.685	2061.04	2020.216	2066.486	2051.087	2056.393	2021.052	2052.249	2038.704
2076.948	2033.951	2049.686	2059.704	2061.502	2076.082	2057.38	2028.045	2047.837	1996.258
2088.078	2041.876	2062.074	2067.223	2088.243	2073.406	2044.959	2027.384	1972.371	2012.267
2075.648	2064.522	2074.819	2082.099	2073.896	2072.304	2050.445	2051.877	2040.127	2050.132
2079.793	2037.074	1978.161	2082.474	2077.629	2072.458	2046.8	2040.43	2040.312	2046.216
2077.354	2060.525	2072.015	2051.074	2072.624	2058.075	2050.19	2029.8	2034.95	2033.744
2093.955	2062.086	2052.684	2069.086	2056.294	2052.983	2040.701	2055.088	2013.523	2053.524
2101.149	2023.776	2053.242	2081.637	2043.751	2054.969	2051.841	2045.245	2031.49	2051.214

(c)

h_{cont}, W/m^2·K

(d)

Figure 6.15. Parameter estimation results of h$^+_{cont}$ for 130 locations, (a) raw estimates at each location index, (b) estimates-versus-detector location with outliers identified (yellow), (c) box-and-whisker plot for identifying outliers, d) probability distribution function.

Figure 6.16 shows the start time estimates for the experiments. Although this is an experimental parameter and not a system parameter, t_{start} is crucial to the parameter estimation scheme. A small error in t_{start} can cause a large difference in the $\rho c, k_{ther}, and\ h_{cont}$ estimations. For instance, looking at Figure 6.1, it is likely that one would estimate $t_{start} \sim 8\ ms$. It would seem to be a good estimate and the remaining three parameters $\rho c, k_{ther}, and\ h_{cont}$ would be determined. However, if another person suggested using $t_{start} \sim 8.5\ ms$, a completely different set of $\rho c, k_{ther}, and\ h_{cont}$ would be determined. This can be problematic when the start time is not

78

accurately known. As described in Section 6.1, "…A technician clips the voltage time series data to a 0.615-s segment that completely captures the rise and fall of the voltage signal corresponding to the time when the laser was pulsed over that location." Therefore, for each data set, the 0.615 s was completely arbitrary and the start time could have been slightly different for each data set. Luckily, Figure 6.16(a) shows that the start times are clustered around 10 ms and only exhibits one outlier.
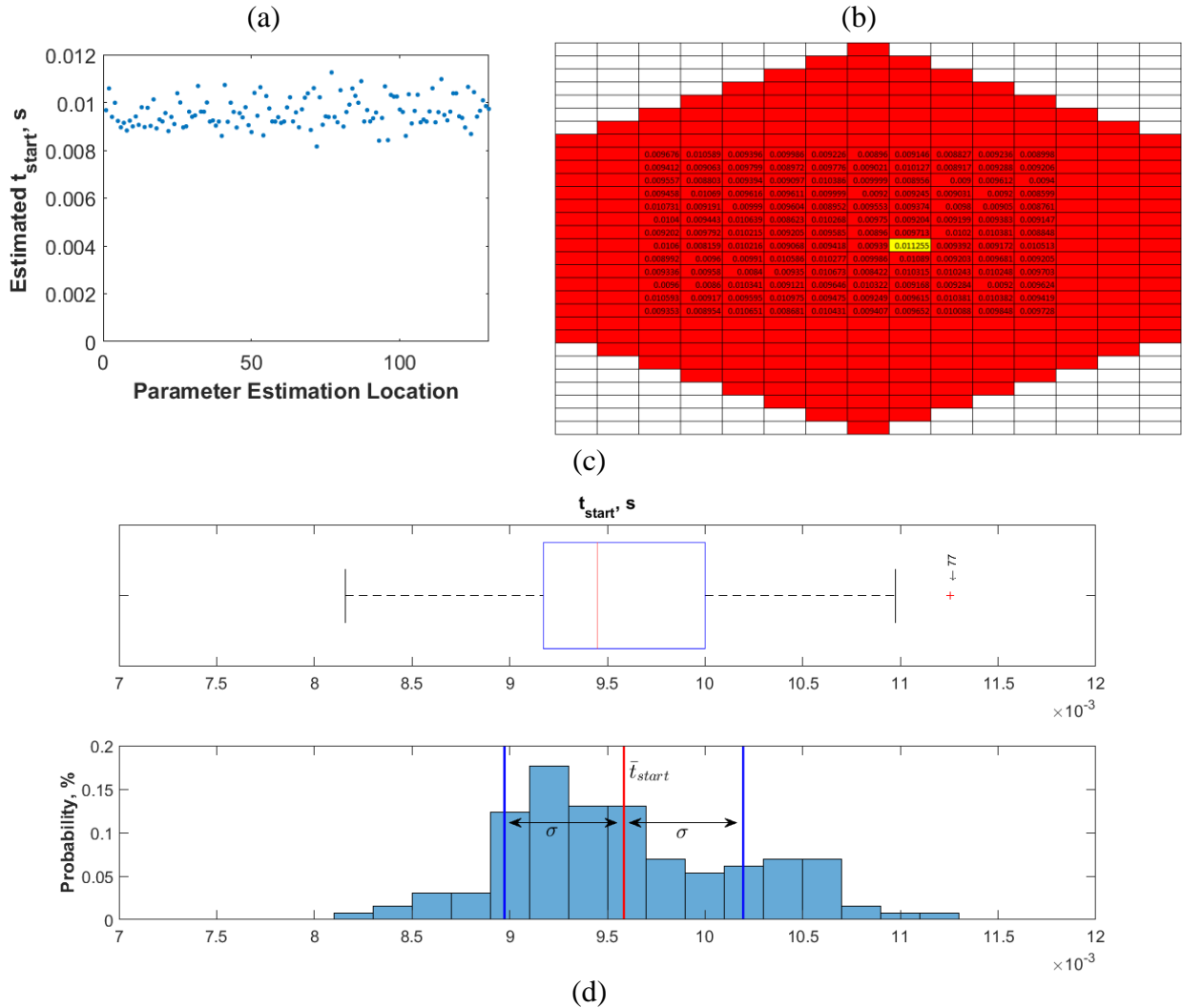

Figure 6.16. Parameter estimation results of t$_{start}$ for 130 locations, (a) raw estimates at each location index, (b) estimates-versus-detector location with outliers identified (yellow), (c) box-and-whisker plot for identifying outliers, (d) probability distribution function.

Lastly, the sum of the squares values were examined to ensure the absence of alarmingly bad fit results, as seen in Figure 6.17. Figure 6.17(c) shows there were four outliers that were all significantly higher than the others.
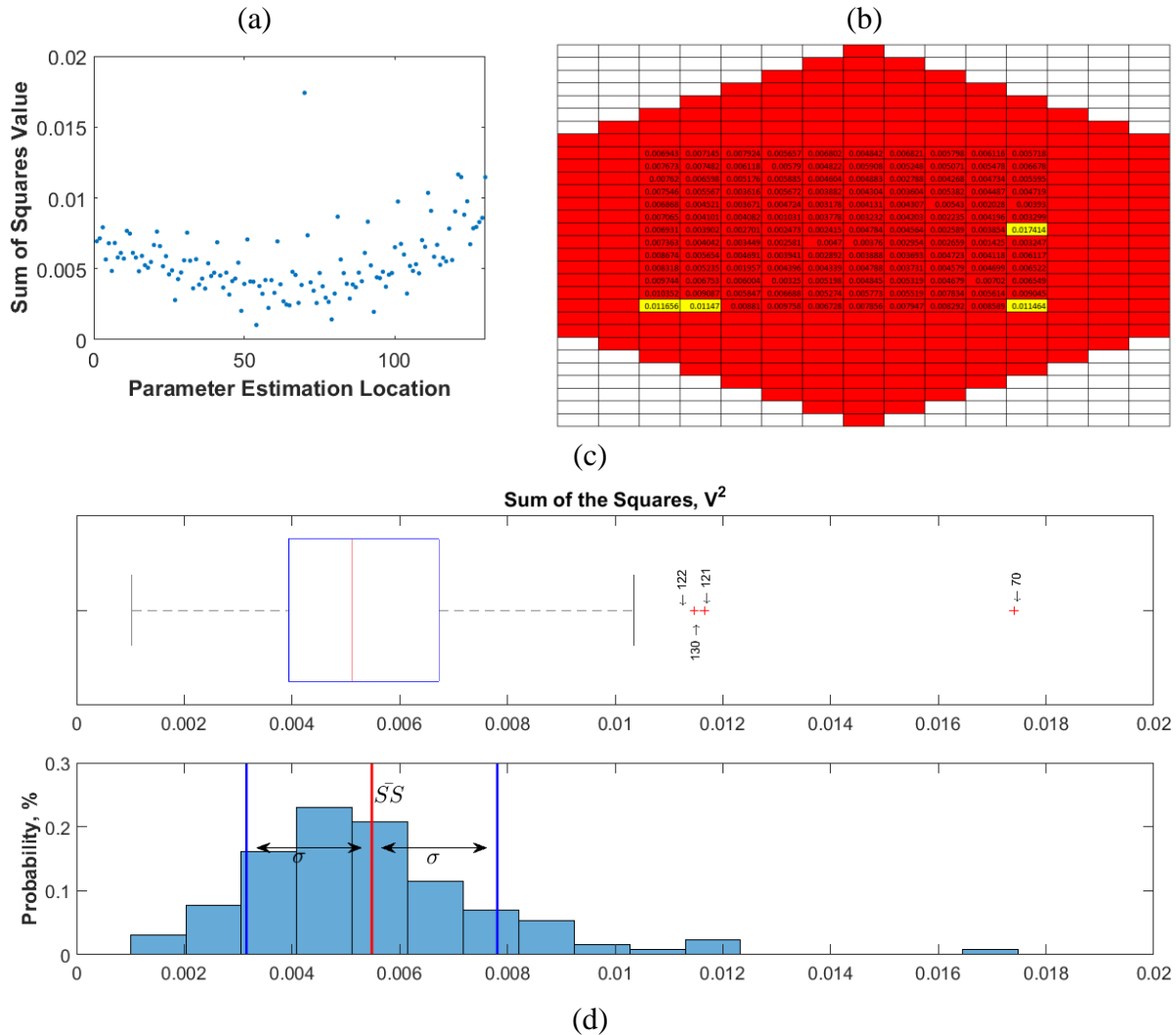
Figure 6.17. Parameter estimation results of sum of the squares for 130 locations, (a) raw estimates at each location index, (b) estimates-versus-detector location with outliers identified (yellow), (c) box-and-whisker plot for identifying outliers, (d) probability distribution function.

The statistical findings for all the results discussed in the above figures are summarized in Table 6.4. Focusing specifically on outliers, among the five data sets analyzed ($\rho c, k_{ther}, h_{cont}$, t_{start} and the objective function) are 15 unique locations having an outlier in at least one of the

five sets. Across the data sets, a common theme is that the upper-left and lower-left areas tested produced the most outliers. This is likely due to the assumption that the thickness L_z is a constant across the entire detector. Due to limits inherent to the manufacturability of the detectors, it is likely that some small thickness variation exists across the detector. This thickness variability could be much more significant in the areas that produced outliers. However, since there is no way to actually quantify this, the optimal solution is to report the averages excluding the outlier locations. Table 6.5 shows a comparison of the parameter estimation results, with and without the outliers included.

Table 6.4. Descriptive statistics for parameter estimation scheme.

	ρc $(\frac{J}{m^3 K})$	k_{ther} $(\frac{W}{m\,K})$	h_{cont} $(\frac{W}{m^2 K})$	t_{start} (s)	SS (V^2)
Mean	41390	1.96	2057	9.6 E-03	5.7 E-03
Standard Error	257	0.098	2.0	5.3E-05	2.0 E-04
Median	41504	1.72	2057	9.5 E-05	5.1 E-03
Standard Deviation	2930	1.12	23.1	6.1 E-04	2.3 E-03
Sample Variance	858600	1.25	534.9	3.7E-07	5.4E-06

Table 6.5. Summary of results for individual and average method with and without outliers included

	ρc, $(\frac{J}{m^3 K})$	k_{ther}, $(\frac{W}{m\,K})$	h_{cont}, $(\frac{W}{m^2 K})$	t_{start}, (ms)
All Locations	41391	1.96	2058	9.58
Outliers Removed	41096	1.72	2056	9.59

6.5.2 Simultaneous Results

Unlike the individual and averaged method, the simultaneous estimation method returned one set of parameters that it found to minimize the sum of the squares at all of the 130 locations. Using the outlier information, the simultaneous estimation was also performed with the 15 outlier locations ignored. Table 6.6 shows the estimated results using the simultaneous method.

Table 6.6. Summary of results for simultaneous method with and without outliers included.

	$\rho c,\ (\frac{J}{m^3 K})$	$k_{ther},\ (\frac{W}{m\ K})$	$h_{cont},\ (\frac{W}{m^2 K})$	$t_{start,\ (ms)}$
All Locations	42247	1.75	2060	9.55
Outliers Removed	41492	1.65	2056	9.53

6.5.3 Selection of Current Best Estimate (CBE) Values

Using the two different estimation techniques with and without outliers, four potential sets of parameters have been identified. Figure 6.18 shows how the predicted voltage for each of the four parameter sets compared to the experimental data from location 68. This figure shows that all of the estimation techniques produce parameters that fit the experimental data well. A noticeable difference exists between the predicted voltage and the experimental data in the earlier transient but this is because each parameter set tries to minimize the difference between all 130 locations, so it is inevitable that some differences will be found when comparing a single location.
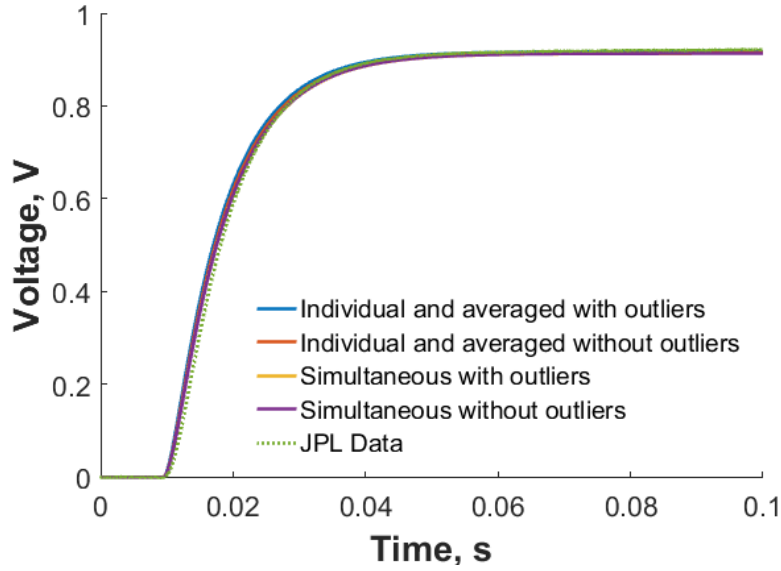
Figure 6.18. Comparison of predicted voltages using the four estimated parameter sets and the experimental data at location index 68.

Ultimately, a method for determining which of the parameter sets best fit all of the data was sought. Comparing the total sum of the squares between the four data sets would be unfair because when outliers are removed fewer total locations are available for testing. Fewer locations means that fewer data points contribute to the total sum-of-the-squares resulting in a smaller total. It was ultimately decided to select the method whose parameters produce the smallest average root-mean-square value (RMS). For a given method, the RMS can be computed as

$$RMS = \sqrt{\frac{1}{\sum_{n=1}^{N} M_n} \sum_{n=1}^{N_{Loc}} \sum_{m=1}^{M_n} \left(V_{n,m} - \hat{V}_{n,m}(\boldsymbol{\beta})\right)^2} \tag{6.15}$$

where M_n is the total number of data points compared at a given location, and N_{Loc} is the total number of locations for that method ($N_{Loc} = 130$ with outliers included or $N_{Loc} = 115$ with outliers excluded). Table 6.7 shows a summary of the parameters estimated using the four techniques and the resulting RMS. Using this criteria, performing simultaneous estimation, with outliers removed, produces the best overall fit. This makes sense as the simultaneous method by default tries to find a set of parameters that best fits all of the tested locations. Additionally, removing locations that produce bad results only improves this fit. Using the parameters $\rho c = 41492 \frac{J}{m^3 K}$, $k_{ther} = 1.65 \frac{W}{m \, K}$, $h_{cont} = 2056 \frac{W}{m^2 K}$, and $t_{start} = 9.53 \, ms$ (shown in red) best replicates the given

83

experimental data. As such, the system parameters, $\rho c, k_{ther},$ and h_{cont}, should be used as input parameters to the MATLAB model. As stated previously, t_{start} is only an experimental parameter specific to this experiment and does not contribute to the overall model. With model parameters set, the detector model can produce accurate voltage data for future applications.

Table 6.7. Summary of parameter estimation results and best fit criteria.

	Parameter Estimation Technique	ρc $(\frac{J}{m^3 K})$	k_{ther} $(\frac{W}{m\ K})$	h_{cont} $(\frac{W}{m^2 K})$	t_{start} (ms)	RMS (V)
All Locations	Individual, averaged	41391	1.96	2058	9.58	0.01538
All Locations	Simultaneous	42247	1.75	2060	9.55	0.01304
Outliers Removed	Individual, averaged	41096	1.72	2056	9.59	0.01311
Outliers Removed	**Simultaneous**	**41492**	**1.65**	**2056**	**9.53**	**0.01268**

A time constant map was generated using these determined CBE values. Figure 6.19(a) illustrates the time constant map produced using the CBE values in milliseconds. A time series voltage was computed corresponding to an extreme illumination for all locations in the 30-by-15 mesh. After the time series voltage had been evaluated, the time constant for that location was determined based on a first-order system (i.e. time required for voltage to reach 63 percent of the maximum voltage). For comparison, the experimentally produced time constant map (in seconds) is presented in Figure 6.19(b). Note: JPL evaluated a time constant by performing a least-squares fit to an exponential curve while neglecting some data points at the beginning of the time series. This difference could account for some differences between the two time constant maps. Qualitatively, the two time constant maps look similar. For both, the center of the detector has the largest time constant, while moving outward towards the edges of the detector produces a gradually smaller time constant. However, a noticeably larger gradient in the time constant map is produced

by the model. Quantitatively, the maximum time constant value simulated from the model is approximately 1 ms faster than the physical detector. This could be an artifact of some interdependency between the estimated system and experimental parameters. For instance, if the heat source is estimated to be energized at $t_{start} = 8.5$ ms rather than $t_{start} = 9.5$ ms, the overall response time of the detector would now be 1 ms slower. As a result, the simulated time constant map would more closely replicate that of the physical detector.
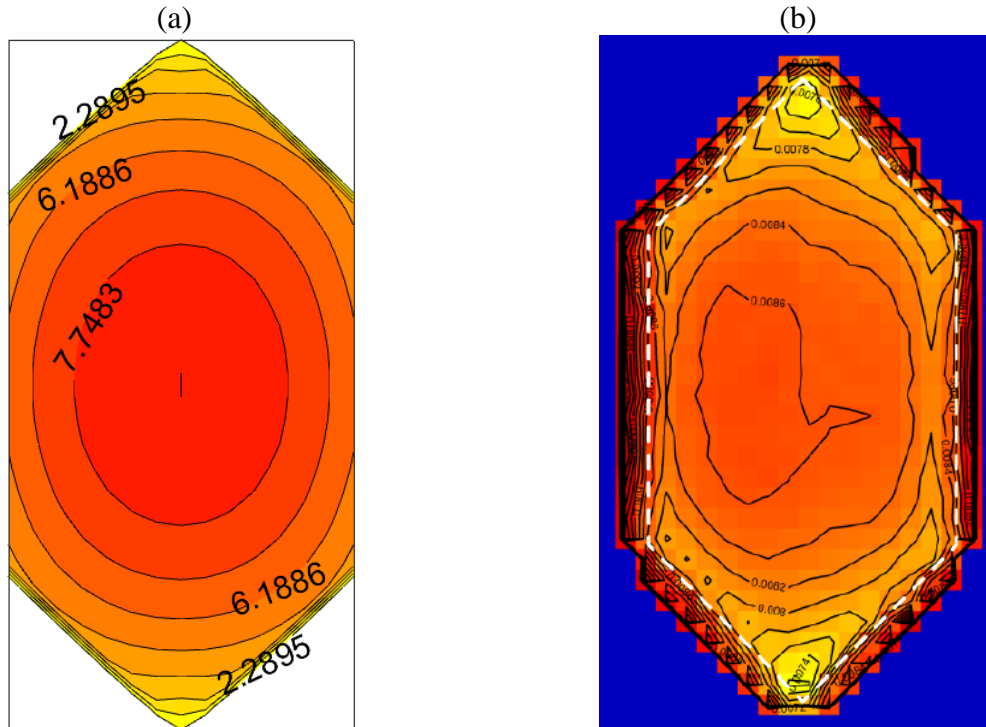
Figure 6.19. Time constant map comparison between (a) model results simulated using CBE parameters (ms) and (b) JPL experimental data (s).

In the simulated time constant map, the time constant values near the boundaries are significantly smaller than that of the physical detector. This is likely due to the assumption that the thermopile fence spans the thickness of the detector. In the model, energy absorbed in boundary cells immediately produces a voltage as these cells are in direct contact with the thermopile. However, due to the composition of the physical detector depicted in Figure 2.8, the energy would need to conduct through the entire thickness of the detector and contact the thermopile fence below the surface. This would reduce the overall time constant of the entire detector improving the agreement between the two time constant maps. However, in order to capture this effect a full three-dimensional model would be needed.

85

7   Summary, Conclusion and Recommendations

This chapter documents the conclusions that can be drawn from this effort and lists recommendations for further research.

7.1   Summary

This thesis presents an electro-thermal model of the sensor in the Radiation Budget Instrument (RBI). This model is to be incorporated with a complete end-to-end model of the entire instrument. A summary of this effort is presented:

- A mathematical model capable of characterizing a typical sensor in a radiation budget instrument has been presented. This model includes two-dimension conduction, incident irradiation, radiation exchange with instrument surroundings and boundary loss from contact conduction with a thermopile fence.

- An implicit finite volume solution, based on center-spaced rectangular control volumes, was developed. This solution utilized the "Library of Elementary Processes" allowing the user to quickly and efficiently implement additional thermal processes for future applications.

- A MATLAB algorithm has been to implement the finite volume solution. This algorithm converts incident irradiation to sensible heat producing a voltage signal. The algorithm allows the user to specify thermal properties of the sensor and the appropriate heat source allowing for future modifications.

- A thorough model analysis demonstrated the relationship between input parameters and the output voltage – specifically the magnitude of h_{cont}, the fixed position of the incident heat source, and a moving heat source.

7.2   Conclusions

The following conclusions can be drawn from this effort:

- A methodology for meshing non-rectangular objects in a rectangular mesh is presented and proved to be a viable option when utilizing an appropriately fine mesh. For the RBI application, it was found that an 18-by-9 mesh is adequate for representing the hexagonal sensor.

86

- A parameter estimation scheme, based on a least-squares method, proved to be an adequate method for determining optimal model parameters for the real RBI instrument. Four comparable techniques for utilizing available instrument data are evaluated. Using a technique that simultaneously accounts for all data locations, rejecting statistically determined outliers, has been found to determine parameters that most accurately replicate instrument performance.

- With these model parameters defined, the electro-thermal model, in conjunction with the remaining pieces of the end-to-end model, can be used to provide insight for future interpretation of data produced by the Radiation Budget Instrument.

7.3 Recommendations

The following recommendations are made for future effort:

- Extend the model to include the substrate surrounding the hexagonal detector. Assuming the surrounding substrate temperature is locked at a known temperature is sufficient for the scope of the research presented here; however, in operation, the radiation flooding the focal plane and other factors may change the substrate temperature.

- Estimate model parameters using data sets from multiple detectors. All of the data presented were collected using a single detector. Ideally similar results would be obtained; however, drastic variations in parameters might speak to the manufacturability of the detectors.

- Incorporate spatially varying thickness of the detector. It is hypothesized that data identified as outliers could be due to non-uniformity in the thickness of gold-black across the detector.

- Develop a thermal model of the detector that accounts for the fractal structure of gold-black.

References

[1] Wielicki, B. A., Harrison, E. F., Cess, T. D., King, M. D., and Randall, D. A., 1995, "Mission to Planet Earth: Role of Clouds and Radiation in Climate," Bulletin of the American Meteorological Society, 76(11), pp. 2125-2154.

[2] Priestley, K. J., 1997, "Use of First-Principle Numerical Models to Enhance the Understanding of the Operational Analysis of Space-Based Earth Radiation Budget Instruments," Doctoral Dissertation, Virginia Tech.

[3] Pfab, J. F., Vick, B., Mahan, J. R., and Priestley, K., 2017, "Thermal Analysis of the Sensor in a Radiation Budget Instrument," (57885), p. V001T004A003.

[4] Finneran, M., "'First Light' Taken by NASA's Newest CERES Instrument," Date Accessed: November 26, 2017. https://www.nasa.gov/mission_pages/NPP/news/npp-ceres-firstlight.html.

[5] Georgieva, E., Priestley, K. J., Dunn, B., Cageao, R., Barki, A., Osmundsen, J., Turczynski, C., and Abedin, N., "Radiation Budget Instrument (RBI) for JPSS-2," Proc. 24th Conference on Characterization and Radiometric Calibration for Remote Sensing (CALCON).

[6] Fanney, A. H., 1975, "Experimental study of the LZEEBE measurement system under simulated flight conditions," M.S. Thesis, Virginia Tech.

[7] Sorensen, I., 2002, "Design and analysis of radiometric instruments using high-level numerical models and genetic algorithms," Doctor of Philosophy Dissertation, Virginia Tech.

[8] Sanchez, M. C., 2002, "Uncertainty and Confidence Intervals of the Monte Carlo Ray-Trace Method in Radiation Heat Transfer," Doctor of Philosoph Dissertation, Virginia Tech.

[9] Quinlan, B. R., 2015, "A Model For The Absorption Of Thermal Radiation By Gold-Black," Master of Science Thesis, Virginia Tech.

[10] Mahan, J. R., Barki, A. R., and Priestley, K. J., 2016, "Diffraction and Polarization Effects in Earth Radiation Budget Measurements," Appl. Opt., 55(34), pp. D54-D59.

[11] Mahan, J. R., Barki, A. R., and Priestley, K. J., 2017, "Diffraction and Polarization Effects in Radiation Heat Transfer: A Case Study," (57885), p. V001T002A002.

[12] Stancil, M. M., 2016, "Creation and Experimental Validation of a Numerical Model of a Michelson Interferometer," Master of Science Thesis, Virginia Tech.

[13] Barki, A. R., and Priestley, K. J., "Radiometric System Model for RBI," Proc. 26th CERES-II Science Team Meeting.

[14] Vick, B., Mahan, J. R., and Priestley, K. J., "Thickness Allocation Between Two Fused Silica Filters," Proc. 25th Conference on Characterization and Radiometric Calibration for Remote Sensing (CALCON).

[15] Beck, J. V., Blackwell, B., and Charles R. St. Clair, J., 1985, Inverse Heat Conduction: Ill-posed Problems, John Wiley & Songs, Inc., New York, NY.

[16] Ozisik, M. N., and Orlande, H. R. B., 2000, Inverse Heat Transfer: Fundamentals and Applications, Taylor & Francis, New York, NY.

[17] McMasters, R. L., de Monte, F., and Beck, J. V., 2017, "Estimating Two Parameters From Two Complementary Transient Experiments," (57892), p. V002T015A004.

[18] Vick, B., and Diller, T. E., "Estimating Perfusion with a Combined Heat Flux and Temperature Sensor," Proc. 2016 Inverse Problems Symposium.

[19] Vick, B., and Schneck, I. I. I. W. C., 2011, "Estimation of the Real Area of Contact in Sliding Systems Using Thermal Measurements," Journal of Tribology, 133(3), pp. 031407-031407-031412.

[20] NOAA, "Joint Polar Satellite System," Date Accessed: 19 October 2017. http://www.jpss.noaa.gov/mission_and_instruments.html.

[21] NASA, "RBI ", Date Accessed: October 19, 2017. https://fpd.larc.nasa.gov/rbi.html.

[22] Priestley, K. J., Shankar, M., and Barki, A., "RBI Instrument Overview," Proc. 26th CERES-II Science Team Meeting.

[23] Glumb, R., Overbeck, J., Lietzke, C., Forsythe, J., and Miller, J., "Radiation Budget Instrument (RBI) Performance Update," Proc. Conference on Characterization and Radiometric Calibration for Remote Sensing.

[24] Glumb, R., Lietzke, C., Overbeck, J., and Webb, M., "The Radiation Budget Instrument (RBI): Instrument Overview and Calibration Features," Proc. Conference on Characterization and Radiometric Calibration for Remote Sensing.

[25] Mariani, G., Kenyon, M., Pearson, J., and Holmes, W., "Far-infrared room-temperature focal plane modules for radiation budget instrument," Proc. 2016 41st International Conference on Infrared, Millimeter, and Terahertz waves (IRMMW-THz), pp. 1-2.

[26] Incropera, F. P., 2006, Fundamentals of Heat and Mass Transfer, John Wiley & Sons.

[27] Mahan, J. R., 2002, Radiation Heat Transfer: A Statistical Approach, John Wiley and Sons.

[28] Barki, A. R., Priestley, K. J., Mahan, J. R., and Vick, B., "First-principle dynamic electro-thermal numerical model of the Radiation Budget Instrument (RBI)," Proc. 28th CERES-II Science Team Meeting.

[29] Vick, B., Mahan, J. R., and Priestley, K., "Complex Model Building: Application to the Earth Radiation Budget Instrument," Proc. 4th International Workshop on Heat Transfer, American Society of Thermal Fluid Engineers.

[30] Patankar, S. V., 1980, Numerical Heat Transfer and Fluid Flow, Hemisphere Publishing Corporation.

[31] John D. Anderson, J., 1995, Computational Fluid Dynamics: The Basics with Applications, McGraw-Hill, Inc.

[32] RBI Technical Memo 17-022 "JPL Detector Response and Time Constant Spot Scan Data for RBI Flight Modules."

[33] RBI Technical Memo 17-022, "JPL Detector Time Constant Maps from EDU SN104 Spot Scans."

[34] Vick, B., 2016, "Applied Mathematics: Course Notes for ME 5304 and ME 5744."

Appendix A: MATLAB Main Script

```matlab
function [ TimeSeriesVoltage ] = ThermalModel( IncidentPower )
%Thermal Model is an algorithm that will compute the time series Voltage
%for the RBI Instrument
%
%   Input: Incident power- The user must input a time series function that
%   tells how much power is incident to the detector as a function of time
%
%   Output: TimeSeriesVoltage - The program will export the Voltage as a
%   function of time to be saved for later


%% ~~~~~~~~~~~~~~~~~~~~~~~~~Thermal Properties~~~~~~~~~~~~~~~~~~~~~~~~%%
% This Build has properties that assume the sensor is made up of a 3 layer
% system. These properties have been computed in a separate analysis and
% should only be changed if necessary. The three layers are as follows:
%           30 um gold black
%           18 nm gold shunt
%           250 nm gold absorber
%The model uses the thickness weighted average of each individual layer to
%compute an equivalent density, rho; equivalent specific heat, c; and
%equivalent thermal conductivity, kther.

%Density of the material in kg/m^3 %%This has been changed to rhoc
rho = 41492;


%Specific Heat of the material in J/kg*K
c = 1;

%Input the thermal conductivity of the material W/m*K
kther = 1.65;




%% ~~~~~~~~~~~~~~~~~~~~~~~~~Physical Geometry~~~~~~~~~~~~~~~~~~~~~~~~%%

% This Section sets the physical geometry of the sensor.
% Lx is defined as the dimension from the 'tip' of the sensor to the bottom
% 'tip' of the sensor. i.e. the long direction
% Ly is defined as the dimension across the sensor
% Lz is the combined thickness of the individual layers
% Note: Please convert the lengths to meters

Thickness_GoldBlack = 0.03*10^-3; %m
Thickness_GoldShunt = 18*10^-9; %m
Thickness_GoldAbsorber = 250*10^-9; %m


Lx = 2.269*10^-3; %m
Ly = 1.1345*10^-3; %m
Lz = Thickness_GoldBlack + Thickness_GoldShunt + Thickness_GoldAbsorber; %mm
```

```matlab
%% ~~~~~~~~~~~~~~~~~~~~~~~~~~Discretization Parameters~~~~~~~~~~~~~~~~%%

%Input the number of cells you want use in the y direction. Increase jj for
%finer grid.
%  Note: Please use an odd number. Additionally, to keep the cells the same
%  size, please allow ii (x-direction) to have 2 times as many cells as jj
%  (y-direction)

jj = 15;
ii = 2*jj;




%Precompute grid sizes
dx = Lx/ii;
dy = Ly/jj;

%% ~~~~~~~~~~~~~~~~~~~~~~~~~Thermocouple Properties~~~~~~~~~~~~~~~~~~~%%

%Equivalent Seebeck coefficient for the n and p thermocouples
alpha_Seebeck = (255)*10^-6;

%Input the number of thermocouple junction pairs
N_Thermocouples = 898;

%% ~~~~~~~~~~~~~~~~~~~~~~~~~Time Step Properties~~~~~~~~~~~~~~~~~~~~~~%%
% By default, the algorithm will compute a full scan with a 100 Hz sampling
% rate.

%Properties that can be changed
N_Scans = 1.0; %By default the program is set to one scan. A down and back
SamplingFrequency = 100; %Hz
CycleTime = 6.6; %By default the program will assume a 6.6s cycle time




%Compute Algorithm properties. Please do not change
dt = 1/SamplingFrequency; %Time step size
tmax = N_Scans * CycleTime;

%This algorithm uses the variable 'p' to march through time. pmax is the
%last computed time
pmax = ceil(tmax/dt);

%% ~~~~~~~~~~~~~~~~~~~~~~~~~Surrounding Interaction Parameters~~~~~%%

%Thermal Conductance Parameters.
hcont = 2056; % W/m^2 %Predetermined to account for loss due to
%thermocouples

Tsur = 308; %Nominal telescope enclosure temperature
```

```matlab
%Radiation Parameters
epsilon = 0.99; %Surface Property of gold Black




%% ~~~~~~~~~~~~~~~~~~~~~~~~~~~Precomputed Parameters~~~~~~~~~~~~~~~~~~~~%%
% This section computes the parameters to be used in the code. They need to
%be computed once and then never changed

%Compute thermal diffusivity and Fourier number for later use
alpha = kther/(rho*c);
Fo = alpha*dt/(dx^2);

%Thermal Conductance Parameters.
htherm = @(t) hcont* heaviside(t);
Tinf = @(t) Tsur*heaviside(t); %Tsur can be a function of time is allowed
%to drift. By default the heaviside function makes it a constant

%Compute the Hex Gaps that outlines where the hex occupies in the overal
%rectangular grid
Gaps = HexGaps(ii,jj);

%Compute the Hex Filter. Used to ensure that irradiation effects only hit
%the sensor
FilterHex = Filter(ii,jj, Gaps);

%Compute BoundaryA/V Matrix. Computes the BoundaryAreaPerVolume ratio to
%be used in the boundary loss component
BoundaryAreaPerVolHexMat = BoundaryAreaPerVolHex(ii,jj, dx, dy);

%Compute Conduction, Radiation, and BC coeffiecents
PhiCondRect2DCoefHex = PhiCondRect2DCoef(ii,jj,Fo, Gaps);
PhiBCCoefHex = @(t) PhiBCCoef(ii, jj, BoundaryAreaPerVolHexMat,...
    htherm(t), rho, c, dt);
PhiRadCoefHex = PhiRadCoef(ii, jj, FilterHex, epsilon, Lz, dt, rho, c);

%Preallocate Solution Matrix and set the Initial Temperature Condition
%The Temperatures at each time step are in vector form and are latter
%partitioned into a 2D Grid

TSolVector = zeros(pmax+1, ii*jj);
TSolVector(1,:) = Tsur.*myflatten(FilterHex);
TSol = zeros(pmax, ii, jj); %Initialize 2D Form of Solution
Voltage = zeros(pmax,1); %Initialize Voltage

%% ~~~~~~~~~~~~~~~~~~~~~~~~~Power Incident To Detector~~~~~~~~~~~~~~%%

%Compute Source Uniform Everywhere
Area_Irrad = .5*Ly*.25*Lx + Ly*.5*Lx+ .5*Ly*.25*Lx; %Set Illuminated Area.
Irrad = @(x,y) (1/(Lz*Area_Irrad)).* heaviside(x).*heaviside(y);

%Compute Source Term
```

```matlab
PhiSourceCoef = @(t) PhiSource2D(Lx, ii, Ly, jj, rho, c, Irrad,dt)...
    .*FilterHex*IncidentPower(t);

%% ~~~~~~~~~~~~~~~~~~~~~~~~~~~Compute Temperatue Solution~~~~~~~~~~~~~~~%%
for p = 1:pmax

    TSolVector(p+1,:) = TSolVector(p,:);

    TSolVector(p+1,:) = PhiCondRect2DPhiSourcePhiRadPhiBC(...
        PhiCondRect2DCoefHex,PhiSourceCoef(p*dt), PhiRadCoefHex,...
        PhiBCCoefHex(p*dt), Tinf(p*dt), TSolVector(p+1,:)...
        );

end

%% Partition into 2D Temperature solution and compute the voltage
for p = 1:pmax
    TSol(p,:,:) = mypartition(TSolVector(p,:), jj);

    Voltage(p) = VoltagePerSeebeck( squeeze(TSol(p,:,:)), Tsur,...
        BoundaryAreaPerVolHexMat)*N_Thermocouples*alpha_Seebeck; %Volts
end




%% Save results
TimeIndex = linspace(0,tmax,pmax);
TimeSeriesVoltage = zeros(pmax,2);
TimeSeriesVoltage(:,1) = TimeIndex;
TimeSeriesVoltage(:,2) = Voltage;

end
```

Appendix B: Sample Input File

```matlab
%% Create Random Heat Source that lasts for CycleTime

CycleTime = 6.6;
N_Samples = 1000;


Time = linspace(0, CyclTime, N_Samples);

%Create Random Powers at every time increment
%To avoid issues, use heat source representative of real instrument.
%As such, confirm that it uses microWatts

MaxRandIndex=100;
Power = 10^-6* randi(MaxRandIndex,[1,length(Time)]);


TransientPower = fit(Time', Power', 'linearinterp');


VoltageOutput = ThermalModel(TransientPower);
```

Appendix C: Library of Elementary Processes Functions

```matlab
function [ Tnew ] = PhiCondRect2DPhiSourcePhiRadPhiBC(PhiCondRect2DCoef,...
    PhiSource2DCoef, PhiRadCoef, PhiBCCoef, Tinf, Told )
%Compound process for 2D Rectangular conduction with Volumetric source,
%radiation and BC

BCBand = diag(myflatten(PhiBCCoef));
BCBand = sparse(BCBand);

FactoredTempPart = (Told.^2 + Tinf^2).*(Told + Tinf);
RadCoefTable = myflatten(PhiRadCoef).*FactoredTempPart;
RadBand = diag(RadCoefTable);
RadBand = sparse(RadBand);


Tnew = (PhiCondRect2DCoef + BCBand + RadBand)\...
    (Told + myflatten(PhiBCCoef).* Tinf + RadCoefTable.* Tinf...
    + myflatten(PhiSource2DCoef))';


end
```

```matlab
function [ BCMatrixFiltered ] = PhiBCCoef( ii, jj, BoundaryAreaPerVol, h,...
    rho, c, dt )
%Compound Function Coef for PhiBC


BCCoefMatrix = h *(dt)/(rho*c) * ones(ii,jj);

BCMatrixFiltered = BCCoefMatrix .* BoundaryAreaPerVol;


end
```

```matlab
function [ CondRect2DCoefMat ] = PhiCondRect2DCoef( ii, jj, Fo, varargin )
%Coef For 2D Conduction
gaps = cell2mat(varargin);

if length(gaps) ~= 0
    CondRect2DCoefMat = sparse(eye(ii*jj)) + Fo*PhiCond2DMat(ii,jj, gaps);
else
    CondRect2DCoefMat = sparse(eye(ii*jj)) + Fo*PhiCond2DMat(ii,jj);
end

end
```

```matlab
function [ RadMatrixFiltered ] = PhiRadCoef( ii, jj, FilterList,...
    epsilon, Lz, dt, rho, c )
%Coef for Radiation

sigma = 5.67*10^-8;

RadMatrix = (epsilon*sigma/Lz) *(2*dt)/(rho*c) * ones(ii,jj);

RadMatrixFiltered = RadMatrix .* FilterList;


end
```

```matlab
function [ SourceMatrix ] = PhiSource2D( Lx, ii, Ly, jj, rho, c, g, dt )
%2D Rectangular Source Setup


i = 1:ii;
j = 1:jj;

dx = Lx/(ii);
x=(i-1)*dx;
xMesh = transpose(repmat(x,jj,1));

dy = Ly/(jj);
y=(j-1)*dy;
yMesh = repmat(y,ii,1);


SourceMatrix = g([xMesh], [yMesh])* (dt/(rho*c));

end
```

```matlab
function [ cond2DMat ] = PhiCond2DMat( ii, jj, varargin )

gaps = cell2mat(varargin);


topBand = -1*ones((ii-1)*jj,1);
rightBand = -1*ones(ii*jj-1,1);
rightBand(jj:jj:ii*jj-1) = 0;


cond2DMatUpper =  diag(rightBand,1) + diag(topBand,jj);

cond2DMatLower = transpose(cond2DMatUpper);

cond2DMat = cond2DMatUpper +cond2DMatLower;


if length(gaps) ~= 0
    for ij=1:length(gaps)
        cond2DMat(gaps(ij),:) = 0;
        cond2DMat(:,gaps(ij)) = 0;
    end

end

   middleBand = -1*sum(cond2DMat,2);
   cond2DMat = sparse(cond2DMat + diag(middleBand));
end
```

Appendix D: Utility Functions

```matlab
function [ BoundaryAreaPerVolMatrix ] = BoundaryAreaPerVolHex( ii, jj,...
    dx, dy, FilterList )
%Creates Boundary Area per Volume matrix for a Hex

BoundaryAreaPerVolMatrix = zeros(ii,jj);


jCenter = (jj +1)/2;
%Calculated A/V along the left and Right Boundaries

for i=jCenter:jCenter+jj
    BoundaryAreaPerVolMatrix(i,1) = 1/dy;
    BoundaryAreaPerVolMatrix(i,jj) = 1/dy;
end



%Calculated A/V for the 4 slopes
for i=1:jCenter

    BoundaryAreaPerVolMatrix(i,jCenter+i-1) = sqrt(dx^2+dy^2)/(dx*dy);
    BoundaryAreaPerVolMatrix(i,jCenter-i+1) = sqrt(dx^2+dy^2)/(dx*dy);
    BoundaryAreaPerVolMatrix(jCenter+jj+i-1,i) = sqrt(dx^2+dy^2)/(dx*dy);
    BoundaryAreaPerVolMatrix(jCenter+jj+i-1,jj-i+1) =...
        sqrt(dx^2+dy^2)/(dx*dy);

end

%Do the two peaks
    BoundaryAreaPerVolMatrix(1,jCenter) = 2*sqrt(dx^2+dy^2)/(dx*dy);
    BoundaryAreaPerVolMatrix(ii,jCenter) = 2*sqrt(dx^2+dy^2)/(dx*dy);



end
```

```matlab
function [ FilterBoundary ] = BoundaryFilter( ii, jj )
%Creates the Boundary Filter For A Hex

jCenter = (jj+1)/2;

FilterBoundary = zeros(ii,jj);

%Place 1's along the left and right boundaries
for i=jCenter:jCenter+jj
    FilterBoundary(i,1) = 1;
    FilterBoundary(i,jj) = 1;
end

%Place 2's along the 4 slopes
for i = 1:jCenter
    FilterBoundary(i, jCenter + i -1) = 2;
    FilterBoundary(i, jCenter - i +1) = 2;
    FilterBoundary(jCenter + jj + i - 1, i) = 2;
    FilterBoundary(jCenter + jj + i - 1, jj - i + 1) = 2;

end

%Do the two peaks
FilterBoundary(1,jCenter) = 2;
FilterBoundary(ii,jCenter) = 2;


end
```

```matlab
function [ FilterMatrix ] = Filter( ii, jj, gaps )
%Creates a Hex Filter to ensure the effect only hits the hex

Unfiltered = ones(ii,jj);

FilterVector = myflatten(Unfiltered);

for ij=1:length(gaps)
    FilterVector(gaps(ij)) =0;
end

FilterMatrix = mypartition(FilterVector, jj);
end
```

```matlab
function [ GapsList ] = HexGaps( ii, jj )
%Computes the elements to be zeroed out to create 2D conduction for a
%hex geometry

%Preallocate
upperLeftCorner = [];
upperRightCorner = [];
lowerLeftCorner = [];
lowerRightCorner = [];


jCenter = (jj+1)/2;

for i=1:jCenter-1
    for j = 1:jCenter-i
        upperLeftCorner = [upperLeftCorner,(i-1)*jj+j];
    end
end

for i=1:jCenter-1
    for j = jCenter+i:jj
        upperRightCorner = [upperRightCorner,(i-1)*jj+j];
    end
end

for i=ii:-1:ii-(jCenter -2)
    for j = 1:i-ii+(jCenter -1)
        lowerLeftCorner = [lowerLeftCorner,(i-1)*jj+j];
    end
end

for i=ii:-1:ii-(jCenter -2)
    for j = ii+(jCenter +1) -i:jj
        lowerRightCorner = [lowerRightCorner,(i-1)*jj+j];
    end
end


GapsList = [upperLeftCorner, upperRightCorner, lowerLeftCorner,...
    lowerRightCorner ];
end
```

```matlab
function [ FlattenedArray ] = myflatten( UnflattenedArray )
%This function flattens an array similar to the function Flatten in
%Mathematica
%   Input an NxM array and a row dominate NM vector is output

FlattenedArray = reshape(UnflattenedArray', 1, []);


end
```

```matlab
function [ PartitionedVector ] = mypartition( FlattenedVector, jj )
%Used to partion a vector into a matrix that has jj columns

PartitionedVector = reshape(FlattenedVector, jj, [])';


End
```

```matlab
function [ Voltage ] = VoltagePerSeebeck( TempList, Tref, BoundaryList )
%Returns the Voltage Per Seebeck at one time step

Voltage = sum(sum((TempList - Tref).*BoundaryList))/sum(sum(BoundaryList));

end
```